Chapter 5: Open-system, metasomatic, diffusion modelling of complex coronas in pelitic granulites from the Vredefort Dome

5.1 Introduction

The unique sectoral and radial heterogeneity of coronas developed in the Steynskraal rocks has been described in Chapter 4. In this chapter, diffusion modelling of coronas is undertaken on the garnet-quartz coronas as part of a coupled modelling approach aimed at quantifying controls on reaction extent and equilibration in the coronas. The theory of open-system diffusion modelling has been discussed in Chapter 3 and mathematical formulations are included in Appendix A.

Open-system diffusion models have been constructed for coronas developed between garnet and quartz from three localities across the Steynskraal traverse representing a range in inferred post-shock temperatures from numerical modelling (Ivanov, 2005) and local bulk compositions. To test temperature control on corona development, coronas were selected with restricted initial compositional variation to minimize any incipient compositional controls on reaction extent, i.e., the 'starting' compositions had to be the same. During reaction the compositions of the corona effective bulk compositions will have evolved depending on diffusion rates and duration of reaction as a function of temperature. Initial conditions needed to be identical to constrain subsequent corona evolution as a function of temperature alone. Optimal coronas selected for this purpose are those developed around quartz inclusions in garnet where interaction with the matrix is limited. Selection of appropriate garnet-quartz core coronas required reconstruction of potential incipient corona bulk compositions prior to reaction. Given the extent of diffusional resetting of the peak garnet composition during post-impact reaction (SK9-CLM, Section 2.5), the original composition of the corona bulk compositions could not be accurately reconstructed using the measured garnet composition at present. The initial bulk compositions for each garnet-quartz corona domain immediately prior to onset of corona formation had to be determined from the peak Archaean compositions in THERMOCALC (Table 5.1). Theoretical THERMOCALC initial

bulk corona compositions comprise 50 mol% peak garnet, 49 mol% quartz and 1 mol% 'matrix'. The 'matrix' component constitutes a minor contribution to the corona bulk composition by matrix phases recalculated to 1 mol%, in their original proportions and compositions in the peak assemblage (see Section 6.1 for further discussion). The actual bulk corona compositions differ for every corona depending on the degree of metasomatic exchange with the surrounding rock during corona formation. The theoretical corona bulk compositions serve only as a guideline in terms of selection of coronas for modelling.

Three coronas developed around quartz inclusions within the cores of garnets from SK8C, SK12A and SK9 were selected for modelling. The three sample localities occur at roughly 1 km intervals along the Steynskraal traverse from the northwest at SK8C to the southeast at SK9 (Figure 5.1). Post-shock temperature, inferred from numerical impact models (Ivanov, 2005), increases from ~ 950 ºC at 8 km (SK8C) from the centre of the Dome to ~ 1050 ºC at 5 km from the centre of the Dome (SK9). As described in Chapter 4, Sections 4.2.1 and 4.3.1, the garnet-quartz corona domains in SK8C, SK12A and SK9A comprise a cordierite-orthopyroxene (Opx_{S1}) symplectite adjacent to garnet, followed by a monomineralic plagioclase layer, terminated by a monomineralic, blocky orthopyroxene layer (Opx_b) (Figure 5.2). Layer thickness and vermicule size increase by an order of magnitude from SK8C to SK9 (Figure 5.2, Chapter 4, Section 4.4). Theoretical incipient bulk corona compositions are included in Table 5.1. Apart from a slight variation in the X_{Mg} of reactant garnet, reflecting bulk rock variation in X_{Mg} (see Chapter 2, Tables 2.1 and 2.2) the initial bulk compositions for all three incipient coronas are as similar as reasonably possible (Table 5.1). Phase equilibria modelling in Chapter 6 (Figure 6.46) establishes that the solidus temperature and, hence, reaction duration (Chapter 6.1), is independent of corona bulk composition X_{Mg}. Accordingly, the minor difference in X_{Mg} between these local bulk compositions exerts no influence on equilibration extent. Any variation in reaction extent can, thus, be attributed to temperature control alone and evolving bulk composition by metasomatic exchange with the matrix through prolonged reaction.

In order to assess the influence of bulk composition on extent of corona formation and equilibration, two additional coronas with the same inferred post-shock temperatures from SK9 (Figure 5.1) were then modelled. These coronas include - in addition to the corona around a quartz inclusion within garnet (SK9A) - a second corona in the core of garnet adjacent to a K-feldspar inclusion (SK9B), and a corona developed at the margin of garnet (SK9C) (Figure 5.2). SK9B and SK9C exhibit the same layer sequence as SK9A except that orthopyroxene vermicules (Opx_{S2}) are present in the plagioclase-orthopyroxene symplectite comprising layer 2 (Figure 5.2c, d). SK9B differs from all other coronas in that a monomineralic K-feldspar layer separates plagioclase-orthopyroxene layer 2 from blocky orthopyroxene layer 4. Layer thickness, vermicule size and spacing are greater in SK9C compared to both SK9A and SK9B (Figure 5.2, Chapter 4). Local incipient corona bulk compositions were determined in THERMOCALC from combinations of peak reactant garnet with quartz and K-feldspar in SK9B and quartz and matrix phases in SK9C, to yield the observed corona product modes, and are included in Table 5.1. SK9B has higher Na_2O, K_2O and Al_2O_3 contents compared to SK9A, which are required to stabilise the K-feldspar observed in the corona assemblage. SK9C is marginally more hydrous, Mg-rich and aluminous compared to SK9A, consistent with the higher observed cordierite modes and trace biotite in the corona domain.

The anhydrous nature of the coronal assemblages modelled obscures the fact that melt must have been present during reaction (Chapter 3, Section 3.6; Chapter 6, Section 6.1). White and Powell (2002) established that suprasolidus *P-T* conditions are required for reaction to occur in a restitic granulite that has previously lost melt during the peak event. Post-shock temperature estimates in excess of 950 °C from numerical modelling (Ivanov, 2005) for the Steynskraal traverse are certainly high enough to induce suprasolidus reaction. The final assemblage observed at present in the coronas is that which is preserved at the solidus upon back-reaction with the melt. The melt serves as an intergranular medium for diffusion, facilitating open-system behaviour in corona reaction domains. The physical loss of melt from a corona domain is also a potential mechanism for loss of Al and Si from the system. The role of melt in corona-forming reactions is assessed in Chapter 6, Section 6.7.3.

Table 5.1: Inferred THERMOCALC bulk compositions for SK8C, SK12A , SK9A, SK9B and SK9C coronas

Component (mol%)	SK8C	SK12A	SK9A	SK9B	SK9C
SiO_2	71.01	71.05	70.98	68.49	66.06
Al_2O_3	7.26	7.28	7.28	8.53	8.25
FeO	12.69	13.14	11.94	11.93	12.97
MgO	8.81	8.34	9.57	9.56	11.77
CaO	0.13	0.07	0.1	0.17	0.1
Na_2O	0.04	0.04	0.04	0.54	0.04
K_2O	0.03	0.05	0.04	0.72	0.63
H_2O	0.03	0.03	0.05	0.05	0.18
X_{Mg}	0.41	0.39	0.44	0.44	0.48

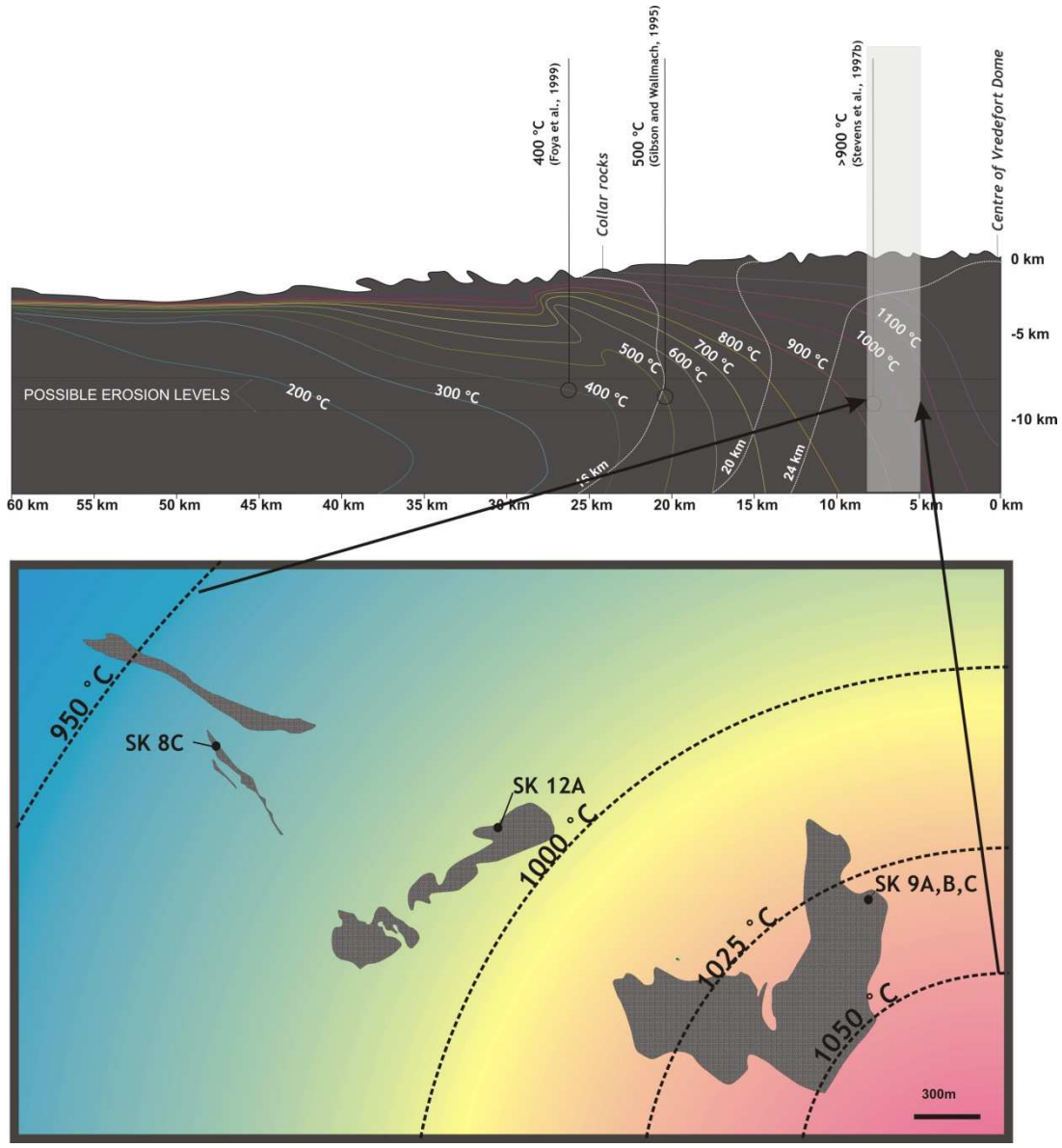

Figure 5.1: Distribution of sample localities for coronas SK8C, SK12A and SK9A, B, C in the Steynskraal area. Post-shock temperature increases from SK8C to SK9 toward the centre of the Dome according to numerical modelling (modified after Ivanov, 2005). Coronas from a variety of textural and compositional settings at SK9, i.e., SK9A, B and C, were selected to demonstrate the influence of bulk compositional parameters on corona development at constant post-shock temperature.

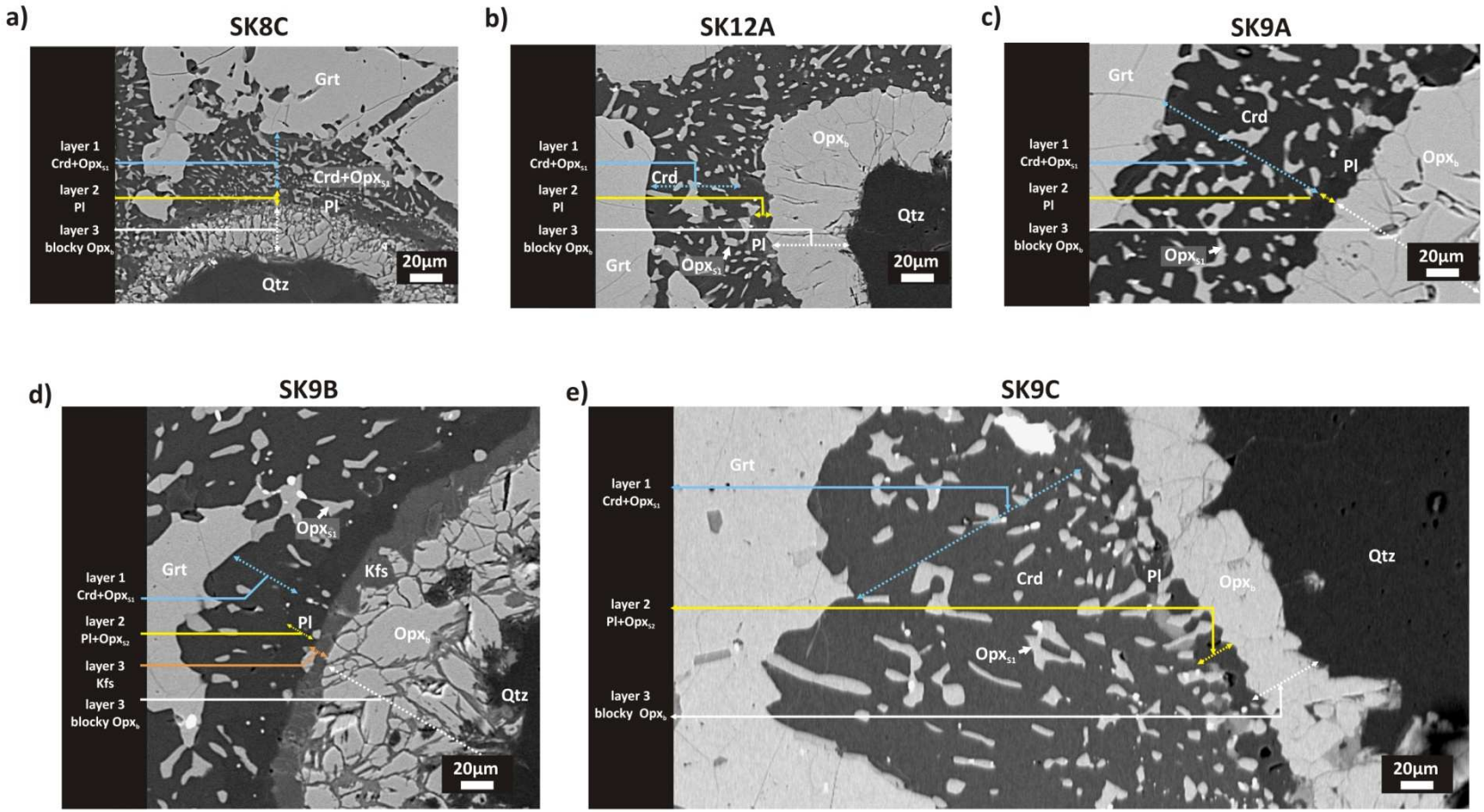

Figure 5.2: BSE images of the coronas investigated in this study: (a) SK8C (8 km from centre of Dome), (b) SK12A (6.5 km from centre of Dome), (c) SK9A (5 km from centre of Dome), (d) SK9B and (e) SK9C. SK9B and SK9C both occur at 5 km from the centre of the Dome. The presence of K-feldspar in SK9B and high modes of cordierite relative to orthopyroxene in SK9C distinguish these coronas from SK9A, indicative of bulk compositional variation between the coronas. Corona layer thickness and vermicule size increase from SK8C to SK9C. Vermicule size, spacing and layer thickness are greater in SK9C compared to SK9B and SK9A.

Open-system diffusion modelling of coronas involves the application of non-equilibrium thermodynamics to reconstruct and simulate one-dimensional diffusion perpendicular to planar layer boundaries with local equilibrium. It is assumed that reaction takes place at a constant temperature and pressure and that the overall reaction stoichiometry does not change with time. The assumption of constant *P* and *T* cannot be strictly true for a corona-forming reaction which is driven by change in *P* and *T*. It is more realistic to consider the final closure pressure and temperature as that which prevailed for the longest duration during the corona-forming reaction, such that the assumption of constant *P* and *T* is approached (Ashworth et al., 2001).

The open-system diffusion models presented in this chapter are based on the coupled modelling methodologies of Ashworth and Sheplev (1997) and Carlson and Johnson (1991). Modelling is based on the primary assumptions of diffusive transport of components only through the corona and that local equilibrium is attained at every point in the corona. Local equilibrium implies the chemical potential of a component is the same in all phases at a point, and that gradients in chemical potentials of components across the corona as a whole drive diffusion. Local equilibrium is established by the partitioning of components between phases and a zone of crystalline disorder extending inwards from grain boundaries, described by Joesten (1977), as an ‘exchange medium’.

Fundamental to the modelling is the approximation of a steady-state during layer growth (Fisher, 1977). In the model of Fisher (1977), a layer grows between adjacent incompatible assemblages by reaction at the layer contacts. Components evolved at one contact of a layer diffuse through the layer to the opposite contact where they are consumed by reaction (Fisher, 1977). The fluxes and chemical potential gradients within each layer approach values which minimize the total rate of entropy production and, consequently, a quasi-stationary or steady-state condition is attained (Joesten, 1977; Fisher, 1977). By Prigogine’s Theorem in non-equilibrium thermodynamics, a stationary state is stable relative to other states derived from it by perturbations and also has a lower rate of entropy production than those perturbed states (Joesten, 1977; Fisher, 1977). In the steady state, the stoichiometric coefficients of reactions at layer boundaries are determined by the

relative component fluxes through the layer (Joesten, 1977; Fisher, 1977). The component fluxes are controlled by the chemical potential gradients in the layer, which, in turn, are dictated by the mineral assemblage in the layer.

The modelling of the final steady-state configuration of layers in a corona requires estimation of an overall reaction from measured overall proportions of minerals and their major element compositions. Three sets of simultaneous equations, relating component fluxes, chemical potential gradients and stoichiometric coefficients of phases in the reaction at each layer boundary, are then solved iteratively for a particular range of diffusion coefficients. For a given overall reaction, varying the postulated diffusion coefficients leads to varying distributions of minerals among layers. An acceptable model must match the observed distribution. Full details of modelling methodology and MATLAB code used to derive models are included in Appendix A.

In this study, in determination of the overall reaction equations, it was not possible to assume closure of the system to Al and Si (strictly $A1O_{3/2}$ and SiO_2, since the components used are oxides, following Fisher, 1973). Instead a constant-volume approximation formulated by Carmichael (1987) and first applied by Carlson and Johnson (1991) was adopted. The original interface between garnet and quartz reactants was assumed to be the boundary between layer 2 plagioclase and layer 3 blocky orthopyroxene (i.e., the contact between Al-rich and Al-poor product layers) consistent with constant volume diffusion models of a garnet-quartz corona reaction in garnet amphibolites of the Llano Uplift (Carlson and Johnson, 1991). Successful diffusion models presented below validate the assumption of placing the original interface at this position.

5.2 Mineral chemistry

Major element mineral chemical analyses were performed on a LEO 1430VP scanning electron microscope with a Link ISIS energy dispersive spectrometry system at the University of Stellenbosch. Beam conditions during the quantitative analyses were 20 KV and 1.5 nA with an acquisition time of 50 s. Spectra were processed by ZAF corrections and quantified using natural mineral standards. Mineral chemical compositions were recalculated using the software AX (T. J. B. Holland, unpublished; see: http://www.esc.cam.ac.uk/astaff/holland/ax.html). Following the methodology of Diener et al. (2005), mineral stoichiometries and the resultant mineral structural formulae were used to evaluate the quality of the analytical data. Only analyses that produced cation totals within 0.05 to 0.1 (depending on the number of cations) of the ideal stoichiometric number for each cation site were considered in the model (Diener et al., 2005). Individual analyses are tabulated in Appendix B.

Average analyses of reactant garnet and corona products for diffusion modelling are included in Table 5.2 and plotted on an AFM projection in Figure 5.3. Projection is made from both K-feldspar and plagioclase since these phases are present in at least trace amounts in all coronas, and is, thus, required when bulk corona compositions are plotted on the same diagram (see Figure 5.24). SK9 corona mineral compositions are all more Fe-rich than in SK8C and SK12A (Figure 5.3), despite higher bulk-rock X_{Mg} in SK9 (0.52) compared to SK8C (0.49) and SK12A (0.41) (Chapter 2, Table 2.1 and 2.2). Similarly, the Al content of corona orthopyroxene decreases from SK8C, to SK12A and to SK9 (Figure 5.3).

Cordierite analyses in all coronas except SK9C exhibit anomalous Si cation totals (> 5.00 based on 11 oxygens). This is due to contamination of cordierite spot analyses by orthopyroxene vermicules in the symplectite, particularly in the most fine-grained symplectite in SK8C. In contrast, orthopyroxene analyses from the symplectite are stoichiometric and do not exhibit contamination by host cordierite. Preferential contamination of cordierite and not symplectite orthopyroxene may be potentially ascribed to the relatively open, less dense, cordierite structure resulting in greater volumes of excitation by the incident electron beam in cordierite compared to

orthopyroxene for the same spot size. Consequently, cordierite analyses in all coronas will be subject to a degree of contamination from orthopyroxene vermicules. Under such conditions, the trends in X_{Mg} for cordierite in the corona will still be valid but the average composition of the cordierite cannot be used for mass balance and flux determinations critical to diffusion modelling. For the purposes of modelling, a modified, stoichiometric, cordierite composition has been determined for SK8C, SK12A, SK9A and SK9B, assuming contamination is from orthopyroxene only. The new, modified, cordierite composition approaches stoichiometric cation totals for Al and Si. Fe and Mg are removed from the modified cordierite analysis to yield stoichiometric cation totals for Fe and Mg, assuming the contaminating Fe and Mg were inherited in the same relative molar proportions as the average orthopyroxene vermicule composition in the symplectite.

Individual point analyses of corona product phases were gridded and contoured using a standard linear variogram in Surfer at a grid node spacing of 2 µm in all coronas (Figures 5.4-5.17). X_{Mg} in orthopyroxene decreases from garnet toward quartz in SK8C, SK12A and SK9B (Figures 5.4a, 5.6a, 5.11a). In SK9A and SK9C, however, the general decrease in X_{Mg} for orthopyroxene from garnet to quartz is perturbed at the contact between layer 2 plagioclase and layer 3 blocky orthopyroxene. At this contact, there is an inflection in X_{Mg} of blocky orthopyroxene to higher values (comparable to intermediate values for layer 1 orthopyroxene), followed by systematic reduction again toward the contact with quartz (Figures 5.8a and 5.15a). In all coronas, the Al content in orthopyroxene on the M1 site, y(Opx), decreases smoothly and systematically from symplectite orthopyroxene adjacent to garnet to blocky orthopyroxene adjacent to quartz (Figures 5.4b, 5.6b, 5.8b, 5.11b, 5.15b), where $y(\text{Opx}) = C_{Al,total}/2$ after Pattison et al. (2003). In general, cordierite X_{Mg} also decreases progressively across the corona toward quartz (Figures 5.5, 5.7, 5.9, 5.12, 5.16).

The plagioclase layer 2 in SK8C and SK12A was too thin to accommodate the spatial distribution of analytical points required to determine trends in composition. In SK9 coronas, plagioclase layer 2 is thick enough to allow detailed probe analysis. In SK9A, X_{Ab} decreases and X_{An} increases towards quartz (Figure 5.10). No

systematic change in plagioclase composition is observed in SK9B (Figure 5.13) and SK9C (Figure 5.17). In the monomineralic K-feldspar layer in SK9B, X_{Ab} decreases and X_{Or} increases towards quartz (Figure 5.14).

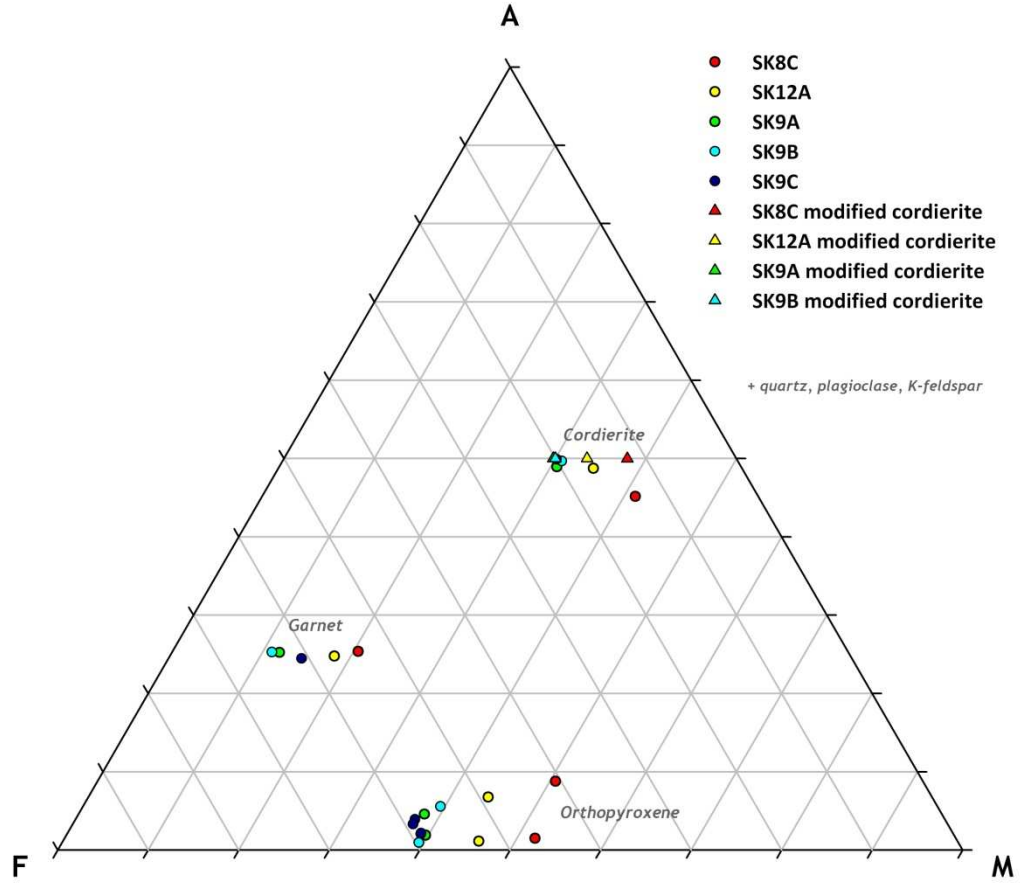

Figure 5.3: AFM projection from quartz, plagioclase and K-feldspar for corona mineral assemblages. All mineral compositions in SK9 coronas are markedly more Fe-rich compared to SK12A and SK8C.

Table 5.2: Average mineral chemistry for coronas SK8C, SK12A and SK9A

	SK8C						SK12A						SK9A					
Position			Layer 1		Layer 2	Layer 3			Layer 1		Layer 2	Layer 3	RCT		Layer 1		Layer 2	Layer 3
Mineral	***Grt***	***Crd***	***Crd****	***Opx***	***Pl***	***Opx***	***Grt***	***Crd***	***Crd****	***Opx***	***Pl***	***Opx***	***Grt***	***Crd***	***Crd****	***Opx***	***Pl***	***Opx***
SiO_2	38.39	52.08	*49.32*	48.44	63.00	51.82	37.81	51.11	*48.86*	47.56	57.80	49.04	37.09	50.81	*48.47*	47.20	59.34	47.78
TiO_2	0.00	0.00	*0.00*	0.02	0.00	0.00	0.00	0.00	*0.00*	0.00	0.00	0.00	0.00	0.00	*0.00*	0.00	0.00	0.00
Al_2O_3	22.18	29.48	*33.46*	8.49	21.46	1.51	21.98	31.76	*33.15*	5.92	25.21	1.24	21.64	31.56	*32.89*	4.02	23.94	1.80
Cr_2O_3	0.00	0.00	*0.00*	0.48	0.00	0.00	0.00	0.00	*0.00*	0.00	0.00	0.00	0.00	0.00	*0.00*	0.00	0.00	0.00
Fe_2O_3	0.00	1.69	*0.00*	0.00	2.34	0.00	0.13	0.60	*0.00*	2.24	1.54	3.40	0.27	0.54	*0.00*	2.54	1.61	3.83
FeO	31.01	6.07	*5.66*	24.78	0.00	28.87	32.53	7.37	*7.71*	29.50	0.00	31.27	34.88	8.97	*9.39*	33.75	0.00	33.92
MnO	0.96	0.00	*0.00*	0.17	0.00	0.23	0.67	0.00	*0.00*	0.00	0.00	0.00	1.47	0.00	*0.00*	0.00	0.00	0.00
MgO	6.60	10.32	*10.06*	17.33	0.00	18.10	5.82	8.76	*8.78*	14.91	0.00	15.25	3.70	7.58	*7.75*	12.66	0.00	12.94
CaO	0.85	0.00	*0.00*	0.49	4.65	0.10	1.07	0.00	*0.00*	0.08	8.45	0.16	0.98	0.00	*0.00*	0.10	7.28	0.12
Na_2O	0.00	0.53	*0.00*	0.00	8.47	0.00	0.00	0.46	*0.00*	0.00	7.01	0.00	0.00	0.58	*0.00*	0.00	7.78	0.00
K_2O	0.00	0.02	*0.00*	0.00	0.30	0.00	0.00	0.01	*0.00*	0.00	0.16	0.00	0.00	0.01	*0.00*	0.00	0.21	0.00
Totals	99.99	100.19		100.20	100.22	100.64	100.01	100.06		100.22	100.16	100.34	100.03	100.06		100.25	100.16	100.38
Nr. O	12	18	18	6	8	6	12	18	18	6	8	6	12	18	18	6	8	6
Si	3.00	5.23	*5.00*	1.82	2.80	1.97	2.98	5.15	*5.00*	1.84	2.60	1.92	2.97	5.16	*5.00*	1.87	2.66	1.90
Ti	0.00	0.00	*0.00*	0.00	0.00	0.00	0.00	0.00	*0.00*	0.00	0.00	0.00	0.00	0.00	*0.00*	0.00	0.00	0.00
Al	2.04	3.49	*4.00*	0.38	1.13	0.07	2.04	3.77	*4.00*	0.27	1.34	0.06	2.04	3.77	*4.00*	0.19	1.27	0.08
Cr	0.00	0.00	*0.00*	0.01	0.00	0.00	0.00	0.00	*0.00*	0.00	0.00	0.00	0.00	0.00	*0.00*	0.00	0.00	0.00
Fe^{3+}	0.00	0.13	*0.00*	0.01	0.08	0.00	0.01	0.05	*0.00*	0.07	0.05	0.10	0.02	0.04	*0.00*	0.08	0.05	0.11
Fe^{2+}	2.03	0.51	*0.48*	0.77	0.00	0.91	2.14	0.62	*0.66*	0.95	0.00	1.02	2.34	0.76	*0.81*	1.12	0.00	1.13
Mn	0.06	0.00	*0.00*	0.01	0.00	0.01	0.04	0.00	*0.00*	0.00	0.00	0.00	0.10	0.00	*0.00*	0.00	0.00	0.00
Mg	0.77	1.55	*1.52*	0.97	0.00	1.03	0.68	1.31	*1.34*	0.86	0.00	0.89	0.44	1.15	*1.19*	0.75	0.00	0.77
Ca	0.07	0.00	*0.00*	0.02	0.22	0.00	0.09	0.00	*0.00*	0.00	0.41	0.01	0.08	0.00	*0.00*	0.00	0.35	0.01
Na	0.00	0.10	*0.00*	0.00	0.73	0.00	0.00	0.09	*0.00*	0.00	0.61	0.00	0.00	0.11	*0.00*	0.00	0.68	0.00
K	0.00	0.00	*0.00*	0.00	0.02	0.00	0.00	0.00	*0.00*	0.00	0.01	0.00	0.00	0.00	*0.00*	0.00	0.01	0.00
Sum	7.98	11.01	*11.00*	3.98	4.97	3.99	7.99	10.99	*11.00*	3.99	5.02	4.00	8.00	10.99	*11.00*	4.00	5.02	4.00
X_{Mg}	0.28	0.75	*0.76*	0.56		0.53	0.24	0.68	*0.67*	0.47		0.46	0.16	0.60	*0.60*	0.40		0.40
$y(Opx)_1$				0.19		0.03				0.13		0.03				0.09		0.04
X_{Ab}					0.75						0.59						0.65	
X_{An}					0.23						0.40						0.34	
X_{Or}					0.02						0.01						0.01	

*Modified ideal stoichiometric cordierite

Table 5.2 continued: Average mineral chemistry for coronas SK9B and SK9C

	SK9B								SK9C					
Analysis			Layer 1		Layer 2		Layer 3	Layer 4		Layer 1		Layer 2		Layer 3
Tag	***Grt***	***Crd***	***Crd****	***Opx***	***Pl***	***Opx***	***Kfs***	***Opx***	***Grt***	***Crd***	***Opx***	***Pl***	***Opx***	***Opx***
SiO_2	36.84	50.80	*48.30*	47.29	59.00	47.18	66.49	48.52	36.95	48.42	47.83	59.83	48.23	48.99
TiO_2	0.00	0.00	*0.00*	0.00	0.00	0.00	0.00	0.00	0.00	0.00	0.00	0.00	0.00	0.00
Al_2O_3	21.65	32.09	*32.78*	4.86	25.57	3.33	17.22	1.00	20.35	32.44	3.34	25.06	2.91	2.02
Cr_2O_3	0.00	0.00	*0.00*	0.00	0.04	0.00	0.00	0.00	0.07	0.00	0.32	0.00	0.15	0.00
Fe_2O_3	0.48	0.31	*0.00*	2.06	0.00	3.36	0.47	3.16	2.50	0.56	1.27	0.68	1.14	1.09
FeO	34.98	8.59	*9.24*	32.70	0.61	33.18	0.00	34.66	32.28	9.12	34.26	0.00	34.60	34.49
MnO	1.61	0.00	*0.00*	0.00	0.00	0.00	0.00	0.00	2.71	0.24	0.89	0.00	0.93	0.99
MgO	3.40	7.64	*7.78*	13.20	0.00	12.37	0.00	12.86	4.38	7.75	12.31	0.00	12.35	12.86
CaO	1.08	0.00	*0.00*	0.09	7.67	0.93	0.03	0.12	1.06	0.00	0.05	7.17	0.09	0.12
Na_2O	0.00	0.59	*0.00*	0.00	7.17	0.00	2.43	0.00	0.00	0.00	0.00	7.12	0.00	0.00
K_2O	0.00	0.01	*0.00*	0.00	0.04	0.00	13.42	0.00	0.00	0.00	0.00	0.19	0.00	0.00
Totals	100.04	100.03		100.21	100.11	100.34	100.05	100.32	100.31	98.52	100.28	100.05	100.39	100.56
Nr. O	12	18		6	8	6	8	6	12	18	6	8	6	6
Si	2.96	5.14	*5.00*	1.86	2.63	1.87	3.04	1.93	2.96	5.00	1.90	2.67	1.91	1.94
Ti	0.00	0.00	*0.00*	0.00	0.00	0.00	0.00	0.00	0.00	0.00	0.00	0.00	0.00	0.00
Al	2.05	3.83	*4.00*	0.22	1.35	0.16	0.93	0.05	1.92	3.95	0.16	1.32	0.14	0.09
Cr	0.00	0.00	*0.00*	0.00	0.00	0.00	0.00	0.00	0.00	0.00	0.01	0.00	0.00	0.00
Fe^{3+}	0.03	0.02	*0.00*	0.06	0.02	0.10	0.02	0.10	0.15	0.04	0.04	0.02	0.03	0.03
Fe^{2+}	2.35	0.73	*0.80*	1.08	0.00	1.10	0.00	1.15	2.16	0.79	1.14	0.00	1.15	1.14
Mn	0.11	0.00	*0.00*	0.00	0.00	0.00	0.00	0.00	0.18	0.02	0.03	0.00	0.03	0.03
Mg	0.41	1.15	*1.20*	0.77	0.00	0.73	0.00	0.76	0.52	1.19	0.73	0.00	0.73	0.76
Ca	0.09	0.00	*0.00*	0.00	0.37	0.04	0.00	0.01	0.09	0.00	0.00	0.34	0.00	0.01
Na	0.00	0.12	*0.00*	0.00	0.62	0.00	0.22	0.00	0.00	0.00	0.00	0.62	0.00	0.00
K	0.00	0.00	*0.00*	0.00	0.00	0.00	0.78	0.00	0.00	0.00	0.00	0.01	0.00	0.00
Sum	8.00	11	*11.00*	4.00	4.99	4.00	66.49	4.00	8.00	11.00	4.00	4.98	4.00	4.00
X_{Mg}	0.15	0.61		0.00				0.40	0.19	0.60	0.39		0.39	0.40
$y(Opx)_1$				0.00				0.02			0.08		0.07	0.05
X_{Ab}					0.63		0.22					0.64		
X_{An}					0.37		0.00					0.35		
X_{Or}					0.00		0.78					0.01		

*Modified ideal stoichiometric cordierite

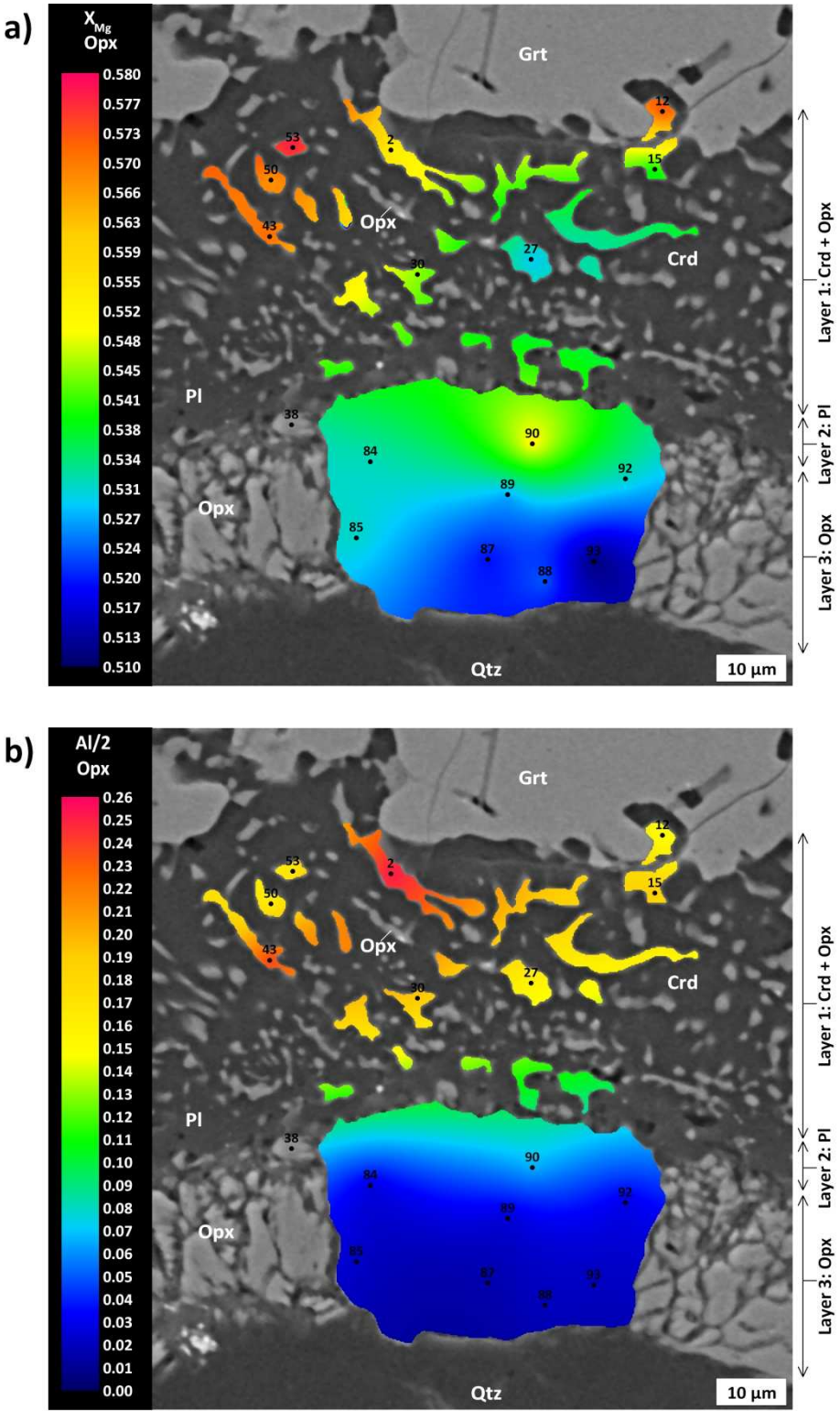

Figure 5.4: SK8C gridded and contoured mineral compositions for (a) orthopyroxene X_{Mg} and (b) orthopyroxene c.Al/2. Numbered tags in the images correspond with individual analyses in Appendix B.

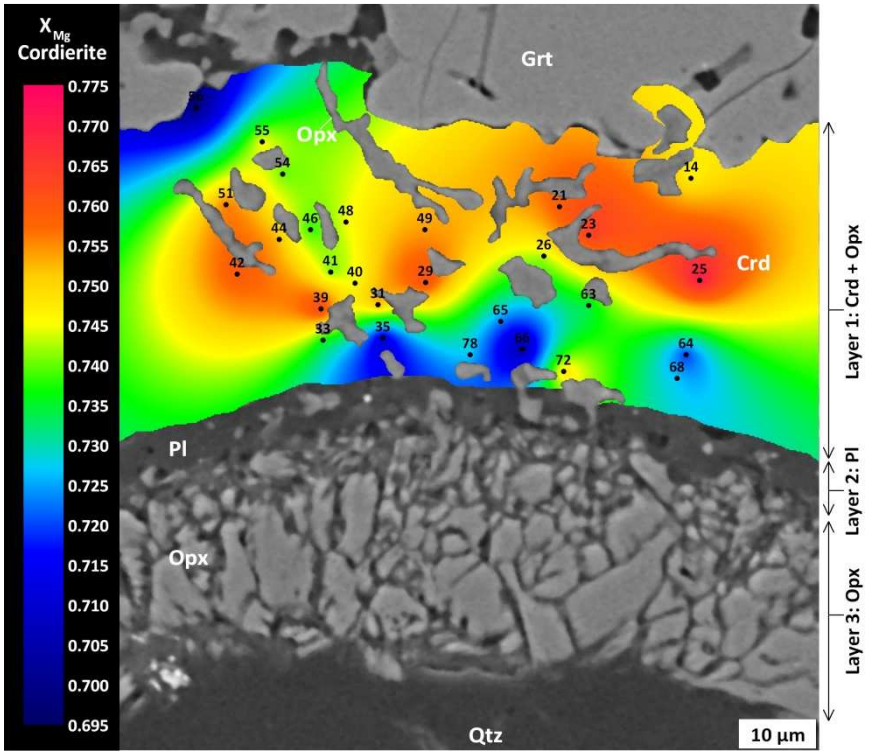

Figure 5.5: SK8C gridded and contoured mineral compositions for layer 1 cordierite X_{Mg}. Numbered tags in the images correspond with individual analyses in Appendix B.

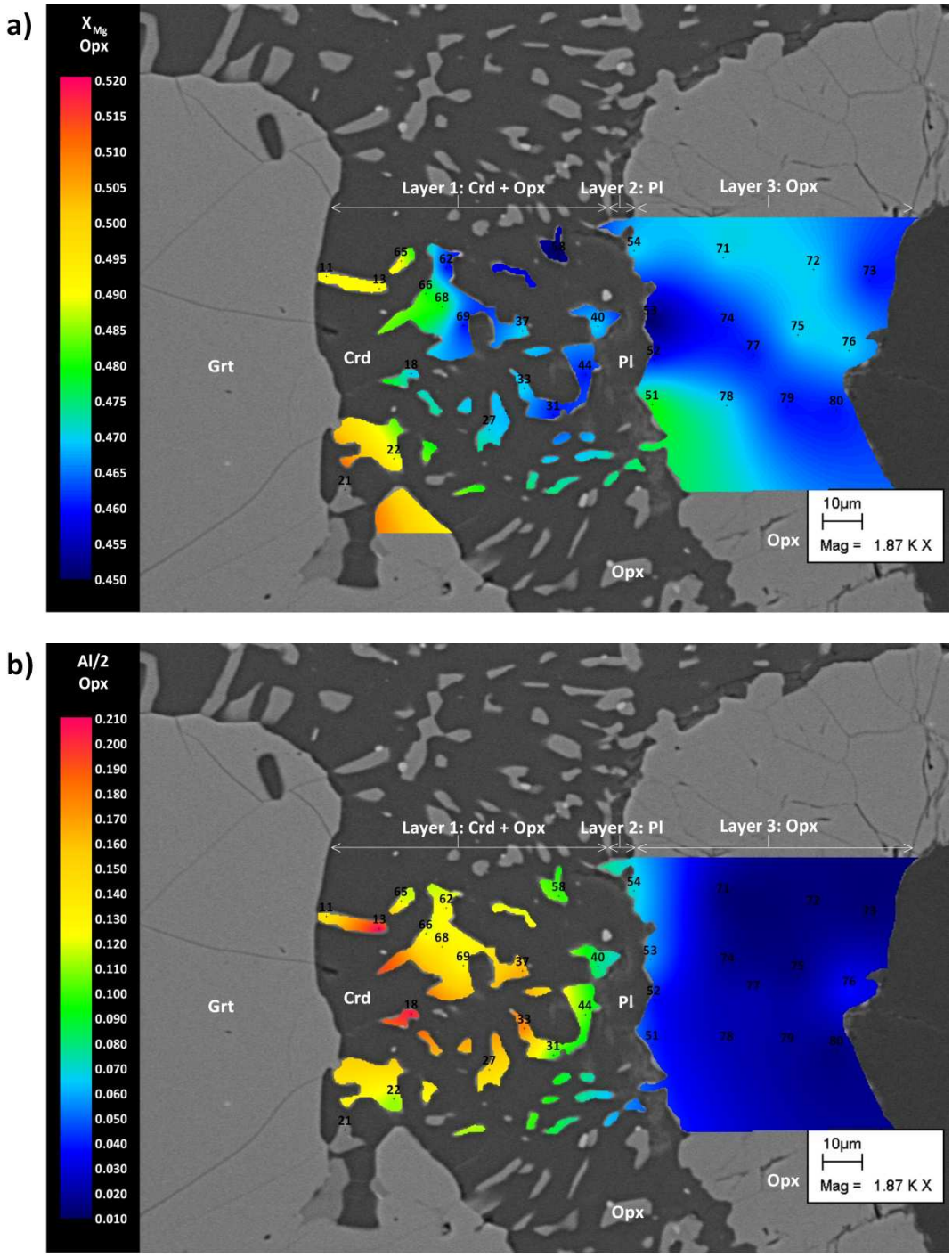

Figure 5.6: SK12A gridded and contoured mineral compositions for (a) orthopyroxene X_{Mg} and (b) orthopyroxene c.Al/2. Numbered tags in the images correspond with individual analyses in Appendix B.

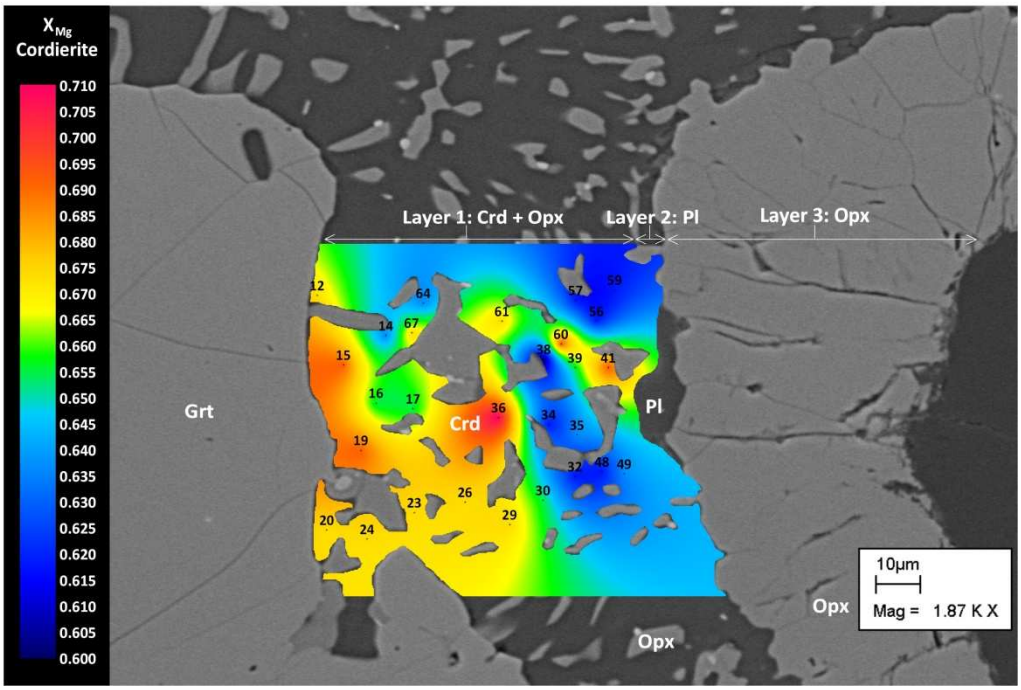

Figure 5.7: SK12A gridded and contoured mineral compositions for layer 1 cordierite X_{Mg}. Numbered tags in the images correspond with individual analyses in Appendix B.

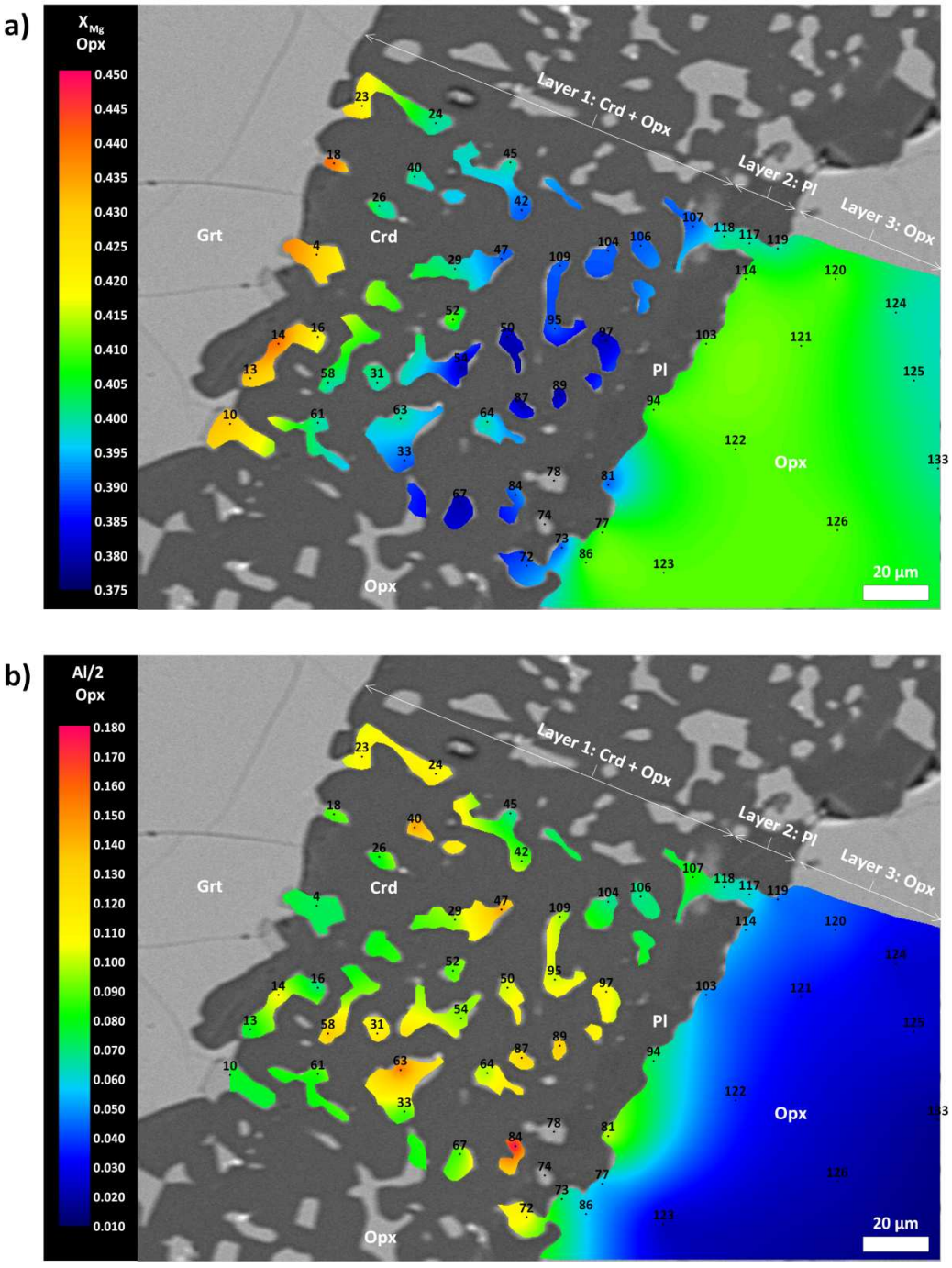

Figure 5.8: SK9A gridded and contoured mineral compositions for (a) orthopyroxene X_{Mg} and (b) orthopyroxene c.Al/2. Numbered tags in the images correspond with individual analyses in Appendix B.

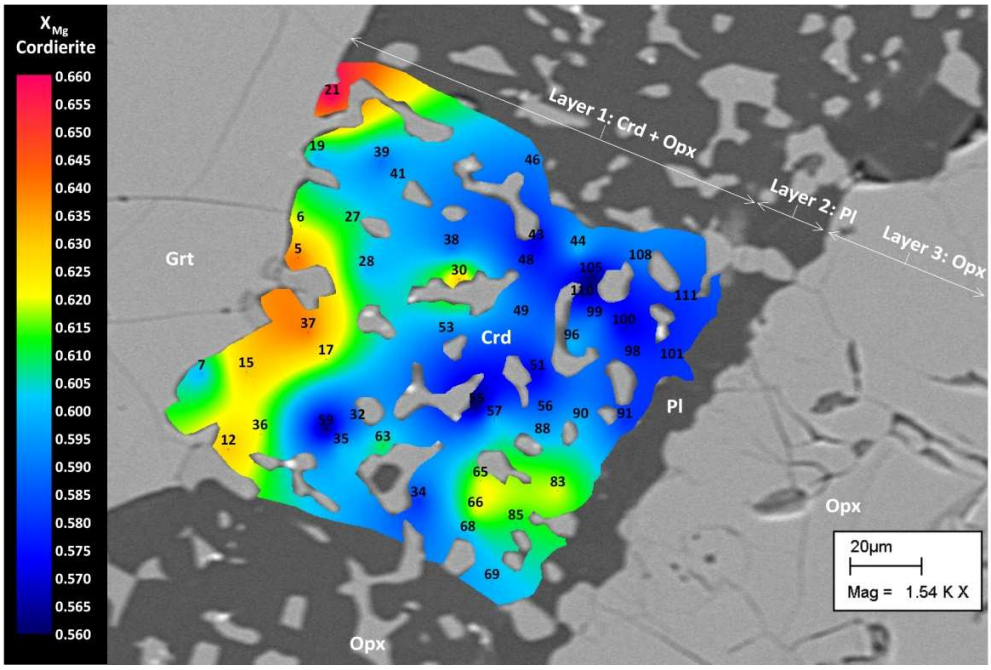

Figure 5.9: SK9A gridded and contoured mineral compositions for layer 1 cordierite $X_{Mg.}$ Numbered tags in the images correspond with individual analyses in Appendix B.

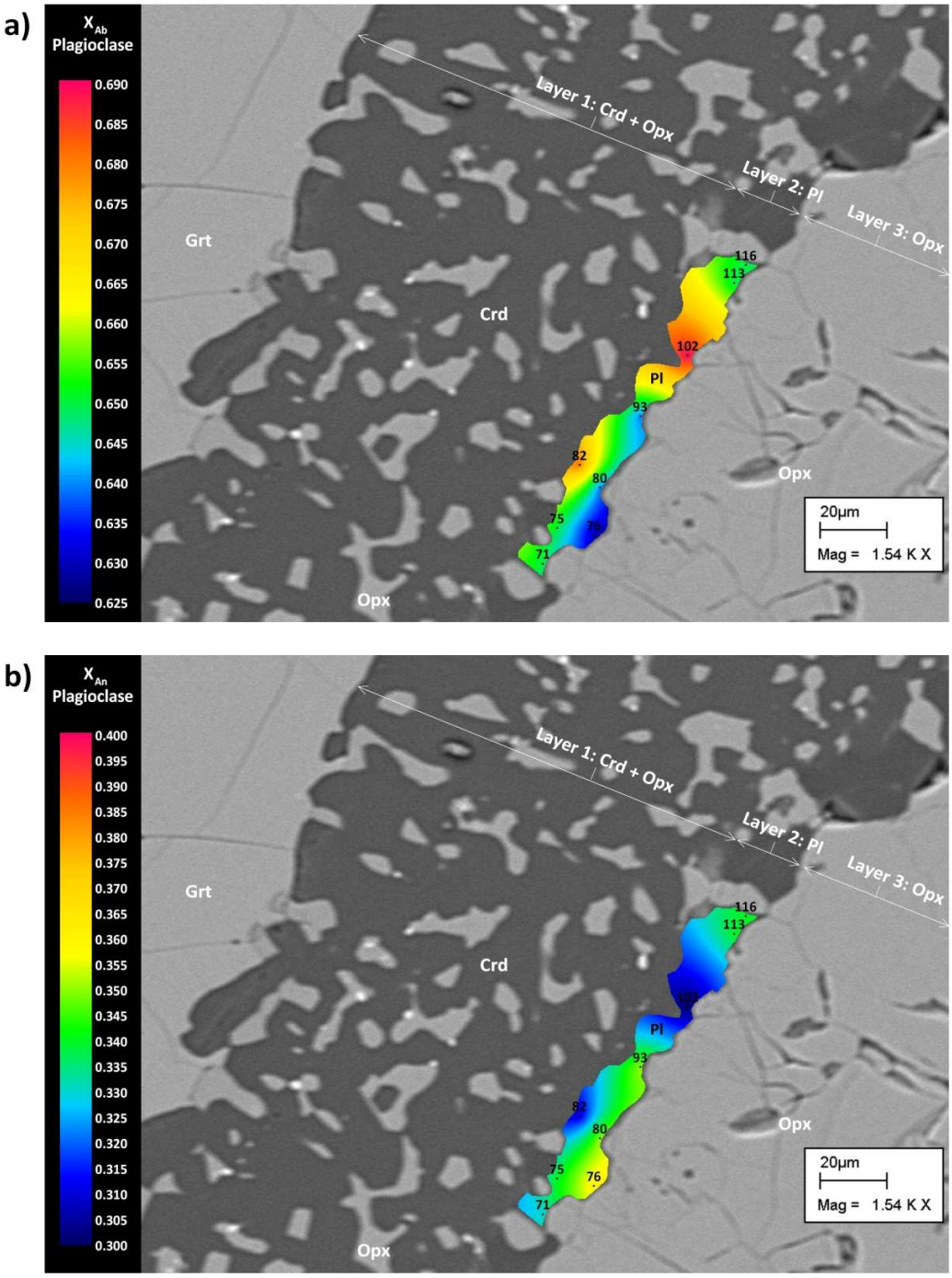

Figure 5.10: SK9A gridded and contoured mineral compositions for (a) layer 2 plagioclase X_{Ab} and (b) layer 2 plagioclase X_{An}. Numbered tags in the images correspond with individual analyses in Appendix B.

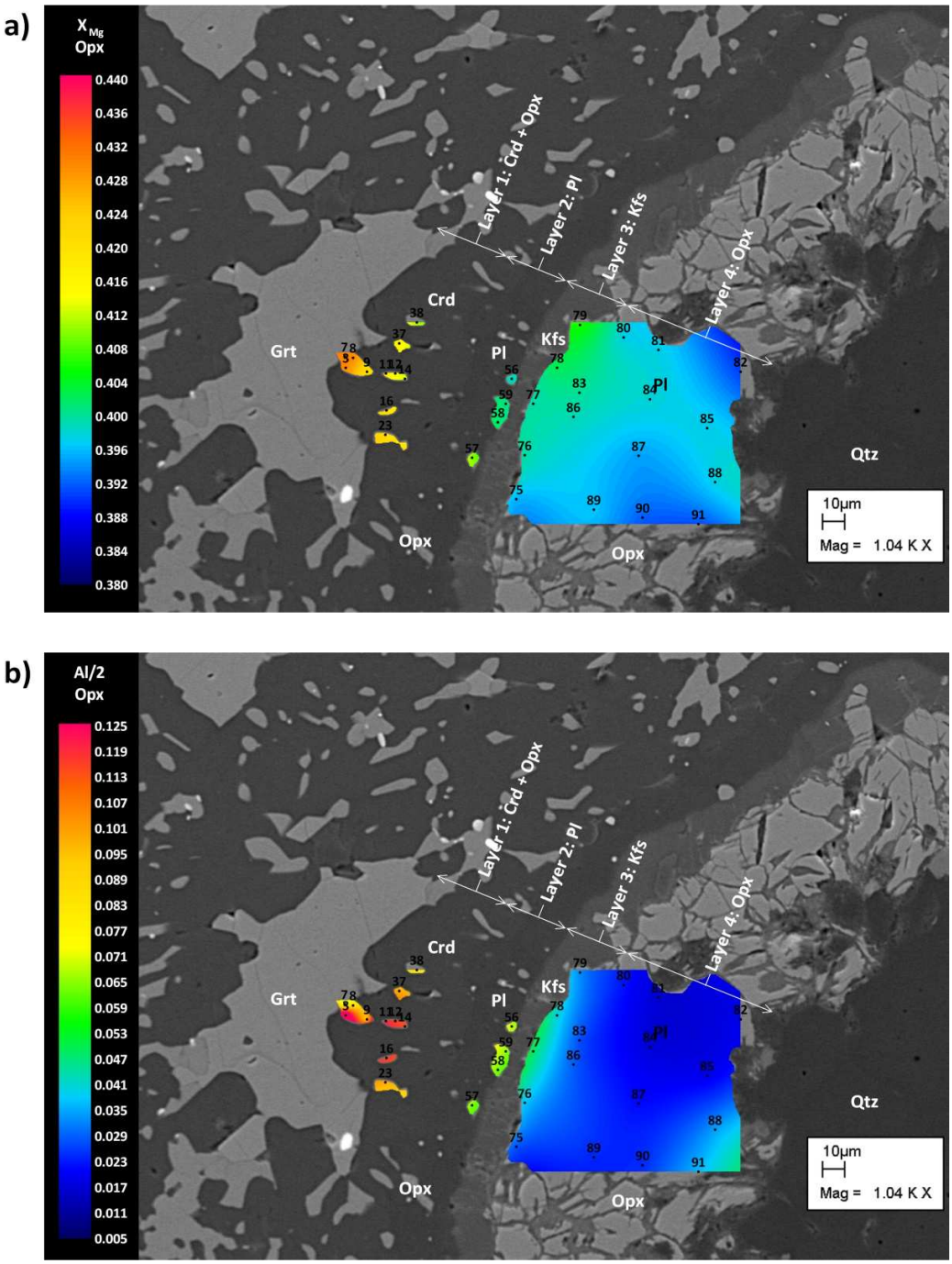

Figure 5.11: SK9B gridded and contoured mineral compositions for (a) orthopyroxene X_{Mg} (b) orthopyroxene c.Al/2. Numbered tags in the images correspond with individual analyses in Appendix B.

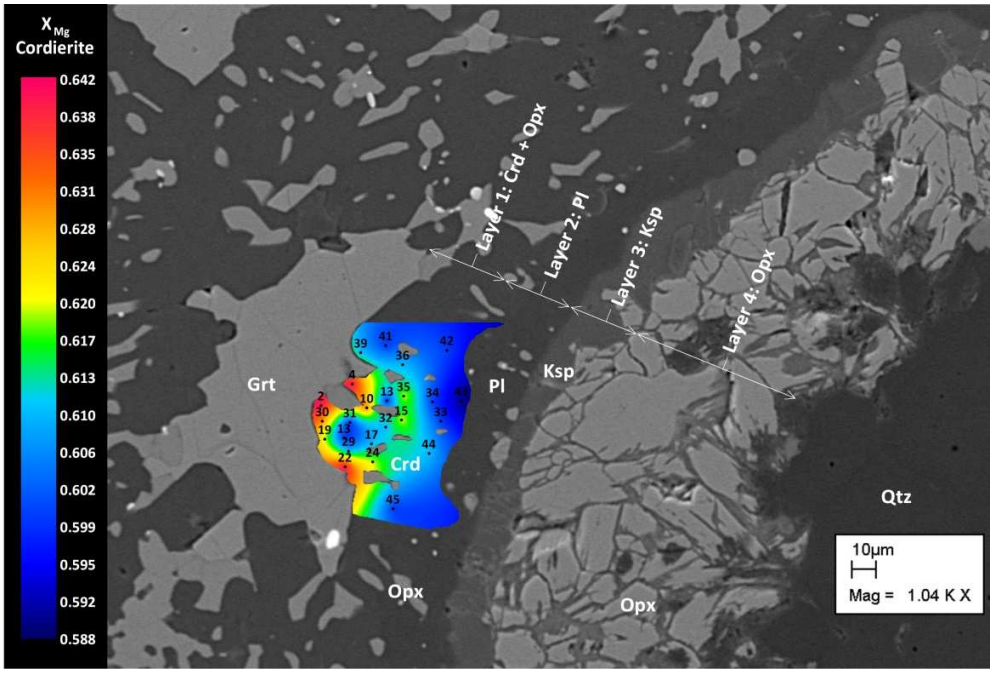

Figure 5.12: SK9B gridded and contoured mineral compositions for layer 1 cordierite X_{Mg}. Numbered tags in the images correspond with individual analyses in Appendix B.

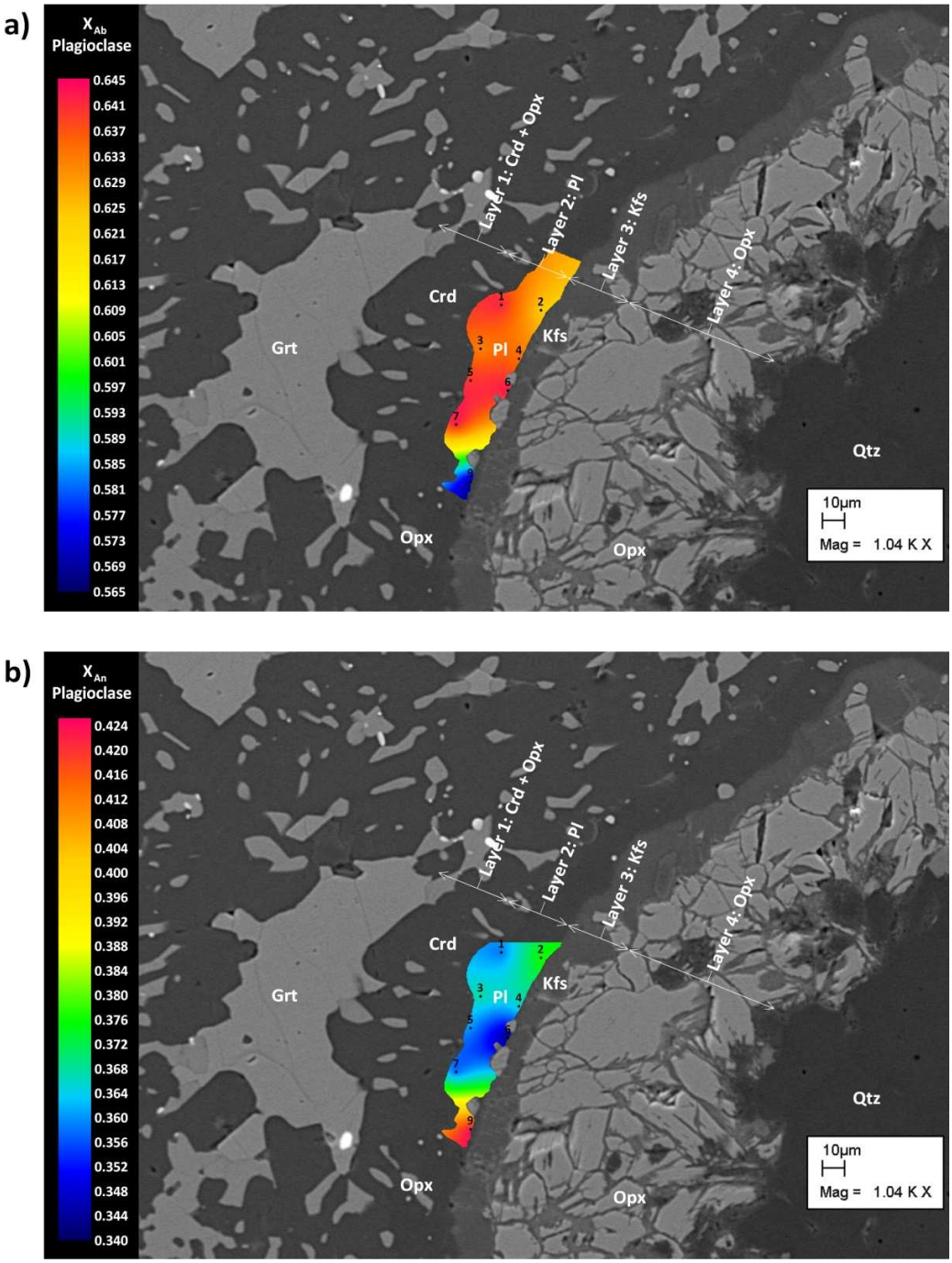

Figure 5.13: SK9B gridded and contoured mineral compositions for (a) layer 2 plagioclase X_{Ab} and (b) layer 2 plagioclase X_{An}. Numbered tags in the images correspond with individual analyses in Appendix B.

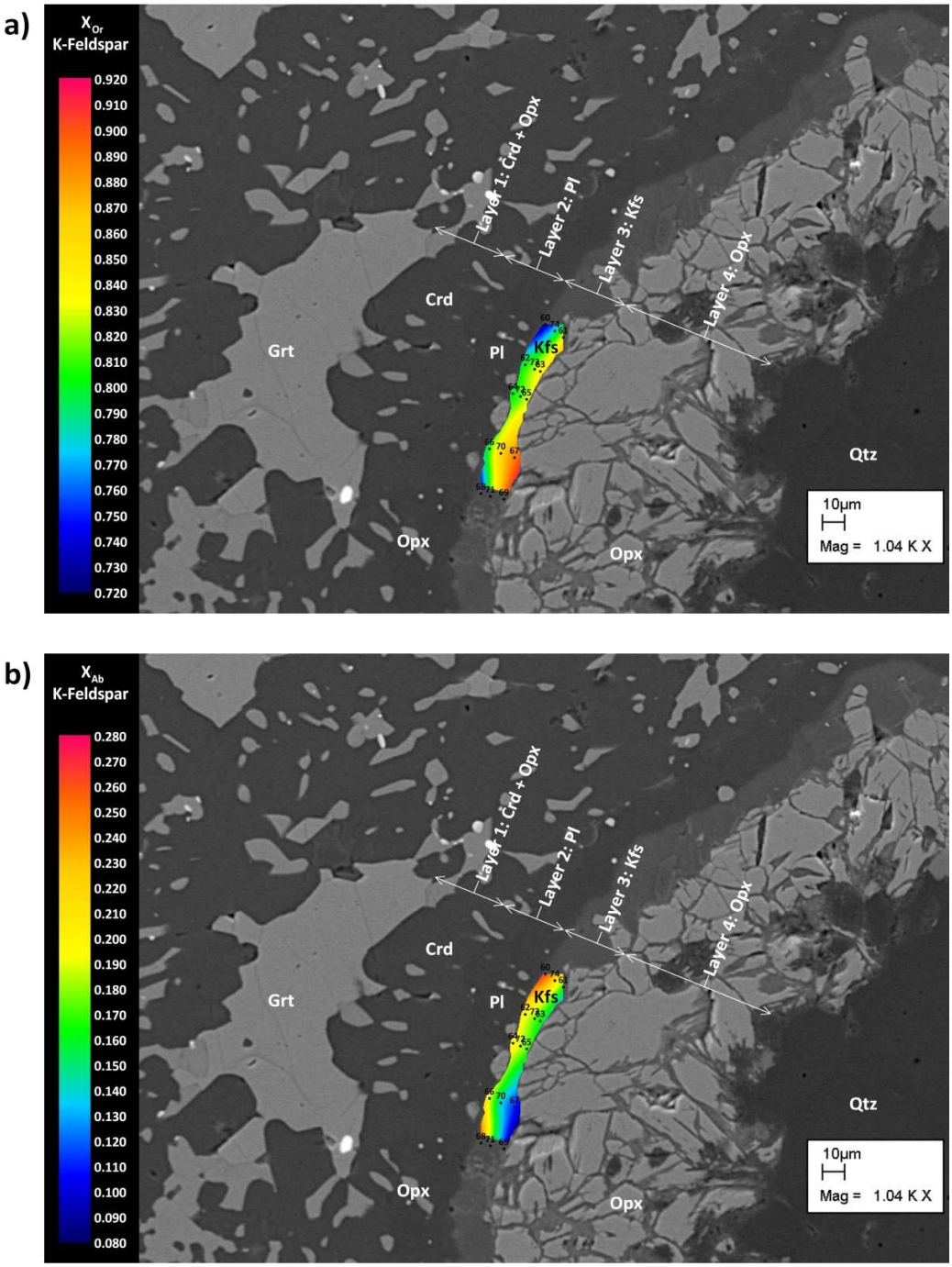

Figure 5.14: SK9B gridded and contoured mineral compositions for (a) layer 3 K-feldspar X_{Or} and (b) Layer 3 K-feldspar X_{Ab}. Numbered tags in the images correspond with individual analyses in Appendix B.

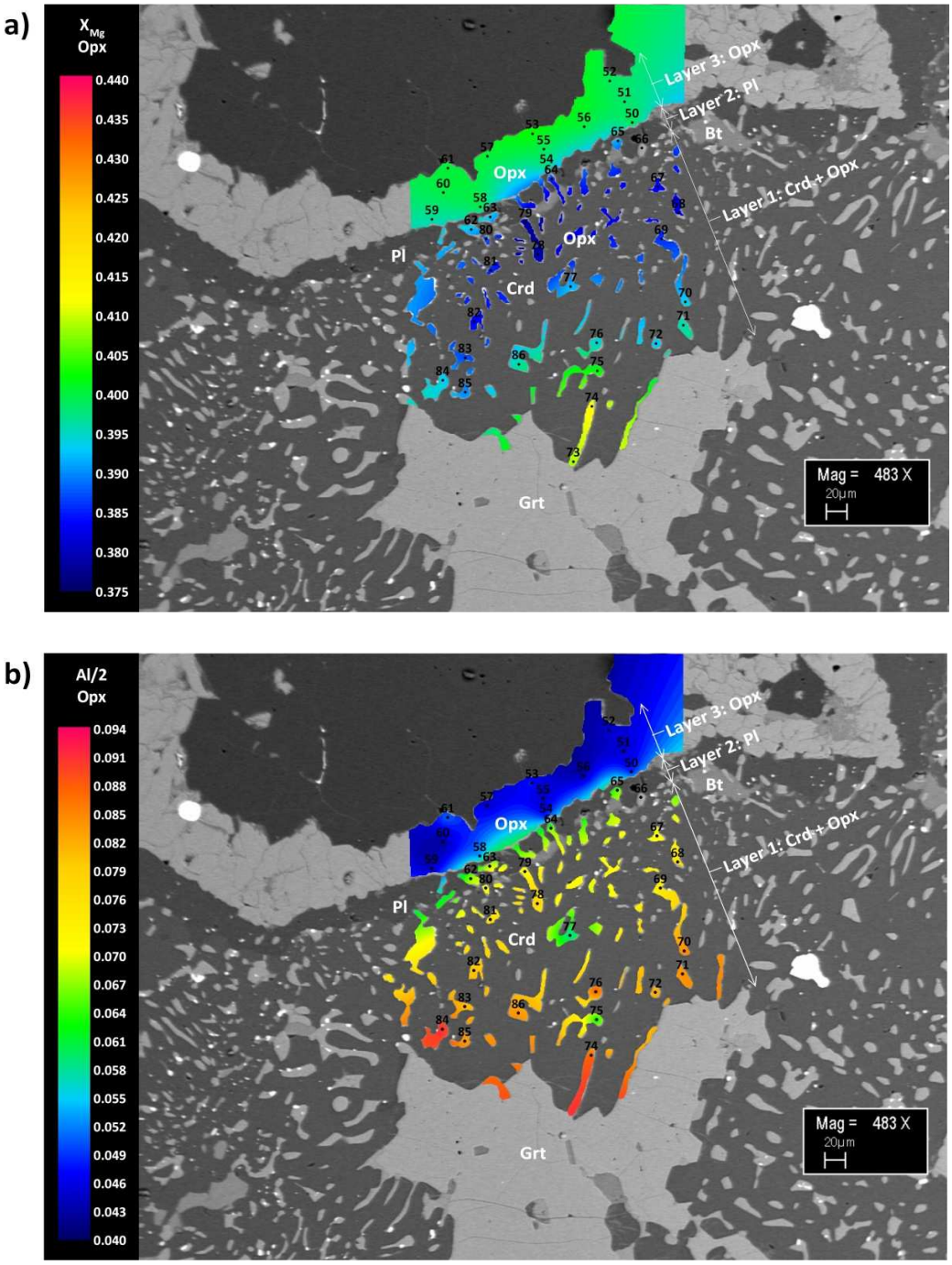

Figure 5.15: SK9C gridded and contoured mineral compositions for (a) orthopyroxene X_{Mg} and (b) orthopyroxene c.Al/2. Numbered tags in the images correspond with individual analyses in Appendix B.

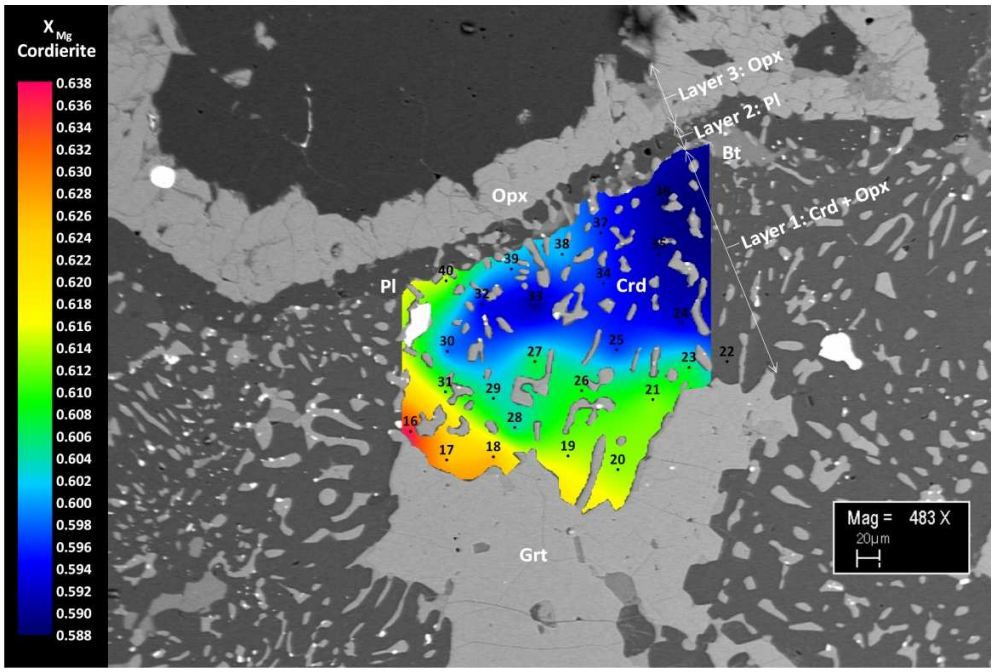

Figure 5.16: SK9C gridded and contoured mineral compositions for layer 1 cordierite X_{Mg}. Numbered tags in the images correspond with individual analyses in Appendix B.

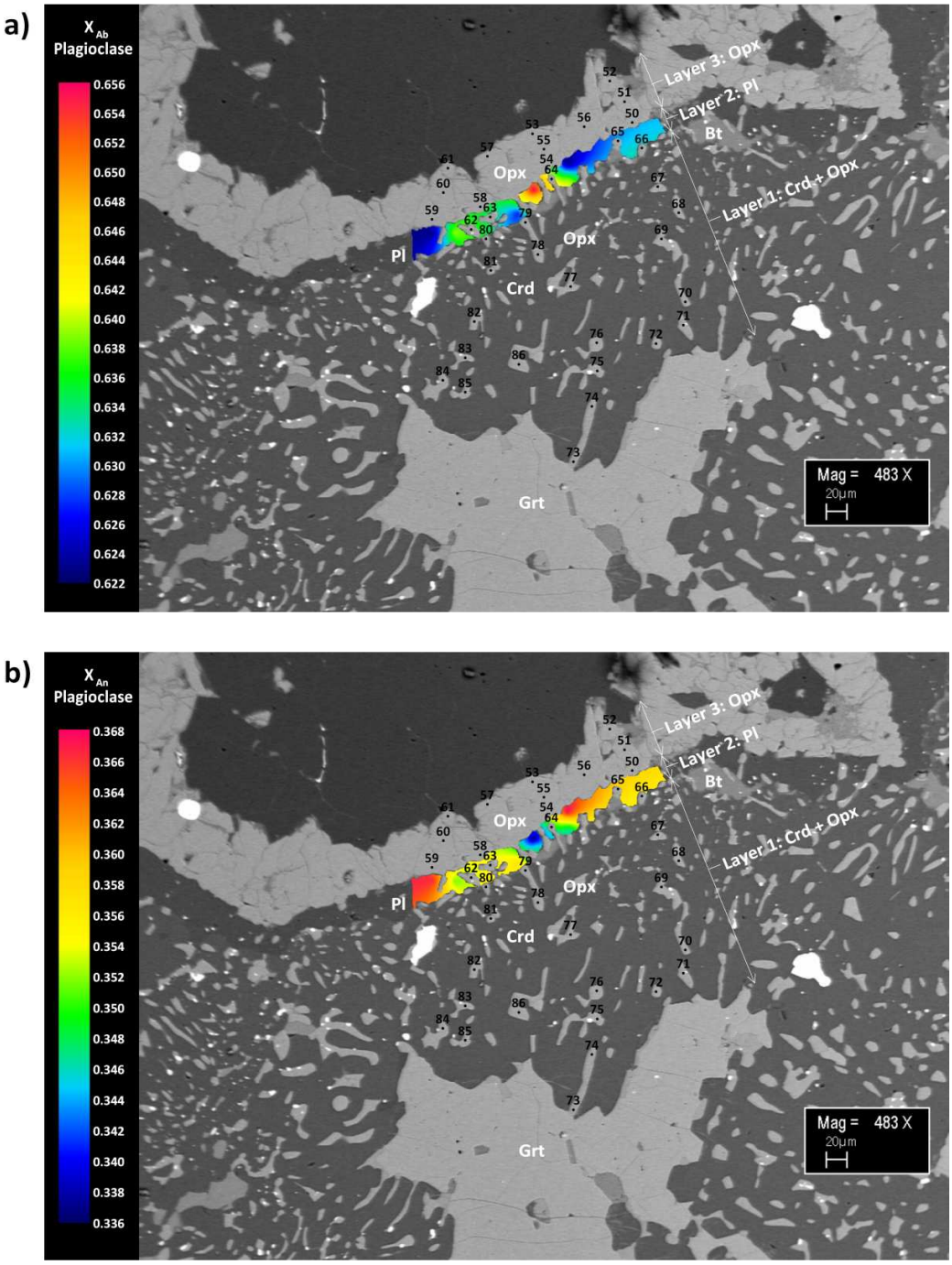

Figure 5.17: SK9C gridded and contoured mineral compositions for (a) layer 2 plagioclase X_{Ab} and (b) layer 2 plagioclase X_{An}. Numbered tags in the images correspond with individual analyses in Appendix B.

5.2.1 Compositional variation in corona product phases

Summary descriptive statistics for corona mineral compositions are included in Table 5.3 and Table 5.4. The standard deviation and, to a lesser extent, the range, demonstrate compositional variability of corona product phases. Lower standard deviations imply less compositional variation in a phase within a corona and, thus, lower attendant chemical potential gradients and greater equilibration within a layer. Standard deviation thus serves as a proxy for extent of equilibration both within a layer and across the corona as a whole. Standard deviations for layer 1 cordierite X_{Mg} and orthopyroxene X_{Mg} and $y(Opx)_1$ are plotted for all coronas in Figure 5.18.

In layer 1 symplectites (Figure 5.18), standard deviation is lowest in SK9C for Al content and X_{Mg} in orthopyroxene and X_{Mg} in cordierite. SK8C and SK12A exhibit a tendency toward higher standard deviations compared to SK9 coronas, but not exclusively (X_{Mg} standard deviation for cordierite in SK9A exceeds that of SK8C and SK12A). The high standard deviation for $y(Opx)_1$ in SK9B is not considered significant owing to the comparatively low sample population (n = 11).

In plagioclase layer 2 (Figure 5.19), the standard deviations are generally higher for X_{Ab} compared to X_{An}. SK12A standard deviation is not considered representative owing to the low sample population (n = 4). Standard deviations for both X_{Ab} and X_{An} are highest in SK8C (X_{Ab} = 0.090, X_{An} = 0.069) and lowest in SK9C (X_{Ab} = 0.011, X_{An} = 0.010). SK9B standard deviations for X_{Ab} (0.022) and X_{An} (0.022) are both slightly higher than for SK9A, for which both X_{Ab} and X_{An} standard deviations are 0.019.

For blocky orthopyroxene (Figure 5.20), SK8C shows markedly higher standard deviations for X_{Mg} (0.011) compared to all other coronas, as well as for $y(Opx)_1$ (0.021) compared to all other coronas except SK9A (0.024). Conversely, SK9C exhibits the lowest standard deviations for X_{Mg} (0.002) and $y(Opx)_1$ (0.003). Standard deviations for X_{Mg} and $y(Opx)_1$ in SK9B are next lowest, whereas SK9A and SK12A exhibit intermediate values. The standard deviations for $y(Opx)_1$ are significantly larger than X_{Mg} for all phases in all layers in all coronas.

Table 5.3: Summary statistics of mineral chemistry for coronas SK8C, SK12A, SK9A, SK9B and SK9C.

	MEAN					RANGE					STD DEV				
	SK8C	**SK12A**	**SK9A**	**SK9B**	**SK9C**	**SK8C**	**SK12A**	**SK9A**	**SK9B**	**SK9C**	**SK8C**	**SK12A**	**SK9A**	**SK9B**	**SK9C**
LAYER 1 CRD-OPX SYMPLECTITE															
X_{Mg} **Crd**	0.742	0.680	0.601	0.613	0.602	0.072	0.060	0.102	0.046	0.025	0.019	0.016	0.023	0.014	0.008
X_{Mg} **Opx**	0.557	0.475	0.401	0.418	0.390	0.062	0.070	0.059	0.032	0.034	0.018	0.017	0.017	0.009	0.008
$y(Opx)_1$	0.188	0.135	0.094	0.112	0.078	0.106	0.131	0.095	0.129	0.034	0.039	0.036	0.022	0.041	0.009
LAYER 2 PLAGIOCLASE															
X_{Ab} **Pl**	0.707	0.595	0.653	0.627	0.636	0.266	0.030	0.060	0.074	0.033	0.090	0.013	0.019	0.022	0.011
X_{An} **Pl**	0.265	0.400	0.336	0.370	0.354	0.202	0.030	0.060	0.081	0.031	0.069	0.014	0.019	0.022	0.010
LAYER 2 ORTHOPYROXENE															
X_{Mg} **Opx**				0.400	0.389				0.041	0.010				0.018	0.004
$y(Opx)_1$				0.078	0.068				0.026	0.004				0.011	0.002
BLOCKY ORTHOPYROXENE															
X_{Mg} **Opx**	0.529	0.465	0.405	0.398	0.399	0.039	0.030	0.022	0.017	0.006	0.011	0.008	0.007	0.005	0.002
$y(Opx)_1$	0.034	0.028	0.042	0.023	0.047	0.122	0.056	0.087	0.026	0.011	0.021	0.018	0.024	0.008	0.003
ALL ORTHOPYROXENE															
X_{Mg} **Opx**	0.542	0.471	0.402	0.405	0.393	0.066	0.070	0.060	0.050	0.034	0.020	0.014	0.015	0.014	0.008
$y(Opx)_1$	0.106	0.087	0.076	0.061	0.066	0.236	0.196	0.134	0.186	0.049	0.085	0.061	0.033	0.048	0.016

Table 5.4: Number of analytical points for each phase in all coronas

	SK8C	SK12A	SK9A	SK9B	SK9C
Layer 1: cordierite	25	28	43	24	21
Layer 1: orthopyroxene	8	17	32	11	19
Layer 2: plagioclase	7	4	9	10	9
Layer 2: orthopyroxene	-	-	-	4	5
Layer 3: K-feldspar	-	-	-	5	-
Blocky orthopyroxene	9	14	16	17	12

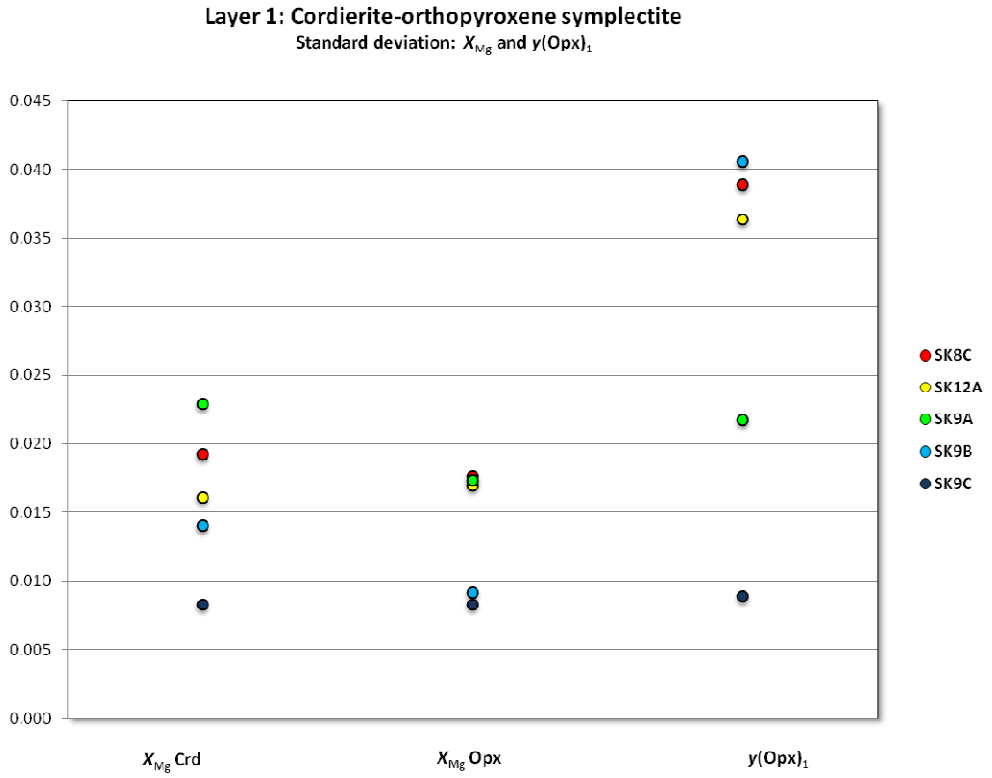

Figure 5.18: X_{Mg} (cordierite and orthopyroxene) and $y(Opx)_1$ standard deviations for layer 1 cordierite-orthopyroxene symplectite.

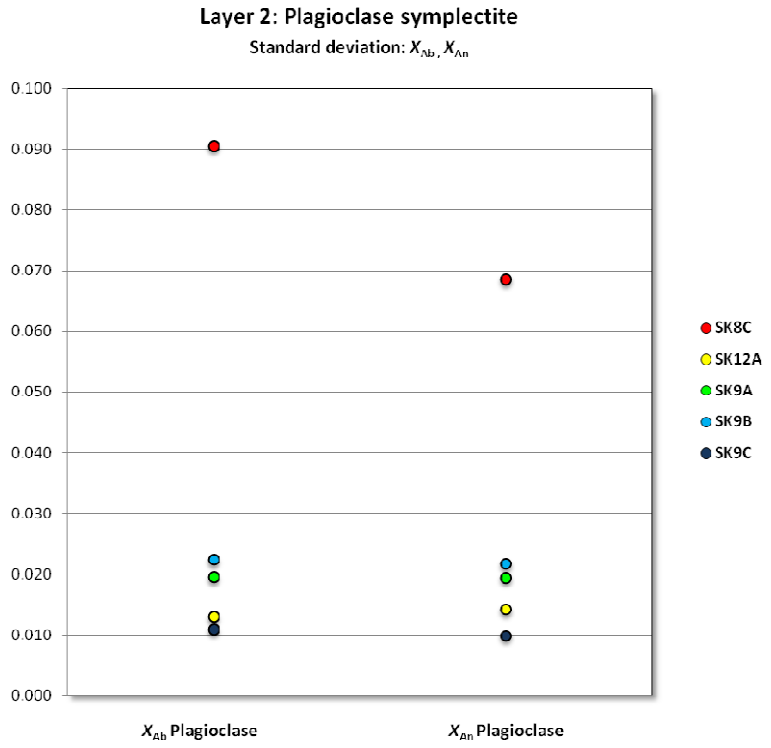

Figure 5.19: X_{Ab} and X_{An} standard deviations for layer 2 plagioclase.

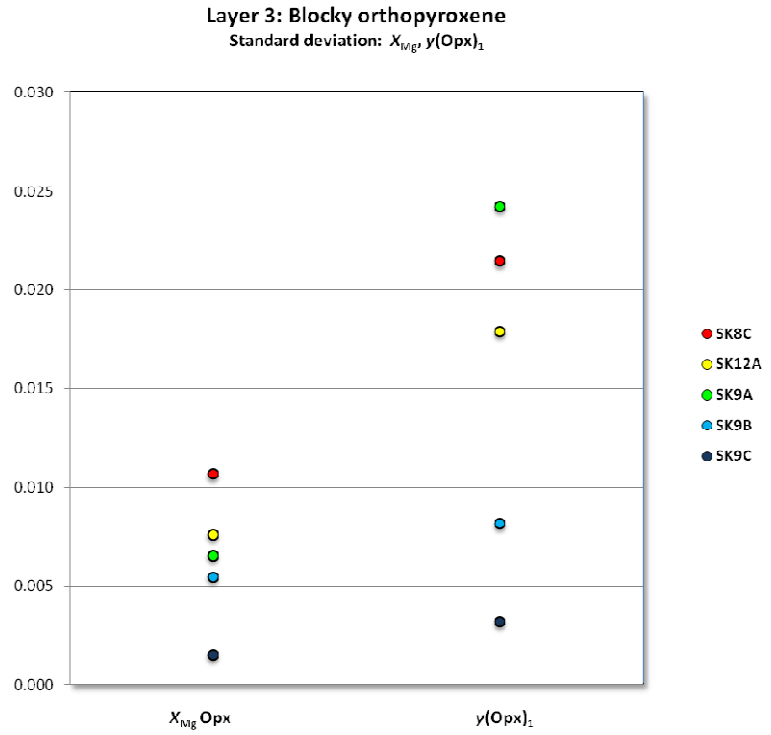

Figure 5.20: X_{Mg} and $y(Opx)_1$ standard deviations for layer 3 blocky orthopyroxene.

The standard deviation for all corona orthopyroxene, i.e., analyses for symplectite and blocky orthopyroxene combined (Figure 5.21), is more diagnostic of equilibration in the corona as a whole. Orthopyroxene X_{Mg} standard deviation in SK8C (0.020) far exceeds SK12A (0.014), SK9B (0.014) and SK9A (0.015). Lowest X_{Mg} standard deviation is in SK9C (0.008). With respect to Al content, the order of increasing standard deviations in *y*(Opx) is: SK8C (0.085) > SK12A (0.061) > SK9B (0.048) > SK9A (0.033) > SK9C (0.016). If standard deviation serves as a valid proxy for extent of equilibration, then the order of increasing equilibration is as follows: SK8C → SK12A → SK9B → SK9A → SK9C.

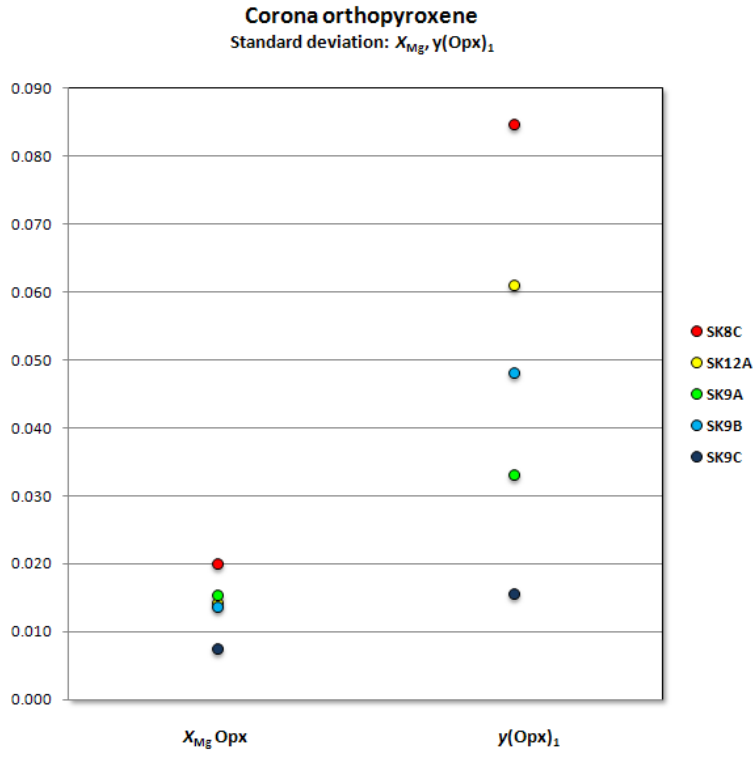

Figure 5.21: X_{Mg} and y(Opx)$_1$ standard deviations for orthopyroxene across all layers in the coronas.

Variation in composition of cordierite and orthopyroxene is compared with variation observed in coronas reviewed in the literature in Figure 5.22. Comparable magnitudes of X_{Mg} variation are observed in the Vredefort coronas relative to

reviewed coronas (Figure 5.22a). Inconsistency in the manner in which Al content in orthopyroxene is formulated in the latter (see Chapter 3, Section 3.7), prevents comparison of the Vredefort coronas with a representative population in the literature (Figure 5.22b). Asymmetric zonation in phase compositions across the coronas supports a single-stage, steady-state, diffusion-controlled origin for corona development during post-shock metamorphism in the Steynskraal traverse (Chapter 3, Section 3.4).

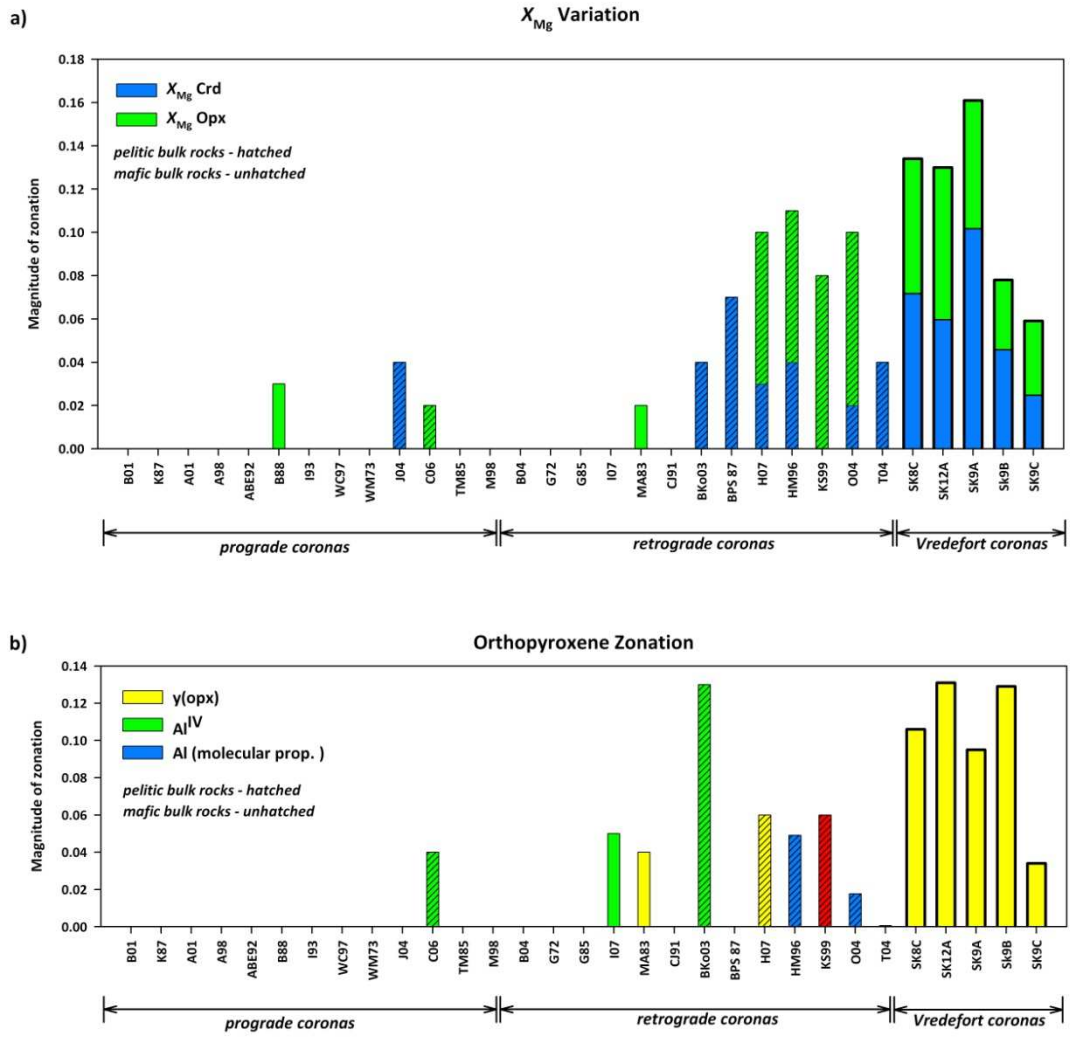

Figure 5.22: Comparison of zonation in (a) X_{Mg} for cordierite and orthopyroxene and (b) Al content in orthopyroxene for Vredefort coronas modelled and coronas reviewed in the literature. Zonation in cordierite and orthopyroxene X_{Mg} for the Vredefort coronas is comparable with that documented for prograde and retrograde coronas from the literature. Only two coronas in the literature formulated Al content in the same manner as this study, negating representative comparison.

5.2.2 Evidence for open-system behaviour in corona phase compositions – implications for calculation of the overall corona reaction

Conservation of components during corona reaction has important implications for the method used in determining the overall corona reaction. If the system is closed to all components, then the overall reaction is uniquely defined if the number of components is one less than the number of minerals. Some authors (e.g., Nishiyama, 1983) combined components together (e.g., FeO + MgO) in preventing the system from being underdetermined. The solution derived for the overall reaction, assuming a closed system, should produce the corona product minerals in the proportions in which they are observed. Predicted corona product proportions are commonly inconsistent with measured modes, negating closed-system behaviour (Ashworth and Sheplev, 1997). An alternative approach was adopted by other workers (Joesten and Fisher, 1988; Ashworth and Birdi, 1990; Johnson and Carlson, 1990; Carlson and Johnson, 1991) in which the measured proportions of the phases were used to reconstruct the overall reaction in an open system, with boundary fluxes accommodating metasomatic exchange with the surrounding rock. To ensure the system is not underdetermined, the reaction coefficient for one of the reactants was arbitrarily assigned as 1. Calculation requires one more constraint for a unique solution for the overall reaction. Carlson and Johnson (1991) used a constant-volume constraint to establish the proportions of reactant minerals consumed. In the case of Ashworth and Birdi (1990), closure of the system to Al and Si enabled reconstruction of the overall reaction without having to assume the original proportions in which the two reactants were consumed.

Before deciding if constant volume or closure for Al or Si is to be used as a valid constraint for unique solution of the overall reaction, the extent of open-system exchange of these components with the surrounding matrix must be assessed. Isocon plots allow the quantification of mobility or immobility of components within the corona (Grant, 1986) and a test of open- or closed-system behaviour (Figure 5.23). The line of equality in the graph indicates constant Al and Si in reactant and products. Conservation of Al and Si can only occur if the product is a symplectite in which product proportions can vary in such a manner that their combined Al/Si ratio

reflects that of the contiguous reactant. Unless a monomineralic product band fortuitously has the same Al/Si ratio as the reactant, the presence of a monomineralic band adjacent to the aluminous reactant is indicative of open-system behaviour for Al and Si (Ashworth and Birdi, 1990). If a symplectite inherits the Al/Si ratio of the reactant, i.e., clusters close to or near to the line of equality in the isocon plot, Ashworth and Birdi (1990) inferred that Al and Si were conserved in reaction (Figure 5.23).

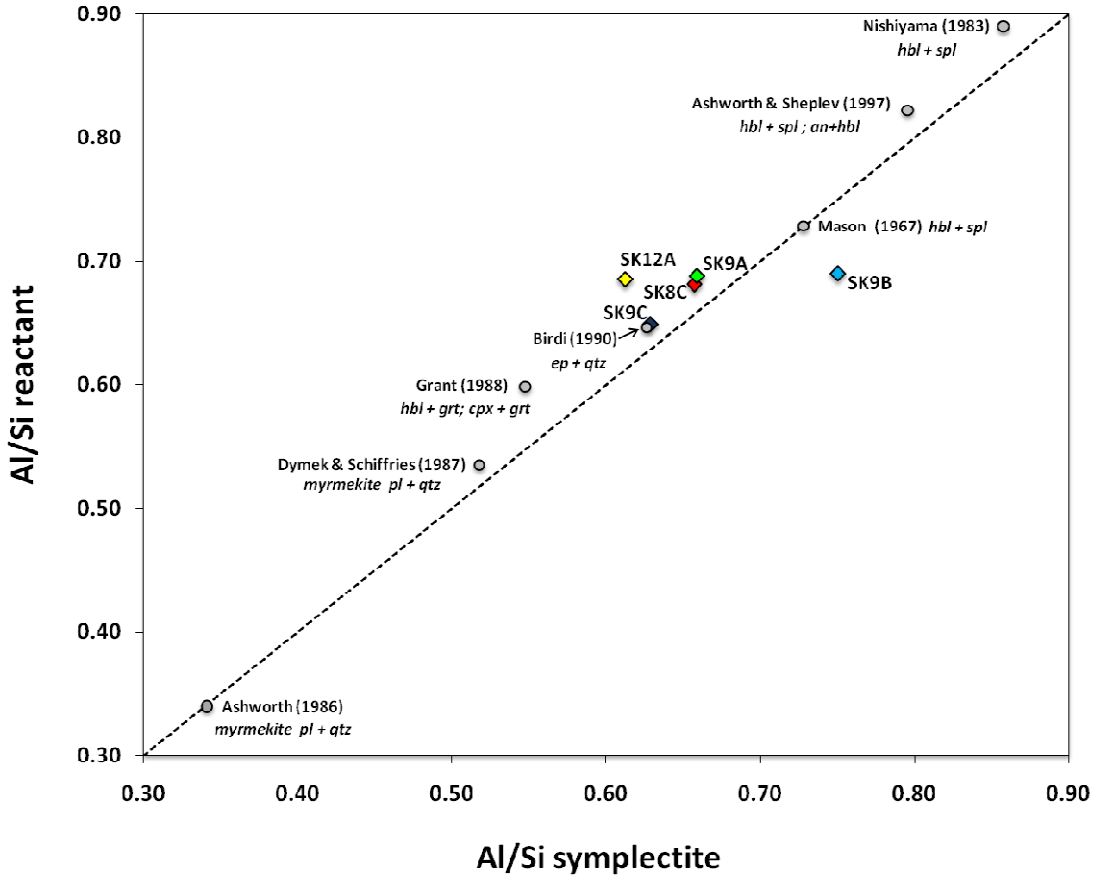

Figure 5.23: Isocon plot of Al/Si ratios in analysed symplectites from this study compared with symplectites reported by Ashworth and Birdi (1990). Symplectite mineralogy is indicated in italics below each data point. Departure from the equality line implies metasomatic exchange of Al and Si with the surrounding matrix. Since the coronas in this study plot off the equality line, the assumption of constant Al and Si could not be made in constructing a unique solution for the overall corona reaction.

The symplectites from SK8C, SK12A, SK9A and SK9C plot above the line of equality (Figure 5.23) and, like the majority of symplectites reviewed in the literature, appear to have either lost Al relative to Si from the system or gained Si relative to Al during reaction (Figure 5.23). In contrast, SK9B plots under the equality line (Figure 5.23), indicative of a nett gain of Al or loss of Si into the system though metasomatic exchange with the enclosing matrix. This is consistent with high modes of K-feldspar and plagioclase in the corona assemblage, not accommodated in the pure garnet-quartz corona bulk composition. The failure to conserve Al and Si in the stoichiometric proportions of the reactant (particularly in SK12A and SK9B) suggests a critical departure from closed-system behaviour in the systems under investigation, and negates the assumption of closure to Al and Si in defining the overall corona reaction. The evidence for open-system behaviour for Al and Si requires that the constant-volume constraint adopted by Carlson and Johnson (1991) be used to determine the overall reaction stoichiometry.

5.3 Open-system diffusion modelling

Open-system diffusion models for SK8C, SK12A, SK9A, SK9B and SK9C are presented in Tables 5.5-5.9. The overall reaction for each corona was calculated using measured phase ratios from image analysis in MATLAB and the average phase compositions in each layer based on the constant-volume approximation (Carlson and Johnson, 1991, Chapter 3) with the original reactant interface at the contact between the blocky orthopyroxene and the immediately contiguous feldspar-bearing layer. Open-system behaviour was accommodated through the introduction of 'imaginary' or artificial phases Met_1 and Met_2 (Ashworth and Birdi, 1990; Ashworth and Sheplev, 1997; Ashworth et al., 1998), which represent the metasomatic fluxes of components in and out of the system. Met_1 is located at the garnet boundary of the corona and Met_2 is located at the quartz boundary. The stoichiometry of these imaginary phases represents the ratios in which components are either lost or gained by the system. Components modelled include SiO_2, $AlO_{3/2}$, FeO, $FeO_{3/2}$, MgO, MnO, CaO, $NaO_{1/2}$ and $KO_{1/2}$. They are abbreviated as Si, Al, Fe^{2+}, Fe^{3+}, Mg, Mn, Ca, Na and K. The component H_2O is not considered in

modelling. This component is considered perfectly mobile, in agreement with Ashworth and Sheplev (1997).

Models presented are those where the ratio of predicted model layer widths most closely approaches the measured layer widths for a set of phenomenological coefficients for diffusion (L-ratios), which satisfy the stability criterion (Ashworth et and Sheplev, 1997; Appendix A). The MATLAB code used in iterative solution of simultaneous equations governing component flux, chemical potential gradients and reaction coefficients between layers is included in Appendix A. Optimally stable models reported are those in which the relative differences in phenomenological coefficients for all components, required to generate diffusionally stable solutions, is minimized. Reaction coefficients for each phase in reactions at layer boundaries are also included in Tables 5.5-5.9. A negative reaction coefficient indicates growth of the phase and a positive reaction coefficient indicates consumption of that phase. The component fluxes and chemical potential gradients for each component are reported and used to determine model gradients in Gibbs free energy for phases across each layer. The overall reaction affinity for each corona is computed from individual component fluxes and chemical potential gradients. The deviation of a model reaction affinity from zero is a measure of the extent of equilibration, i.e., larger magnitudes of reaction affinity indicate greater scales of disequilibrium. Non-equilibrium thermobarometry based on end-member reaction affinities across the coronas has been undertaken to constrain prevailing *P*-*T* conditions during corona growth.

Table 5.5: Modelling results for corona SK8C

N matrix (n_{ik} phase compositions, 24-oxygen mole basis)

i	***Grt***	***Crd***	***Opx$_{S1}$***	***Pl***	***Opx$_b$***	***Qtz***	***Met$_1$***	***Met$_2$***
Si	6.002	6.667	7.274	8.400	7.882	12.000	0.000	-34.660
Al	4.088	5.333	1.504	3.375	0.271	0.000	-0.882	0.000
Fe^{3+}	0.000	0.000	0.024	0.234	0.013	0.000	0.000	0.063
Fe^{2+}	4.054	0.644	3.089	0.000	3.659	0.000	0.000	2.273
Mn	0.128	0.000	0.022	0.000	0.030	0.000	-0.080	0.000
Mg	1.538	2.027	3.880	0.000	4.105	0.000	0.000	6.140
Ca	0.142	0.000	0.078	0.663	0.017	0.000	0.013	0.000
Na	0.000	0.000	0.000	2.190	0.000	0.000	0.344	0.000
K	0.000	0.000	0.000	0.051	0.000	0.000	0.008	0.000

Measured Proportion of product phases (counts)

Crd	***Opx$_{S1}$***	***Pl***	***Opx$_b$***
0.3791	0.1104	0.0758	0.4347

Overall Reaction

1 ***Grt*** + 3.80 ***Qtz*** + 0.06 $FeO_{3/2}$ + 2.27 FeO + 6.14 MgO + 0.01 CaO + 0.34 $NaO_{1/2}$ + 0.01 $KO_{1/2}$ = 34.66 SiO_2 + 0.88 $AlO_{3/2}$ + 0.08 MnO + 0.33 ***Crd*** + 0.35 ***Opx$_{S1}$*** + 0.16 ***Plg*** + 1.37 ***Opx$_b$***

L-ratios (phenomenological coefficients)

L_{SiSi}/L_{AlAl}	5.8	L_{SiSi}/L_{MgMg}	0.52
$L_{SiSi}/L_{Fe^{3+}Fe^{3+}}$	1	L_{SiSi}/L_{CaCa}	0.6
$L_{SiSi}/L_{Fe^{2+}Fe^{2+}}$	0.45	L_{SiSi}/L_{NaNa}	0.6
L_{SiSi}/L_{MnMn}	1	L_{SiSi}/L_{KK}	1

Coefficients of phases at boundaries 1-, V_k^r at boundary q (mol phase/mol reaction progress)

Boundary	***Crd***	***Opx$_{S1}$***	***Pl***	***Opx$_b$***
1	-0.4672	-0.4305		
2	0.1340	0.0782	-0.2026	
3			0.0462	-0.0424
4				-1.3305

Table 5.5 continued: Modelling Results for corona SK8C

Molar amounts of minerals in layer r (mol/mol reaction progress)

Layer	*Crd*	Opx_{S1}	*Pl*	Opx_b
1	0.3332	0.3523		
2			0.1564	
3				1.3729

Molar volumes of phases ($10^{-4}m^3mol^{-1}$)

Crd	Opx_{S1}	*Pl*	Opx_b
2.3457	0.6465	0.9993	0.6529

Model layer thicknesses, hr* ($10^{-4}m^3$/mol reaction progress)

Thickness	*Layer 1*	*Layer 2*	*Layer 3*
hr*	1.01	0.16	0.90
ratio	1.13	0.17	1.00

Observed layer widths (μm)

Width	*Layer 1*	*Layer 2*	*Layer 3*
measured	63	11	58
ratio	1.09	0.19	1.00

Model fluxes in layers 1 to 3 (mol/mol reaction progress)

Layer	*Si*	*Al*	Fe^{3+}	Fe^{2+}	*Mn*	*Mg*	*Ca*	*Na*	*K*
1	-0.2446	0.0668	-0.0103	2.4232	0.0385	-1.0795	0.1214	0.3420	0.0080
2	-0.4841	0.2154	-0.0559	2.7512	0.0402	-0.5043	-0.0068	-0.1017	-0.0023
3	-0.4304	0.3598	-0.0456	2.5959	0.0390	-0.6786	0.0231	-0.0005	0.0000

Matrix: Jqt

Model chemical potential gradients for components in layers 1 to 3 (mol/mol reaction progress)

Layer	*Si*	*Al*	Fe^{3+}	Fe^{2+}	*Mn*	*Mg*	*Ca*	*Na*	*K*
1	0.2446	-0.3875	0.0103	-1.0904	-0.0385	0.5614	-0.0729	-0.2052	-0.0080
2	0.4841	-1.2491	0.0559	-1.2380	-0.0402	0.2623	0.0041	0.0610	0.0023
3	0.4304	-2.0870	0.0456	-1.1681	-0.0390	0.3529	-0.0139	0.0003	0.0000

Matrix: Cpt

Table 5.5 continued: Modelling Results for corona SK8C

Model Free Energy gradients for phases in layers 1 to 3 (mol^2 component/[(mol mineral).(mol reaction progress)])

Layer	*Grt*	*Crd*	*Opx_{S1}*	*Pl*	*Opx_b*	*Qtz*	*Met_1*	*Met_2*
1	-3.6884	0.0000	0.0000	0.2514	0.1353	2.9355	0.2737	-7.5096
2	-6.8211	-3.6998	-1.1636	0.0000	0.0230	5.8086	1.1258	-17.9770
3	-10.1490	-8.2979	-2.2486	-3.4265	0.0000	5.1645	1.8438	-15.4020

Matrix: Gfkgrd

Model Free Energy differences for phases across layers 1 to 3 (m^{3}mol^2 component/[(mol mineral).(mol^2 reaction progress)])

Layer	*Grt*	*Crd*	*Opx_{S1}*	*Pl*	*Opx_b*	*Qtz*	*Met_1*	*Met_2*
1	-3.7230E-04	0.0000	0.0000	2.5374E-05	1.3657E-05	2.9630E-04	2.7623E-05	-7.5800E-04
2	-1.0660E-04	-5.7819E-05	-1.8184E-05	0.0000	3.5887E-07	9.0773E-05	1.7594E-05	-2.8093E-04
3	-9.0970E-04	-7.4381E-04	-2.0156E-04	-3.0714E-04	0.0000	4.6293E-04	1.6527E-04	-1.3806E-03

Matrix: Gfkdiff

Model Free Energy differences of phases at boundary q from those at boundary where phase is present (must be ≤0 for stability)

Boundary	*Grt*	*Crd*	*Opx_{S1}*	*Pl*	*Opx_b*	*Qtz*
1	0.0000	0.0000	0.0000	-2.5374E-05	-1.4015E-05	-8.5001E-04
2	-3.7230E-04	0.0000	0.0000	0.0000	-3.5800E-07	-5.5371E-04
3	-4.7889E-04	-5.7819E-05	-1.8184E-05	0.0000	0.0000	-4.6293E-04
4	-1.3886E-03	-8.0163E-04	-2.1974E-04	-3.0714E-04	0.0000	0.0000

For calculation of model affinity -ΔG (m^{3}mol^2 component/mol^3 reaction progress)

Layer	*Si*	*Al*	*Fe^{3+}*	*Fe^{2+}*	*Mn*	*Mg*	*Ca*	*Na*	*K*	*Total*
1	6.0405E-06	2.6132E-06	1.0777E-08	2.6670E-04	1.4983E-07	6.1166E-05	8.9285E-07	7.0836E-06	6.4600E-09	3.4467E-04
2	3.6616E-06	4.2039E-06	4.8775E-08	5.3227E-05	2.5316E-08	2.0669E-06	4.3534E-10	9.7037E-08	8.5088E-11	6.3331E-05
3	1.6603E-05	6.7315E-05	1.8643E-07	2.7181E-04	1.3617E-07	2.1462E-05	2.8715E-08	1.4320E-11	4.9925E-14	3.7754E-04

Reaction Affinity (m^{3}mol^{-1}) 0.0007855

Table 5.6: Modelling Results for corona SK12A

N matrix (n_{ik} phase compositions, 24-oxygen mole basis)

i	***Grt***	***Crd***	***Opx$_{S1}$***	***Pl***	***Opx$_b$***	***Qtz***	***Met$_1$***	***Met$_2$***
Si	5.962	6.667	7.360	7.799	7.685	12.000	0.000	-35.951
Al	4.085	5.333	1.078	4.010	0.227	0.000	-1.118	0.000
Fe^{3+}	0.016	0.000	0.262	0.157	0.402	0.000	0.000	0.679
Fe^{2+}	4.290	0.880	3.818	0.000	4.099	0.000	0.000	3.432
Mn	0.089	0.000	0.000	0.000	0.000	0.000	-0.089	0.000
Mg	1.367	1.787	3.439	0.000	3.561	0.000	0.000	5.733
Ca	0.182	0.000	0.014	1.222	0.026	0.000	-0.014	0.000
Na	0.000	0.000	0.000	1.833	0.000	0.000	0.188	0.000
K	0.000	0.000	0.000	0.028	0.000	0.000	0.003	0.000

Measured Proportion of product phases (counts)

Crd	***Opx$_{S1}$***	***Pl***	***Opx$_b$***
0.3726	0.1358	0.0495	0.4421

Overall Reaction

1 ***Grt*** + 3.92 ***Qtz*** +0.68 $FeO_{3/2}$ +3.43 FeO +5.73 MgO + 0.19 $NaO_{1/2}$ + 0.003 $KO_{1/2}$= 35.95 SiO_2 + 1.12 $AlO_{3/2}$ + 0.09 MnO + 0.01 CaO + 0.33 ***Crd*** + 0.43 ***Opx$_{S1}$*** + 0.10 ***Pl*** + 1.41 ***Opx$_b$***

L-ratios (phenomenological coefficients)

L_{SiSi}/L_{AlAl}	3.5	L_{SiSi}/L_{MgMg}	0.45
$L_{SiSi}/L_{Fe^{3+}Fe^{3+}}$	1	L_{SiSi}/L_{CaCa}	0.55
$L_{SiSi}/L_{Fe^{2+}Fe^{2+}}$	0.42	L_{SiSi}/L_{NaNa}	0.55
L_{SiSi}/L_{MnMn}	1	L_{SiSi}/L_{KK}	1

Coefficients of phases at boundaries 1-4, V_k^r at boundary q (mol phase/mol reaction progress)

Boundary	***Crd***	***Opx$_{S1}$***	***Pl***	***Opx$_b$***
1	-0.4435	-0.4521		
2	0.1118	0.0185	-0.1244	
3			0.0220	-0.0175
4				-1.3912

Table 5.6 continued: Modelling Results for corona SK12A

Molar amounts of minerals in layer r (mol/mol reaction progress)

Layer	*Crd*	Opx_{S1}	*Pl*	Opx_b
1	0.3317	0.4336		
2			0.1023	
3				1.4087

Molar volumes of phases ($10^{-4}m^3mol^{-1}$)

Crd	Opx_{S1}	*Pl*	Opx_b
2.3492	0.6549	1.0109	0.6564

Model layer thicknesses, hr* ($10^{-4}m^3$/mol reaction progress)

Thickness	*Layer 1*	*Layer 2*	*Layer 3*
hr*	1.06	0.10	0.92
ratio	1.15	0.11	1.00

Observed layer widths (μm)

Width	*Layer 1*	*Layer 2*	*Layer 3*
measured	120	12	105
ratio	1.14	0.11	1.00

Model fluxes in layers 1 to 3 (mol/mol reaction progress)

Layer	*Si*	*Al*	Fe^{3+}	Fe^{2+}	*Mn*	*Mg*	*Ca*	*Na*	*K*
1	-0.3226	0.1144	-0.1025	2.1734	0.0000	-0.9805	0.1617	0.1880	0.0030
2	-0.4107	0.2319	-0.1171	2.3426	0.0000	-0.7169	0.0100	-0.0400	-0.0005
3	-0.3728	0.3164	-0.1207	2.2710	0.0000	-0.7791	0.0365	0.0005	0.0001

Matrix: Jqt

Model chemical potential gradients for components in layers 1 to 3 (mol/mol reaction progress)

Layer	*Si*	*Al*	Fe^{3+}	Fe^{2+}	*Mn*	*Mg*	*Ca*	*Na*	*K*
1	0.3226	-0.4005	0.1025	-0.9129	0.0000	0.4412	-0.0889	-0.1034	-0.0030
2	0.4107	-0.8117	0.1171	-0.9839	0.0000	0.3226	-0.0055	0.0220	0.0005
3	0.3728	-1.1075	0.1207	-0.9538	0.0000	0.3506	-0.0201	-0.0003	-0.0001

Matrix: Cpt

Table 5.6 continued: Modelling Results for corona SK12A

Model Free Energy gradients for phases in layers 1 to 3 (mol^2 component/[(mol mineral).(mol reaction progress)])

Layer	*Grt*	*Crd*	*Opx_{S1}*	*Pl*	*Opx_b*	*Qtz*	*Met_1*	*Met_2*
1	-3.0403	0.0000	0.0000	0.6276	0.2562	3.8707	0.4295	-12.1300
2	-4.6463	-1.8801	-0.4689	0.0000	0.1345	4.9281	0.9117	-16.2120
3	-5.9162	-3.6340	-0.8551	-1.5400	0.0000	4.4733	1.2384	-14.5830

Matrix: Gfkgrd

Model Free Energy differences for phases across layers 1 to 3 (m^{3}mol^2 component/[(mol mineral).(mol^2 reaction progress)])

Layer	*Grt*	*Crd*	*Opx_{S1}*	*Pl*	*Opx_b*	*Qtz*	*Met_1*	*Met_2*
1	-3.2324E-04	0.0000	0.0000	6.6730E-05	2.7241E-05	4.1154E-04	4.5665E-05	-1.2897E-03
2	-4.8043E-05	-1.9440E-05	-4.8484E-06	0.0000	1.3911E-06	5.0957E-05	9.4268E-06	-1.6763E-04
3	-5.4707E-04	-3.3604E-04	-7.9067E-05	-1.4240E-04	0.0000	4.1364E-04	1.1452E-04	-1.3485E-03

Matrix: Gfkdiff

Model Free Energy differences of phases at boundary q from those at boundary where phase is present (must be ≤0 for stability)

Boundary	*Grt*	*Crd*	*Opx_{S1}*	*Pl*	*Opx_b*	*Qtz*
1	0.0000	0.0000	0.0000	-6.6730E-05	-2.8632E-05	-8.7614E-04
2	-3.2324E-04	0.0000	0.0000	0.0000	-1.3910E-06	-4.6460E-04
3	-3.7129E-04	-1.9440E-05	-4.8484E-06	0.0000	0.0000	-4.1365E-04
4	-9.1836E-04	-3.5548E-04	-8.3915E-05	-1.4240E-04	0.0000	0.0000

For calculation of model affinity -ΔG (m^{3}mol^2 component/mol^3 reaction progress)

Layer	*Si*	*Al*	*Fe^{3+}*	*Fe^{2+}*	*Mn*	*Mg*	*Ca*	*Na*	*K*	*Total*
1	1.1025E-05	4.8555E-06	1.1125E-06	2.1024E-04	0.0000E+00	4.5839E-05	1.5233E-06	2.0599E-06	9.5371E-10	2.7665E-04
2	1.7388E-06	1.9407E-06	1.4144E-07	2.3762E-05	0.0000E+00	2.3843E-06	5.6173E-10	9.0566E-09	2.3978E-12	2.9977E-05
3	1.2806E-05	3.2298E-05	1.3422E-06	1.9963E-04	0.0000E+00	2.5172E-05	6.7400E-08	1.1879E-11	1.6946E-12	2.7132E-04

Reaction Affinity (m^{3}mol^{-1}) **0.0005780**

Table 5.7: Modelling Results for corona SK9A

N matrix (n_{ik} phase compositions, 24-oxygen mole basis)

i	*Grt*	*Crd*	Opx_{S1}	*Pl*	Opx_b	*Qtz*	Met_1	Met_2
Si	5.945	6.667	7.474	7.987	7.603	12.000	0.000	-53.135
Al	4.090	5.333	0.749	3.799	0.336	0.000	-0.805	0.000
Fe^{3+}	0.033	0.000	0.303	0.163	0.459	0.000	0.000	1.009
Fe^{2+}	4.675	1.080	4.470	0.000	4.514	0.000	0.000	6.218
Mn	0.201	0.000	0.000	0.000	0.000	0.000	-0.201	0.000
Mg	0.883	1.587	2.987	0.000	3.068	0.000	0.000	6.818
Ca	0.168	0.000	0.017	1.050	0.021	0.000	0.000	0.000
Na	0.000	0.000	0.000	2.029	0.000	0.000	0.233	0.000
K	0.000	0.000	0.000	0.035	0.000	0.000	0.004	0.000

Measured Proportion of product phases (counts)

Crd	Opx_{S1}	*Pl*	Opx_b
0.3421	0.0770	0.0464	0.5344

Overall Reaction

1 ***Grt*** + 5.68 ***Qtz*** + 1.01 $FeO_{3/2}$ + 6.22 FeO + 6.82 MgO + 0.23 $NaO_{1/2}$ + 0.004 $KO_{1/2}$= 53.14 SiO_2 + 0.81 $AlO_{3/2}$ + 0.20 MnO + 0.37 ***Crd*** + 0.29 Opx_{S1}+ 0.11 ***Pl*** + 2.04 Opx_b

L-ratios (phenomenological coefficients)

L_{SiSi}/L_{AlAl}	1	L_{SiSi}/L_{MgMg}	0.12
$L_{SiSi}/L_{Fe^{3+}Fe^{3+}}$	1	L_{SiSi}/L_{CaCa}	0.4
$L_{SiSi}/L_{Fe^{2+}Fe^{2+}}$	0.1	L_{SiSi}/L_{NaNa}	0.4
L_{SiSi}/L_{MnMn}	1	L_{SiSi}/L_{KK}	1

Coefficients of phases at boundaries 1-4, V_k^r at boundary q (mol phase/mol reaction progress)

Boundary	*Crd*	Opx_{S1}	*Pl*	Opx_b
1	-0.5451	-0.3255		
2	0.1800	0.0332	-0.1878	
3			0.0737	-0.0732
4				-1.9635

Table 5.7 continued: Modelling Results for corona SK9A

Molar amounts of minerals in layer r (mol/mol reaction progress)

Layer	*Crd*	Opx_{S1}	*Pl*	Opx_b
1	0.3651	0.2923		
2			0.1141	
3				2.0367

Molar volumes of phases ($10^{-4}m^3mol^{-1}$)

Crd	Opx_{S1}	*Pl*	Opx_b
2.3521	0.6614	1.0206	0.6586

Model layer thicknesses, hr* ($10^{-4}m^3$/mol reaction progress)

Thickness	*Layer 1*	*Layer 2*	*Layer 3*
hr*	1.05	0.12	1.34
ratio	0.78	0.09	1.00

Observed layer widths (μm)

Width	*Layer 1*	*Layer 2*	*Layer 3*
measured	40	5	50
ratio	0.80	0.10	1.00

Model fluxes in layers 1 to 3 (mol/mol reaction progress)

Layer	*Si*	*Al*	Fe^{3+}	Fe^{2+}	*Mn*	*Mg*	*Ca*	*Na*	*K*
1	-0.1225	0.1339	-0.0656	2.6311	0.0000	-0.9545	0.1615	0.2320	0.0040
2	-0.1741	0.4054	-0.0862	2.9741	0.0000	-0.5695	-0.0352	-0.1491	-0.0026
3	-0.1413	0.6609	-0.1077	2.6439	0.0000	-0.7940	0.0407	0.0005	0.0000

Matrix: Jqt

Model chemical potential gradients for components in layers 1 to 3 (mol/mol reaction progress)

Layer	*Si*	*Al*	Fe^{3+}	Fe^{2+}	*Mn*	*Mg*	*Ca*	*Na*	*K*
1	0.1225	-0.1339	0.0656	-0.2631	0.0000	0.1145	-0.0646	-0.0928	-0.0040
2	0.1741	-0.4054	0.0862	-0.2974	0.0000	0.0683	0.0141	0.0597	0.0026
3	0.1413	-0.6609	0.1077	-0.2644	0.0000	0.0953	-0.0163	-0.0002	0.0000

Matrix: Cpt

Table 5.7 continued: Modelling Results for corona SK9A

Model Free Energy gradients for phases in layers 1 to 4 (mol^2 component/[(mol mineral).(mol reaction progress)])

Layer	*Grt*	*Crd*	*Opx_{S1}*	*Pl*	*Opx_b*	*Qtz*	*Met_1*	*Met_2*
1	-0.9572	0.0000	0.0000	0.2240	0.0788	1.4699	0.0863	-7.2975
2	-1.9482	-1.2143	-0.1018	0.0000	0.0941	2.0886	0.3402	-10.5440
3	-3.0144	-2.7173	-0.3040	-1.3825	0.0000	1.6953	0.5320	-8.3924

Matrix: Gfkgrd

Model Free Energy differences for phases across layers 1 to 3 (m^3mol^2 component/[(mol mineral).(mol^2 reaction progress)])

Layer	*Grt*	*Crd*	*Opx_{S1}*	*Pl*	*Opx_b*	*Qtz*	*Met_1*	*Met_2*
1	-1.0070E-04	0.0000	0.0000	2.3564E-05	8.2900E-06	1.5464E-04	9.0830E-06	-7.6774E-04
2	-2.2684E-05	-1.4139E-05	-1.1847E-06	0.0000	1.0954E-06	2.4319E-05	3.9609E-06	-1.2278E-04
3	-4.0436E-04	-3.6449E-04	-4.0781E-05	-1.8544E-04	0.0000	2.2741E-04	7.1366E-05	-1.1258E-03

Matrix: Gfkdiff

Model Free Energy differences of phases at boundary q from those at boundary where phase is present (must be ≤0 for stability)

Boundary	*Grt*	*Crd*	*Opx_{S1}*	*Pl*	*Opx_b*	*Qtz*
1	0.0000	0.0000	0.0000	-2.3564E-05	-9.3854E-06	-4.0637E-04
2	-1.0070E-04	0.0000	0.0000	0.0000	-1.0954E-06	-2.5173E-04
3	-1.2338E-04	-1.4139E-05	-1.1847E-06	0.0000	0.0000	-2.2741E-04
4	-5.2774E-04	-3.7863E-04	-4.1966E-05	-1.8544E-04	0.0000	0.0000

For calculation of model affinity -ΔG (m^3mol^2 component/mol^3 reaction progress)

Layer	*Si*	*Al*	*Fe^{3+}*	*Fe^{2+}*	*Mn*	*Mg*	*Ca*	*Na*	*K*	*Total*
1	1.5785E-06	1.8871E-06	4.5324E-07	7.2831E-05	0.0000E+00	1.1502E-05	1.0972E-06	2.2650E-06	1.6833E-09	9.1616E-05
2	3.5273E-07	1.9136E-06	8.6489E-08	1.0299E-05	0.0000E+00	4.5320E-07	5.7710E-09	1.0358E-07	7.7170E-11	1.3215E-05
3	2.6774E-06	5.8598E-05	1.5571E-06	9.3766E-05	0.0000E+00	1.0147E-05	8.8837E-08	1.2941E-11	5.6674E-15	1.6683E-04

Reaction Affinity (m^3mol^{-1}) 0.0002717

Table 5.8: Modelling Results for corona SK9B

N matrix (n_{ik} phase compositions, 24-oxygen mole basis)

i	*Grt*	*Crd*	Opx_{S1}	*Pl*	Opx_{S2}	*Ksp*	Opx_b	*Qtz*	Met_1	Met_2
Si	5.920	6.667	7.437	7.900	7.490	9.123	7.729	12.00	0.000	-62.402
Al	4.102	5.333	0.898	4.037	0.622	2.786	0.188	0.00	-0.534	0.000
Fe3+	0.058	0.000	0.245	0.069	0.401	0.049	0.380	0.00	0.000	0.912
Fe2+	4.700	1.067	4.301	0.000	4.404	0.000	4.617	0.00	0.000	6.972
Mn	0.220	0.000	0.000	0.000	0.000	0.000	0.000	0.00	-0.220	0.000
Mg	0.814	1.600	3.093	0.000	2.925	0.000	3.052	0.00	1.000	6.130
Ca	0.186	0.000	0.015	1.101	0.156	0.004	0.021	0.00	0.221	0.000
Na	0.000	0.000	0.000	1.863	0.000	0.647	0.000	0.00	0.694	0.000
K	0.000	0.000	0.000	0.007	0.000	2.352	0.000	0.00	0.383	0.000

Measured Proportion of product phases (counts)

Crd	Opx_{S1}	*Pl*	Opx_{S2}	*Ksp*	Opx_b
0.2161	0.0161	0.1163	0.0108	0.0632	0.5775

Overall Reaction

1 ***Grt*** + 6.77 ***Qtz*** + 0.91 $FeO_{3/2}$ + 6.97 FeO + 6.13 MgO + 0.22 CaO + 0.69 $NaO_{1/2}$ + 0.38 $KO_{1/2}$= 62.40 SiO_2 + 0.53 $AlO_{3/2}$ + 0.22 MnO + 0.25 ***Crd*** + 0.001 Opx_{S1} + 0.32 ***Pl*** + 0.05 Opx_{S2} + 0.16 ***Ksp*** + 2.43 Opx_b

L-ratios (phenomenological coefficients)

L_{SiSi}/L_{AlAl}	1.5	L_{SiSi}/L_{MgMg}	0.08
$L_{SiSi}/L_{Fe^{3+}Fe^{3+}}$	1	L_{SiSi}/L_{CaCa}	0.20
$L_{SiSi}/L_{Fe^{2+}Fe^{2+}}$	0.05	L_{SiSi}/L_{NaNa}	0.20
L_{SiSi}/L_{MnMn}	1	L_{SiSi}/L_{KK}	0.15

Coefficients of phases at boundaries 1-4, V_k^r at boundary q (mol phase/mol reaction progress)

Boundary	*Crd*	Opx_{S1}	*Pl*	Opx_{S2}	*Ksp*	Opx_b
1	-0.6140	-0.2586				
2	0.3598	0.2573	-0.4698	-0.0918		
3			0.1536	0.0467	-0.1724	
4					0.0106	-0.0108
5						-2.4143

Table 5.8 continued: Modelling Results for corona SK9B

Molar amounts of minerals in layer r (mol/mol reaction progress)

Layer	*Crd*	*Opx$_{S1}$*	*Pl*	*Opx$_{S2}$*	*Ksp*	*Opx$_b$*
1	0.2543	0.0013				
2			0.3162	0.0451		
3					0.1618	
4						2.4251

Molar volumes of phases (10^{-4}m^{3}mol^{-1})

Crd	*Opx$_{S1}$*	*Pl*	*Opx$_{S2}$*	*Ksp*	*Opx$_b$*
2.3519	0.6596	1.0178	0.6619	1.0807	0.6589

Model layer thicknesses, hr* (10^{-4}m^3/mol reaction progress)

Thickness	*Layer 1*	*Layer 2*	*Layer 3*	*Layer 4*
hr*	0.60	0.35	0.17	1.60
ratio	0.37	0.22	0.11	1.00

Observed layer widths (μm)

Width	*Layer 1*	*Layer 2*	*Layer 3*	*Layer 4*
measured	40	20	15	100
ratio	0.40	0.20	0.15	1.00

Model fluxes in layers 1 to 4 (mol/mol reaction progress)

Layer	*Si*	*Al*	*Fe^{3+}*	*Fe^{2+}*	*Mn*	*Mg*	*Ca*	*Na*	*K*
1	-0.0968	0.0606	-0.0054	2.9327	0.0000	0.0318	0.4027	0.6937	0.3829
2	-0.1844	0.2563	-0.0116	4.0188	0.0000	1.1346	-0.1250	-0.1817	0.3796
3	-0.1938	0.4253	0.0093	4.2245	0.0000	1.2712	0.0507	-0.0070	-0.0249
4	-0.1806	0.4528	0.0057	4.1745	0.0000	1.2381	0.0506	-0.0001	0.0001

Matrix: Jqt

Model chemical potential gradients for components in layers 1 to 4 (mol/mol reaction progress)

Layer	*Si*	*Al*	*Fe^{3+}*	*Fe^{2+}*	*Mn*	*Mg*	*Ca*	*Na*	*K*
1	0.0968	-0.0909	0.0054	-0.1466	0.0000	-0.0025	-0.0805	-0.1387	-0.0574
2	0.1844	-0.3845	0.0116	-0.2009	0.0000	-0.0908	0.0250	0.0363	-0.0569
3	0.1938	-0.6379	-0.0093	-0.2112	0.0000	-0.1017	-0.0101	0.0014	0.0037
4	0.1806	-0.6792	-0.0057	-0.2087	0.0000	-0.0991	-0.0101	0.0000	0.0000

Matrix: Cpt

Table 5.8 continued: Modelling Results for corona SK9B

Model Free Energy gradients for phases in layers 1 to 4 (mol^2 component/[(mol mineral).(mol reaction progress)])

Layer	*Grt*	*Crd*	*Opx_{S1}*	*Pl*	*Opx_{S2}*	*Ksp*	*Opx_b*	*Qtz*	*Met_1*	*Met_2*
1	-0.5058	0.0000	0.0000	0.0506	0.0050	0.4051	0.0469	1.1619	-0.0899	-7.0753
2	-1.4987	-1.1809	-0.1158	0.0000	0.0000	0.5012	0.1530	2.2126	0.1237	-13.4530
3	-2.5474	-2.4980	-0.3570	-1.0534	-0.1782	0.0000	0.0886	2.3256	0.2394	-14.1980
4	-2.7807	-2.7992	-0.4723	-1.3265	-0.2824	-0.2448	0.0000	2.1675	0.2618	-13.3390

Model Free Energy differences for phases across layers 1 to 4 (m^{3}mol^2 component/[(mol mineral).(mol^2 reaction progress)])

Layer	*Grt*	*Crd*	*Opx_{S1}*	*Pl*	*Opx_{S2}*	*Ksp*	*Opx_b*	*Qtz*	*Met_1*	*Met_2*
1	-3.0290E-05	0.0000	0.0000	3.0308E-06	3.0149E-07	2.4260E-05	2.8059E-06	6.9586E-05	-5.3852E-06	-4.2373E-04
2	-5.2706E-05	-4.1531E-05	-4.0717E-06	0.0000	0.0000	1.7626E-05	5.3809E-06	7.7816E-05	4.3491E-06	-4.7313E-04
3	-4.4546E-05	-4.3683E-05	-6.2429E-06	-1.8421E-05	-3.1166E-06	0.0000	1.5495E-06	4.0668E-05	4.1866E-06	-2.4828E-04
4	-4.0702E-04	-3.9913E-04	-5.7043E-05	-1.6832E-04	-2.8477E-05	0.0000	1.4158E-05	3.7159E-04	3.8254E-05	-2.2686E-03

Model Free Energy differences of phases at boundary q from those at boundary where phase is present (must be ≤0 for stability)

Boundary	*Grt*	*Crd*	*Opx_{S1}*	*Pl*	*Opx_{S2}*	*Ksp*	*Opx_b*	*Qtz*
1	0.0000	0.0000	0.0000	-3.0308E-06	-3.0149E-07	-4.1886E-05	-2.3894E-05	-5.5966E-04
2	-3.0290E-05	0.0000	0.0000	0.0000	0.0000	-1.7626E-05	-6.9303E-06	-4.9007E-04
3	-8.2996E-05	-4.1531E-05	0.0000	0.0000	0.0000	0.0000	-1.5494E-06	-4.1226E-04
4	-1.2754E-04	-8.5214E-05	-1.0315E-05	-1.8421E-05	-3.1167E-06	0.0000	0.0000	-3.7159E-04
5	-5.3457E-04	-4.8435E-04	-6.7357E-05	-1.8674E-04	-3.1593E-05	0.0000	0.0000	0.0000

For calculation of model affinity -ΔG (m^{3}mol^2 component/mol^3 reaction progress)

Layer	*Si*	*Al*	*Fe^{3+}*	*Fe^{2+}*	*Mn*	*Mg*	*Ca*	*Na*	*K*	*Total*
1	5.6148E-07	3.3024E-07	1.7143E-09	2.5753E-05	0.0000E+00	4.8347E-09	1.9428E-06	5.7631E-06	1.3167E-06	3.5674E-05
2	1.1957E-06	3.4664E-06	4.6916E-09	2.8400E-05	0.0000E+00	3.6218E-06	1.0992E-07	2.3209E-07	7.6000E-07	3.7791E-05
3	6.5679E-07	4.7440E-06	1.5223E-09	1.5604E-05	0.0000E+00	2.2605E-06	9.0041E-09	1.7003E-10	1.6239E-09	2.3277E-05
4	5.2132E-06	4.9142E-05	5.2593E-09	1.3922E-04	0.0000E+00	1.9595E-05	8.1673E-08	3.5366E-13	1.6511E-13	2.1326E-04

Reaction Affinity (m^{3}mol^{-1}) 0.0003100

Table 5.9: Modelling Results for corona SK9C

N matrix (n_{ik} phase compositions, 24-oxygen mole basis)

i	*Grt*	*Crd*	Opx_{S1}	*Pl*	Opx_{S2}	Opx_b	*Qtz*	Met_1	Met_2
Si	5.922	6.670	7.593	8.002	7.650	7.75	12.00	0.000	-12.981
Al	3.845	5.268	0.624	3.951	0.545	0.38	0.00	-1.411	0.000
Fe3+	0.302	0.058	0.152	0.069	0.135	0.13	0.00	0.000	-0.204
Fe2+	4.326	1.051	4.548	0.000	4.589	4.56	0.00	0.000	-1.478
Mn	0.368	0.028	0.120	0.000	0.126	0.13	0.00	-0.29	0.000
Mg	1.047	1.592	2.913	0.000	2.922	3.03	0.00	0.000	1.151
Ca	0.182	0.000	0.008	1.027	0.014	0.02	0.00	-0.087	0.000
Na	0.000	0.000	0.000	1.847	0.000	0.00	0.00	0.154	0.000
K	0.000	0.000	0.000	0.031	0.000	0.00	0.00	0.003	0.000

Measured Proportion of product phases (counts)

Crd	Opx_{S1}	*Pl*	Opx_{S2}	Opx_b
0.5720	0.1457	0.0586	0.0300	0.1938

Overall Reaction

1 ***Grt*** + 1.19 ***Qtz*** + 1.15 MgO + 0.15 $NaO_{1/2}$ + 0.003 $KO_{1/2}$ = 12.98 SiO_2 + 1.41 $AlO_{3/2}$ + 0.20 $FeO_{3/2}$ + 1.48 FeO + 0.29 MnO + 0.09 CaO + 0.36 ***Crd*** + 0.05 Opx_{S1} + 0.08 ***Pl*** + 0.07 Opx_{S2} + 0.43Opx_b

L-ratios (phenomenological coefficients)

L_{SiSi}/L_{AlAl}	1	L_{SiSi}/L_{MgMg}	0.027
$L_{SiSi}/L_{Fe^{3+}Fe^{3+}}$	1	L_{SiSi}/L_{CaCa}	0.205
$L_{SiSi}/L_{Fe^{2+}Fe^{2+}}$	0.024	L_{SiSi}/L_{NaNa}	0.205
L_{SiSi}/L_{MnMn}	1	L_{SiSi}/L_{KK}	1

Coefficients of phases at boundaries 1-4, V_i^r at boundary q (mol phase/mol reaction progress)

Boundary	*Crd*	Opx_{S1}	*Pl*	Opx_{S2}	Opx_b
1	-0.4060	-0.4268			
2	0.0496	0.3772	-0.0705	-0.3447	
3			-0.0127	0.2787	-0.2621
4					-0.1644

Table 5.9 continued: Modelling Results for corona SK9C

Molar amounts of minerals in layer r (mol/mol reaction progress)

Layer	*Crd*	Opx_{S1}	*Pl*	Opx_{S2}	Opx_b
1	0.3564	0.0495			
2			0.0832	0.0659	
3					0.4265

Molar volumes of phases ($10^{-4}m^3mol^{-1}$)

Crd	Opx_{S1}	*Pl*	Opx_{S2}	Opx_b
2.3271	0.6592	1.0204	0.6592	0.6588

Model layer thicknesses, hr* ($10^{-4}m^3$/mol reaction progress)

Thickness	*Layer 1*	*Layer 2*	*Layer 3*
hr*	0.86	0.13	0.28
ratio	3.07	0.46	1.00

Observed layer widths (μm)

Width	*Layer 1*	*Layer 2*	*Layer 3*
measured	125	19	40
ratio	3.13	0.48	1.00

Model fluxes in layers 1 to 3 (mol/mol reaction progress)

Layer	*Si*	*Al*	Fe^{3+}	Fe^{2+}	*Mn*	*Mg*	*Ca*	*Na*	*K*
1	-0.0263	0.0284	0.2131	1.9583	0.0183	-0.8432	0.0919	0.1537	0.0026
2	-0.0324	0.0585	0.2219	2.1445	0.0217	-0.6722	0.0177	0.0234	0.0004
3	-0.0317	0.0618	0.2248	2.2281	0.0219	-0.6524	0.0033	0.0000	0.0000

Matrix: Jqt

Model chemical potential gradients for components in layers 1 to 3 (mol/mol reaction progress)

Layer	*Si*	*Al*	Fe^{3+}	Fe^{2+}	*Mn*	*Mg*	*Ca*	*Na*	*K*
1	0.0263	-0.0284	-0.2131	-0.0470	-0.0183	0.0228	-0.0188	-0.0315	-0.0026
2	0.0324	-0.0585	-0.2219	-0.0515	-0.0217	0.0182	-0.0036	-0.0048	-0.0004
3	0.0317	-0.0618	-0.2248	-0.0535	-0.0219	0.0176	-0.0007	0.0000	0.0000

Matrix: Cpt

Table 5.9 continued: Modelling Results for corona SK9C

Model Free Energy gradients for phases in layers 1 to 3 (mol^2 component/[(mol mineral).(mol reaction progress)])

Layer	*Grt*	*Crd*	*Opx_{S1}*	*Pl*	*Opx_{S2}*	*Opx_b*	*Qtz*	*Met_1*	*Met_2*
1	-0.2072	0.0000	0.0000	0.0062	0.0054	0.0176	0.3160	0.0421	-0.2028
2	-0.3124	-0.1310	-0.0082	0.0000	0.0000	0.0175	0.3888	0.0884	-0.2784
3	-0.3385	-0.1557	-0.0264	-0.0065	-0.0180	0.0000	0.3807	0.0935	-0.2668

Model Free Energy differences for phases across layers 1 to 3 (m^3mol^2 component/[(mol mineral).(mol^2reaction progress)])

Layer	*Grt*	*Crd*	*Opx_{S1}*	*Pl*	*Opx_{S2}*	*Opx_b*	*Qtz*	*Met_1*	*Met_2*
1	-1.7862E-05	0.0000	0.0000	5.3125E-07	4.6877E-07	1.5145E-06	2.7244E-05	3.6317E-06	-1.7485E-05
2	-4.0106E-06	-1.6814E-06	-1.0497E-07	0.0000	0.0000	2.2508E-07	4.9904E-06	1.1348E-06	-3.5742E-06
3	-9.5115E-06	-4.3736E-06	-7.4242E-07	-1.8200E-07	-5.0702E-07	0.0000	1.0697E-05	2.6272E-06	-7.4961E-06

Model Free Energy differences of phases at boundary q from those at boundary where phase is present (must be ≤0 for stability)

Boundary	*Grt*	*Crd*	*Opx_{S1}*	*Pl*	*Opx_{S2}*	*Opx_b*	*Qtz*
1	0.0000	0.0000	0.0000	-5.3123E-07	-4.6877E-07	-1.7396E-06	-4.2932E-05
2	-1.7862E-05	0.0000	0.0000	0.0000	0.0000	-2.2510E-07	-1.5688E-05
3	-2.1872E-05	-1.6815E-06	-1.0498E-07	0.0000	0.0000	0.0000	-1.0697E-05
4	-3.1384E-05	-6.0549E-06	-8.4739E-07	-1.8200E-07	-5.0703E-07	0.0000	0.0000

For calculation of model affinity -ΔG (m^3mol^2 component/mol^3 reaction progress)

Layer	*Si*	*Al*	*Fe^{3+}*	*Fe^{2+}*	*Mn*	*Mg*	*Ca*	*Na*	*K*	*Total*
1	5.9791E-08	6.9584E-08	3.9143E-06	7.9348E-06	2.8995E-08	1.6551E-06	1.4928E-07	4.1734E-07	5.8612E-10	1.4230E-05
2	1.3473E-08	4.4001E-08	6.3205E-07	1.4168E-06	6.0506E-09	1.5661E-07	8.2236E-10	1.4420E-09	2.0258E-12	2.2713E-06
3	2.8282E-08	1.0726E-07	1.4202E-06	3.3478E-06	1.3438E-08	3.2287E-07	6.4416E-11	3.3281E-17	3.8274E-20	5.2400E-06

Reaction Affinity (m^3mol^{-1}) 0.0000217

5.3.1 Corona overall reactions

Corona product volume proportions were determined from image analysis of BSE images of each corona in MATLAB. The calculated molar volumes and the average composition of each phase in the corona layers were then used to calculate molar phase ratios (Tables 5.5 - 5.9). The overall reaction in each corona was reconstructed by ensuring mass balance for each component *i*.

$$\sum_{k=1}^{\Phi} v_k n_{ik} = 0 \qquad \textit{eqn 5.1}$$

v_k is the stoichiometric coefficient of phase k in the overall reaction, and n_{ik} is the number of moles of component *i* in 1 mole of phase *k*. In an open system, the metasomatic fluxes at the corona boundaries are treated as imaginary phases Met_1 and Met_2.

The final steady-state bulk composition of the corona system is yielded by the right hand side of the following equation:

$$v_{grt} + v_{qtz} + v_{met_1} + v_{met_2} = v_{crd} + v_{opx_{s1,s2,b}} + v_{plg} + v_{kfs} \qquad \textit{eqn 5.1a}$$

The terms $v_{grt} + v_{qtz}$ give the apparent initial bulk composition of the corona system with immediate onset of reaction (Figure 5.24). This measured bulk composition is not the true incipient bulk composition since the composition of garnet (principally X_{Mg}) has been modified though prolonged reaction and open-system interaction with the surrounding rock. The apparent initial bulk compositions may be corrected to yield reasonable estimates of the true initial bulk compositions by adjusting X_{Mg} such that the original compositions of the predicted peak Archaean garnet compositions from THERMOCALC are reproduced (Table 5.10). The final steady-state bulk composition is related to the true initial bulk compositions by the true metasomatic flux vectors $v_{tmet_1} + v_{tmet_2}$ in Figure 5.24. The final steady-state bulk compositions are related to the apparent initial bulk compositions by the apparent metasomatic flux vectors $v_{met_1} + v_{met_2}$. Since corona modelling is concerned with modelling the final steady-state configuration of product layers, reactants and overall reaction affinity, the final reactant compositions and apparent

metasomatic fluxes are used in constraining the overall equation, with open-system modification to the original reactant compositions accommodated in the metasomatic fluxes.

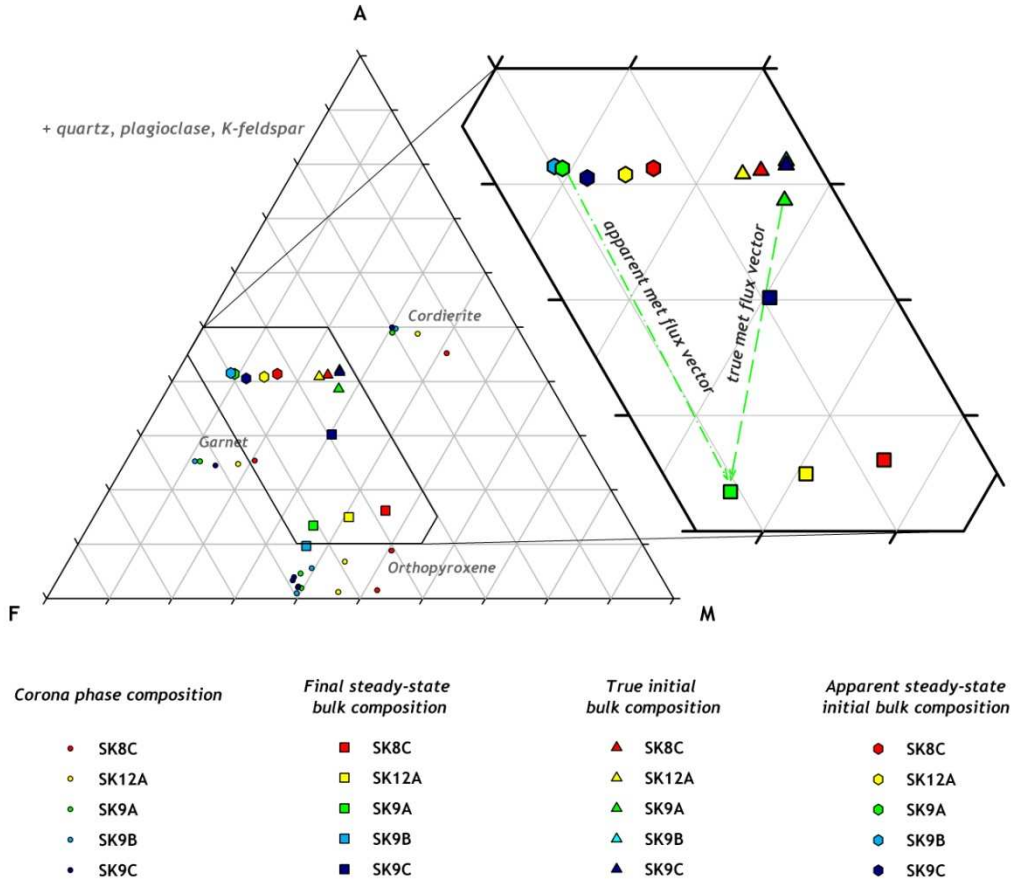

Figure 5.24: AFM diagram with quartz, plagioclase and K-feldspar in excess demonstrating the evolution of corona bulk composition with prolonged reaction. The final steady-state corona bulk composition is that determined from the compositions and relative proportions of corona product phases observed at present. Two potential initial bulk compositions may be generated: an apparent initial bulk composition based on the proportion of garnet consumed in the overall reaction with its current measured composition; and a true initial bulk composition based on a predicted peak garnet composition from THERMOCALC immediately prior to impact. The true initial bulk composition evolves toward the final steady-state corona bulk composition as garnet becomes progressively depleted in Mg in producing a magnesian product assemblage with corona growth, resulting in the relative enrichment of garnet in Fe. The true and apparent initial compositions are related to the final steady-state bulk composition by true and apparent metasomatic flux vectors respectively.

Table 5.10: Molar bulk compositions for SK8C, SK12A, SK9A, SK9B and SK9C coronas

	APPARENT INITIAL MOLAR BULK COMPOSITION									
	SiO_2	$AlO_{3/2}$	$FeO_{3/2}$	FeO	MnO	MgO	CaO	$NaO_{1/2}$	$KO_{1/2}$	X_{Mg}
SK8C	83.83	6.64	0	6.59	0.21	2.5	0.23	0	0	0.28
SK12A	84.08	6.48	0.03	6.81	0.14	2.17	0.29	0	0	0.24
SK9A	88.06	4.86	0.04	5.55	0.24	1.05	0.2	0	0	0.16
SK9B	89.63	4.22	0.06	4.83	0.23	0.84	0.19	0	0	0.15
SK9C	66.75	12.7	1	14.29	1.22	3.46	0.6	0	0	0.19
	INITIAL MOLAR BULK COMPOSITION – THERMOCALC AMENDED X_{Mg}									
	SiO_2	$AlO_{3/2}$	$FeO_{3/2}$	FeO	MnO	MgO	CaO	$NaO_{1/2}$	$KO_{1/2}$	X_{Mg}
SK8C	83.83	6.64	0	5.38	0.21	3.78	0.23	0	0	0.41
SK12A	84.08	6.48	0.03	5.49	0.14	3.5	0.29	0	0	0.39
SK9A	88.06	4.86	0.04	4.15	0.24	3.32	0.2	0	0	0.44
SK9B	89.63	4.22	0.06	3.14	0.23	2.5	0.19	0	0	0.44
SK9C	66.75	12.7	1	10.2	1.22	8.15	0.6	0	0	0.44
	FINAL OPEN SYSTEM MOLAR BULK COMPOSITION									
	SiO_2	$AlO_{3/2}$	$FeO_{3/2}$	FeO	MnO	MgO	CaO	$NaO_{1/2}$	$KO_{1/2}$	X_{Mg}
SK8C	48.69	9.23	0.18	18.21	0.14	22.1	0.45	0.99	0.02	0.55
SK12A	47.47	8.27	1.94	21.53	0	19.79	0.47	0.52	0.01	0.48
SK9A	47.4	7.41	2.35	24.57	0	17.37	0.38	0.52	0.01	0.41
SK9B	49.13	7.08	1.95	23.16	0	15.76	0.81	1.38	0.73	0.4
SK9C	47.75	16.08	0.65	18.82	0.53	14.52	0.63	1.02	0.02	0.44

In Figure 5.25, the variable magnitudes of apparent and true external metasomatic fluxes for components in all coronas are demonstrated. Positive values indicate the influx of material into the corona from an adjacent source and negative values indicate a loss from the corona to an adjacent sink outside of the volume of equilibration considered. The choices of location for component metasomatic fluxes, i.e., at either the quartz or garnet boundary, are those that yield diffusionally stable solutions, (e.g., Ashworth and Sheplev, 1997). The choice to assign Fe and Mg

fluxes to the quartz boundary means that Fe and Mg are not solely derived from garnet to produce blocky orthopyroxene. This minimises both the diffusive flux of Fe and Mg from garnet toward quartz and diffusion coefficients relative to Si required for diffusional stability. This is in agreement with the modelling premise in this study and that of Carlson and Johnson (1991), which models the minimum differences in phenomenological coefficients (L-ratios) for diffusional stability. The inflection in X_{Mg} values for blocky orthopyroxene to higher values comparable to intermediate values for the symplectite orthopyroxene in the same corona is also consistent with metasomatic input of Mg at the boundary with quartz.

Al, Fe, and Mg are the major components entering or exiting the corona domain. The steady-state corona bulk composition, thus, evolves with prolonged reaction, becoming depleted in Al and progressively richer in Fe and Mg (Figure 5.25). Si external fluxes are not considered, since the corona EBC's are silica-saturated, such that changing SiO_2 flux results only in a change in the mode of free quartz in the assemblage (quartz is still stable in the product assemblage). The true and apparent metasomatic fluxes differ primarily with respect to relative fluxes of Fe and Mg components (Figure 5.25). For SK8C and SK12A, the true input metasomatic flux of Mg exceeds Fe at both boundaries in producing a progressively more Mg-rich final steady-state bulk composition from the true initial corona bulk compositions (Figure 5.25). In contrast, the true input metasomatic flux of Fe exceeds Mg in SK9A and SK9B, yielding Fe-rich final steady-state bulk compositions. In SK9C, the output flux of Mg exceeds Fe, resulting in a progressively more Fe-rich final steady-state corona bulk composition. In all coronas, the apparent input metasomatic flux of Mg is higher than Fe. This is an artifact of gradual garnet Fe-enrichment during prolonged corona reaction to compositions more Fe-rich than that required to generate the final steady-state bulk composition. Hence, external Mg input is invoked by mass balance to accommodate the final steady-state composition and may not be an indication of the actual metasomatic fluxes prevailing during corona growth. Both true and apparent metasomatic fluxes require addition of Na, Ca and K to the final steady-state bulk composition to support the observed modes of plagioclase and K-feldspar (SK9B), respectively.

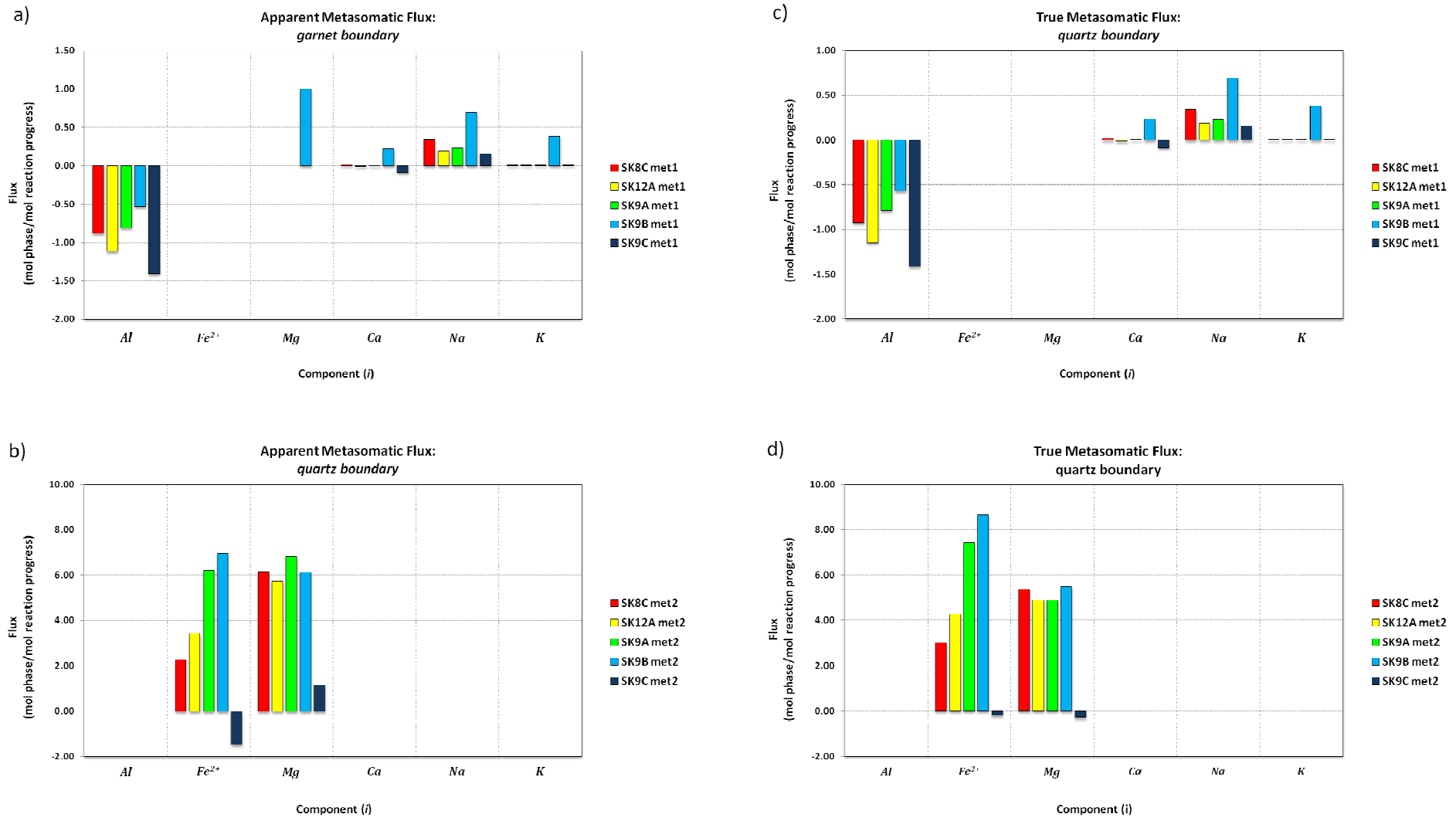

Figure 5.25: True and apparent metasomatic fluxes for open-system diffusion models reported in this study.

5.3.2 L-ratios

Given an overall reaction for each corona, model layer structures were calculated for ratios of Onsager diffusion coefficients or L-ratios, relating component flux to chemical potential gradients (Appendix A; Joesten, 1977; Mongkoltip and Ashworth, 1983; Foster, 1986; Grant, 1988; Johnson and Carlson, 1990; Carlson and Johnson, 1991; Ashworth and Birdi, 1990; Ashworth et al., 1992; Ashworth and Sheplev, 1997; Markl et al., 1998; Ashworth et al., 1998).

Input L-ratios yielding diffusionally stable solutions for corona models are included in Figure 5.26. L_{ii} expresses linear proportionality between flux of component *i* and its chemical potential gradient (Joesten, 1977). Model L-ratios are defined as ratios of component diffusion coefficients relative to Si, i.e., L_{SiSi}/L_{ii}. The contribution to the flux of a component that results from the chemical potential gradient of another component is assumed to be negligible (i.e., $L_{ij} = 0$, where $i \neq j$) in agreement with Ashworth and Sheplev, (1997). L-ratios are also assumed to remain constant across the reaction band or layer. In Figure 5.26, $L_{SiSi}/L_{ii} = 1$ represents a line of equality, such that any L-ratios plotting along this line indicate no relative difference in intergranular diffusion rate of component *i* relative to Si. L-ratios plotting below 1 suggest more rapid diffusion of component *i* relative to Si. Conversely, L-ratios plotting above 1 indicate slower diffusion of component *i* relative to Si. A range of L-ratios for a particular corona will yield stable solutions. Following the rationale of Carlson and Johnson (1991), the L-ratios accepted for models were those as close as possible to unity, i.e., representative of the minimum differences of phenomenological coefficients required in order to generate diffusionally stable models.

In all coronas, $L_{SiSi}/L_{ii} < 1$ for components Fe^{2+}, Mg, Ca, Na and K (the actual diffusing species is component oxide; Joesten, 1977). Fe^{2+} and Mg exhibit the lowest L-ratios and are, thus, the most rapidly diffusing species, followed by Ca, Na and K. Al is the only component for which $L_{SiSi}/L_{ii} > 1$. Al is, thus, the slowest diffusing of all components relative to Si. These relative differences in intergranular diffusivities manifest as partitioning of the steady-state corona bulk composition from garnet towards quartz into a 'proximal' aluminous symplectite, followed by a

plagioclase-bearing symplectite accommodating more rapidly diffusing alkalis, terminated by a 'distal', alumina-deficient, monomineralic blocky orthopyroxene layer comprising the most rapidly diffusing ferromagnesian components. In SK9B, K diffuses nearly twice as fast as it does in all other coronas modelled, thereby stabilizing a K-feldspar layer adjacent to blocky orthopyroxene (e.g., Figure 5.2d). In SK8C, SK12A and SK9B, Al diffuses more slowly than Si (SK8C L_{SiSi}/L_{AlAl} = 5.8; SK12A L_{SiSi}/L_{AlAl} = 3.5; SK9B L_{SiSi}/L_{AlAl} = 1.5). In SK9A and SK9C, there is no relative difference in intergranular diffusion coefficients between Al and Si (L_{SiSi}/L_{AlAl} = 1.0), reflecting more rapid diffusion of Al in these coronas than in SK8C, SK12A and SK9B.

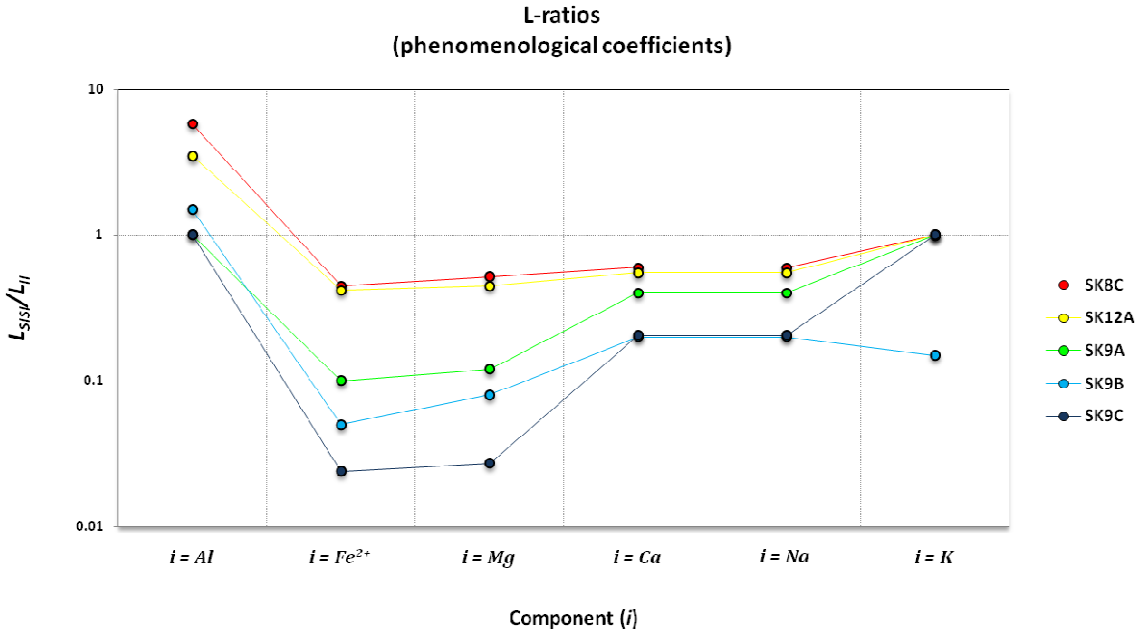

Figure 5.26: L-ratios for stable diffusion models for coronas SK8C, SK12A, SK9A, SK9B and SK9C.

5.3.3 Corona product proportions

Corona product phase proportions were determined by image analysis in MATLAB of BSE images of the respective coronas (Figure 5.27). Corona product proportions vary between the coronas, reflecting differences in local bulk composition caused by metasomatic exchange of components with the matrix during reaction. The proportion of cordierite decreases from 0.38 in SK8C, to 0.37 in SK12A and 0.34 in SK9A, with lowest cordierite proportions of 0.22 in SK9B. SK9C cordierite proportion is markedly higher at 0.57. The inverse relationship for blocky Opx_b is observed, with the proportion of Opx_b increasing from 0.43 in SK8C to 0.44 in SK12A, 0.53 in SK9A and 0.58 in SK9B. The proportion of Opx_b is lowest in SK9C at 0.19. The overall proportion of orthopyroxene in the coronas increases from 0.55 in SK8C to 0.58 in SK12A and 0.61 in SK9A. Overall orthopyroxene modes are lower in SK9B (0.60) and lowest in SK9C (0.37). Plagioclase and K-feldspar modes are highest in SK9B (0.12 for plagioclase and 0.06 for K-feldspar). K-feldspar is absent in other coronas and plagioclase is present in far lower proportions (0.08 in SK8C, 0.05 in SK12A, 0.05 in SK9A and 0.06 in SK9C) compared to SK9B. Higher cordierite modes and lower overall orthopyroxene modes in SK9C relative to SK9A reflect the overall less silicic, more aluminous, bulk composition of SK9C (Table 5.10, Figure 5.24). Likewise, higher plagioclase modes, lower cordierite modes and the presence of K-feldspar are indicative of the more alkali-rich, siliceous bulk composition of SK9B compared to SK9A and SK9C (Table 5.10, Figure 5.24).

A critical caveat must be made with regard to the significance of corona product modes. It has been established that the coronas cannot be treated as closed systems for any component. The implication of this is that only a portion of the actual EBC has been sampled within each model boundary. It is not possible to use the measured modes of the phases within the model boundary/framework to infer the actual composition of the EBC, e.g., the reduced mode of cordierite in SK9A may lead one to assume reduced $a H_2O$ in the EBC of which it forms only a part. In reality, SK9A forms part of a larger EBC in which cordierite modes are actually slightly higher than orthopyroxene modes overall (see Chapter 4, Section 4.3.1). The discrepancy

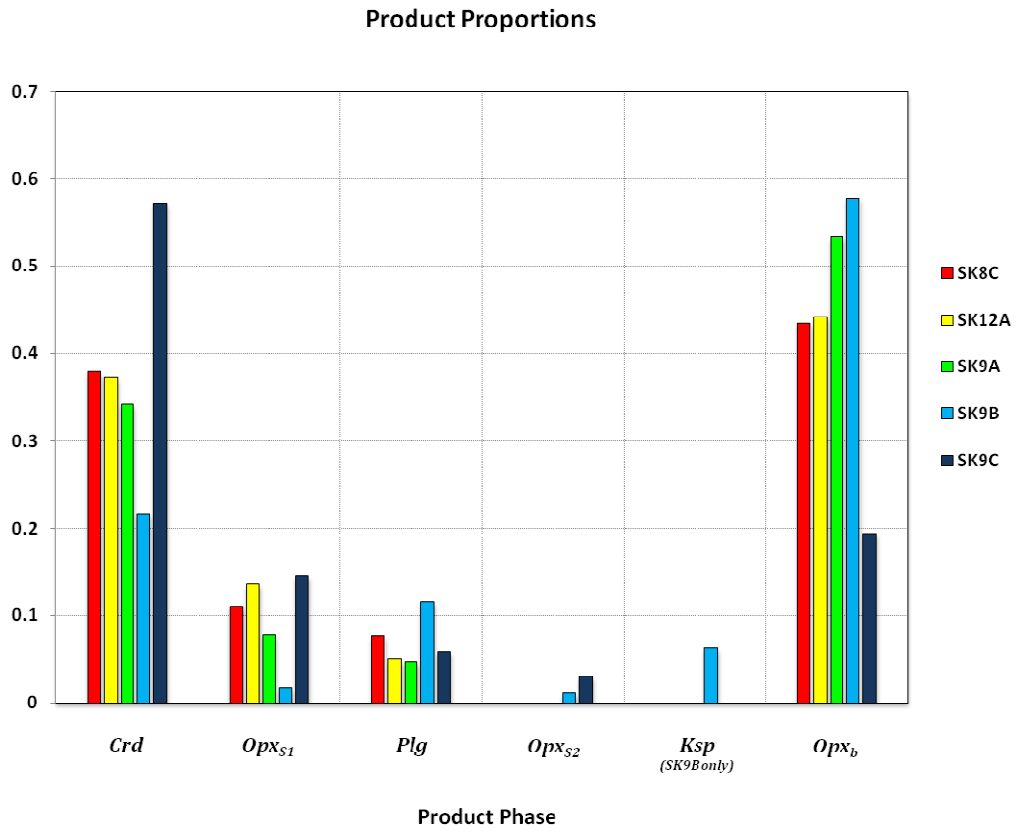

Figure 5.27: Observed proportions of corona product phases determined by image analysis.

arises because boundaries need to be imposed on a portion of the EBC to facilitate modelling, with external fluxes required to accommodate chemical communication with the remaining EBC as a whole. Within the model boundaries from relict garnet to quartz reactant in SK9A, orthopyroxene modes are high compared to SK8C and SK12A. The high modes of orthopyroxene reflect the preferential, rapid diffusion of FeO and MgO from sources within the EBC external to the model boundaries toward the quartz inclusion, which acts as a sink for rapidly diffusing FeO and MgO. The mode of orthopyroxene is raised locally within the SK9A model framework, resulting in an apparent depletion in cordierite within the model boundary. If the model boundaries are expanded so as to approach that of the real EBC, cordierite mode will increase as portions of the EBC comprising less mobile components ($AlO_{3/2}$) are included within the model framework. The model overall reaction will be different from that for the actual EBC, i.e., principally larger reaction coefficients will be required for blocky orthopyroxene (Opx_b) with larger attendant FeO and

MgO fluxes at model boundaries. Since reaction affinity is dependent on chemical potential gradients across layers, regardless of bulk composition and modelled overall reaction, the reaction affinity determined in a portion of the EBC should be indicative of the extent of equilibration within the EBC as a whole, assuming constancy of diffusion coefficients for all components thoughout.

5.3.4 Component fluxes

By definition, component flux (J_i^q) in layer q is given by the summation of the quantities of components liberated in reactions up to boundary *r* and is given by the following equation (Joesten, 1977; Appendix A):

$$J_i^q = n_i^{qleft}.\bar{v} + n_i^q.\bar{v}^q \qquad \textit{eqn 5.2}$$

Where J_i^q = flux of component *i* in layer *q*; n_i^{qleft} = moles component *i* in the layer to the left of layer q toward garnet; $\bar{v}$ = overall reaction coefficients for phases; n_i^q = moles of component *i* in layer *q*; $\bar{v}^q$ = reaction coefficients at boundary *r* immediately to the left of layer *q*. The term $n_i^q.\bar{v}^q$ is always negative since the reaction coefficients for product phases are negative.

In qualitative terms, the component flux can be described as the difference between the molar amount of component *i* required at boundary *r* to yield layer *q* ($n_i^q.\bar{v}^q$) and the amount initially liberated by the garnet reactant and metasomatic influx at the garnet boundary, less the molar amount of that component in layers to the left of layer *q*, ($n_i^{qleft}.\bar{v}$). The magnitude of the fluxes and their sign, either negative or positive, reflect the balance expressed in the equation above. The convention in diffusion modelling when referring to diffusing components is to use the element symbol alone, e.g., Si for SiO_2 (e.g., Joesten, 1977; Mongkoltip and Ashworth, 1983; Foster, 1986; Grant, 1988; Johnson and Carlson, 1990; Carlson and Johnson, 1991; Ashworth and Birdi, 1990; Ashworth et al., 1992; Ashworth and Sheplev, 1997; Markl et al., 1998; Ashworth et al., 1998).

Flux relationships in all layers across theoretical coronas are demonstrated in Figure 5.28 and Figure 5.29. In layer 1 (cordierite and orthopyroxene symplectite), positive component fluxes indicate material transport from the garnet reactant or metasomatic influx at the garnet boundary ($n_i^{qleft}.\bar{v}$) exceeds the amount required to stabilize corona product phases in the layer ($n_i^q.\bar{v}^q$) (Figure 5.28). Excess material is able to diffuse to further potential reaction sites down chemical potential gradients toward quartz (Figure 5.28). Conversely, negative fluxes indicate that the amount of component *i* liberated by garnet and metasomatic losses or gains at the garnet boundary is not sufficient to produce the product phases of the appropriate compositions in the observed proportions (Figure 5.29). Flux of material from the opposite direction (i.e., either from the quartz reactant or metasomatic influx at the quartz boundary) must be invoked to stabilize the layer assemblage (Figure 5.29).

The relative magnitudes of component fluxes reflect a balance between concentration of a component in the reactant, the metasomatic influx of that component into the garnet or quartz boundaries in an open system, and the modes and compositions of the product layers. Very large positive fluxes suggest either large molar amounts of component *i* liberated from reactant garnet or high metasomatic influx at boundary 1, coupled with low modes of cordierite and orthopyroxene in layer 1 or a low concentration of that component in the symplectite phases. Very large negative fluxes are associated with comparatively small amounts of component *i* in garnet or loss of component *i* to the external system at boundary 1, compounded by higher modes of cordierite and orthopyroxene in layer 1 or a high concentration of component *i* in these phases.

In subsequent layers, fluxes reflect the same constraints on material balance as in layer 1, except that the molar amount of a component diffusing from reactant garnet and Met_1 input is reduced by the molar amount of a component in the previous layer. Typically, a layer (*q*) grows at boundary *r* and breaks down at boundary *r+1*, thus liberating an amount of component *i* reflecting the relative proportions and compositions of phases in layer *q* (Figure 5.28 and 5.29). Large positive inflections in fluxes of components in layer *q* occur when the molar amounts of component *i* yielded by the consumption of phases in the previous layer *q-1* at the preceding

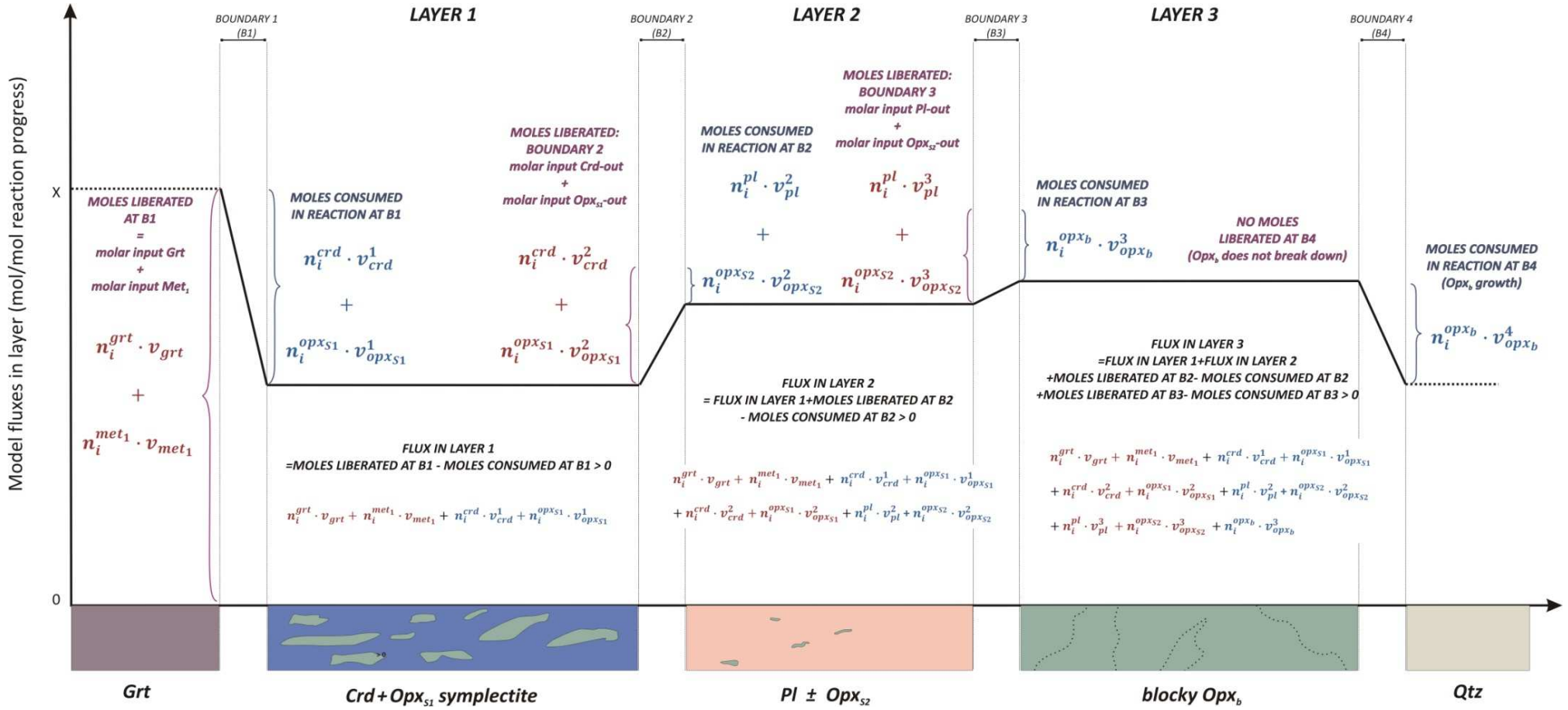

Figure 5.28: Development of positive fluxes over a corona band in a model system. The amount of component i liberated by garnet and metasomatic influx at the garnet boundary ($n_i^{qleft} . \overline{v}$) exceeds the amount required to stabilize corona product phases in the layer 1 ($n_i^q . \overline{v}^q$), such that J_i^q is >0. Excess material is able to diffuse to further potential reaction sites down chemical potential gradients towards quartz.

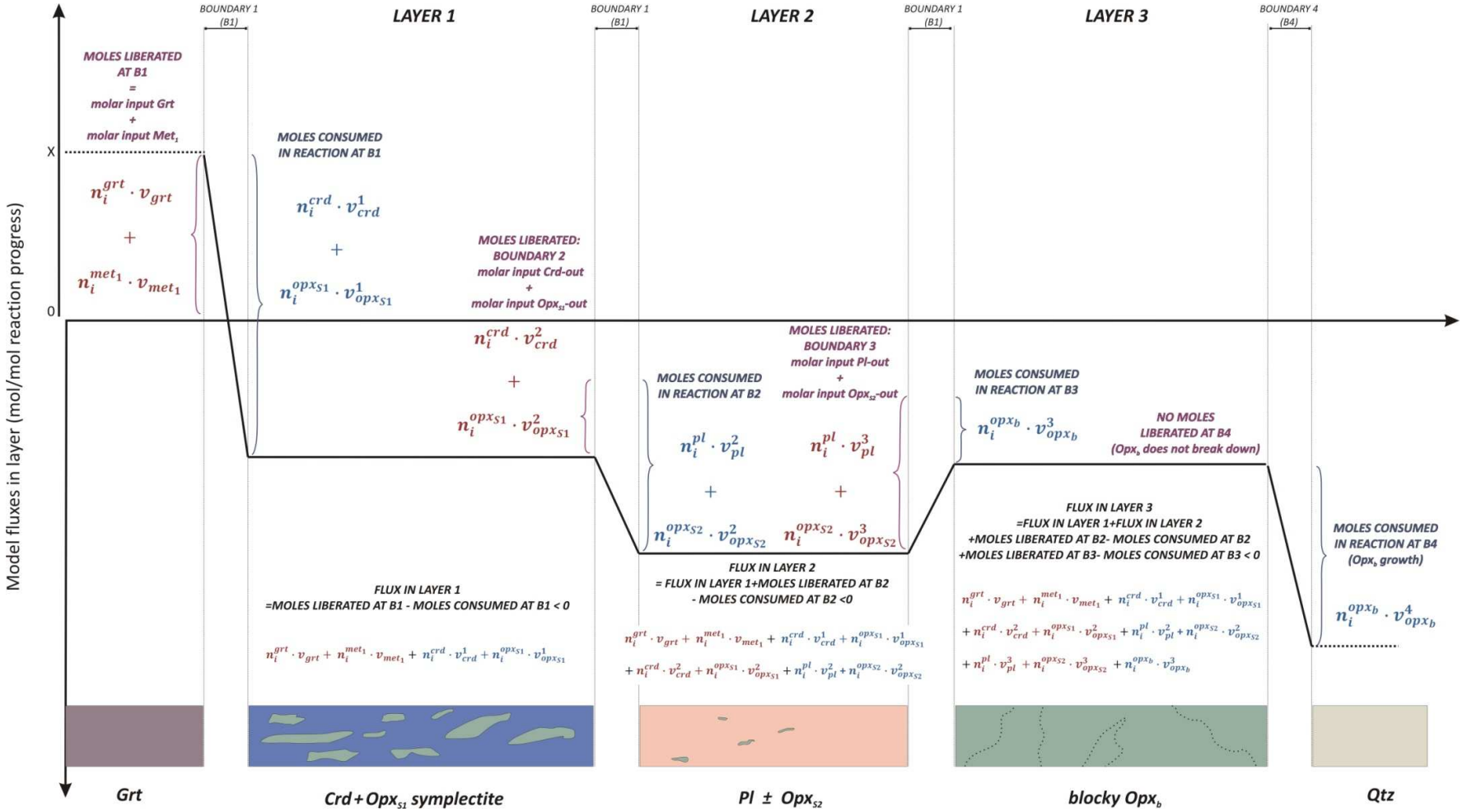

Figure 5.29: Development of negative fluxes over a corona band. The amount of component i liberated by garnet and metasomatic influx at the garnet boundary is not sufficient to produce the product phases of the appropriate compositions in the observed proportions in layer 1, i.e., J_i^q is <0. Flux of material from quartz or metasomatic influx at the quartz boundary must be invoked to stabilize the layer assemblage

boundary *r* greatly exceed the amounts consumed in producing layer *q* phases (e.g., layer 2 in Figure 5.28). This occurs either because of large positive reaction coefficients for phases in layer *q-1* at boundary *r*, i.e., large amounts of component *i* liberated by consumption of high proportions of products of layer *q-1* ($n_i^{qleft}.\bar{v}$ increases), or low concentrations of component *i* consumed in producing phases of layer *q* with low overall modes in the corona assemblage ($n_i^q.\bar{v}^q \rightarrow 0$). Large negative flux inflections occur in layer *q* (e.g., layer 2 in Figure 5.29) when the molar amount of component *i* liberated at the preceding boundary *r* through the breakdown of phases in the previous layer *q-1* is markedly less than that required to form the phases in the observed proportions and compositions in layer *q*. Diffusion of the requisite molar amounts of component *i* is induced from the opposite direction from quartz toward garnet to accommodate the deficiency in molar *i* at boundary *r*.

Component fluxes in layers of each individual corona are presented in Figure 5.30a-g and Tables 5.5-5.9. Fluxes were also calculated independently in Excel through manual solution of equation 5.2 for each layer individually as a check on the matrix algebra in the Matlab model (Table 5.11). Manually calculated fluxes are also useful in demonstrating the nature of material transfer through each layer and mass balance with reaction at layer boundaries schematically (Figures 5.31-5.44). Fluxes calculated manually are equivalent to those determined by Matlab. In some rare instances, the manually calculated flux differs by < 0.0005 mol from the Matlab flux. This results in a deviation by 0.001 with rounding to three decimal places. The variation between manual and Matlab fluxes is attributed to the greater number of significant figures included during the Matlab modelling of reaction coefficients at layer boundaries throughout iterative calculation and is not considered significant.

Variation in Si flux across all coronas is shown in Figure 5.30a. Si fluxes in layer 1 cordierite and orthopyroxene symplectite from all coronas are negative since the molar SiO_2 required to stabilise the formation of the symplectite requires diffusion from quartz toward Si-deficient garnet. The Si flux relationships for SK9C, SK9B and SK8C are demonstrated schematically in Figures 5.31-5.33, respectively. A marked increase in the magnitude of negative Si flux across plagioclase-bearing layer 2 in all coronas (e.g., Figures 5.31, 5.32 and 5.33) and K-feldspar layer 3 in

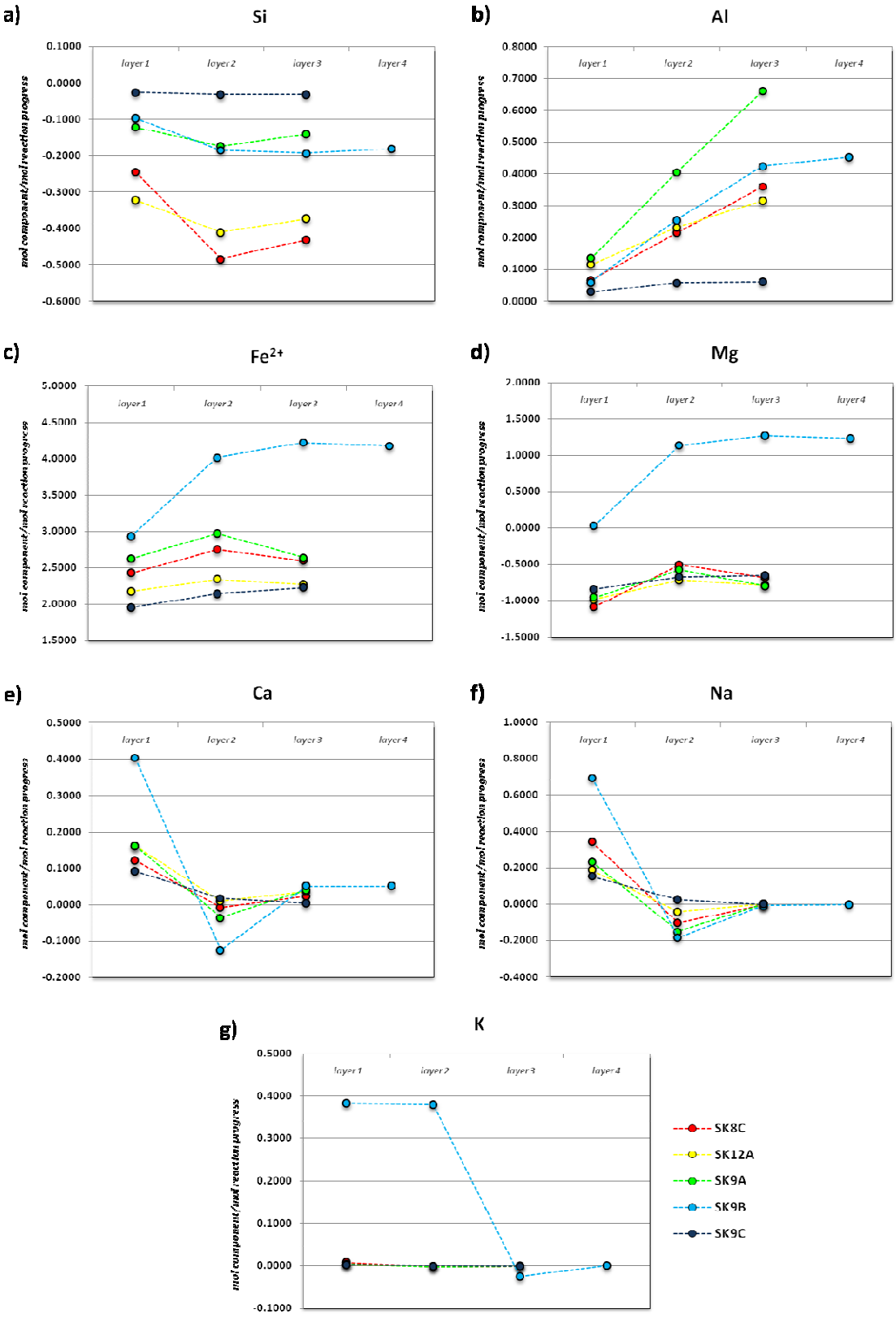

Figure 5.30: Model component fluxes for each component in corona layers

Table 5.11: Component fluxes through layers and molar amounts of components liberated and consumed at layer boundaries (reported at 3 decimal places).

	Fe^{2+}					Mg					Si					Al				
	SK8C	**SK12A**	**SK9A**	**SK9B**	**SK9C**	**SK8C**	**SK12A**	**SK9A**	**SK9B**	**SK9C**	**SK8C**	**SK12A**	**SK9A**	**SK9B**	**SK9C**	**SK8C**	**SK12A**	**SK9A**	**SK9B**	**SK9C**
Molar input garnet + met 1	4.054	4.290	4.675	4.700	4.326	1.538	1.367	0.883	1.814	1.047	6.002	5.962	5.945	5.920	5.922	3.206	2.967	3.284	3.568	2.434
Moles consumed B1	-1.631	-2.117	-2.044	-1.767	-2.368	-2.617	-2.347	-1.837	-1.782	-1.890	-6.246	-6.284	-6.067	-6.017	-5.948	-3.139	-2.853	-3.151	-3.507	-2.405
Flux in layer 1	2.423	2.173	2.631	2.933	1.958	-1.079	-0.980	-0.954	0.032	-0.843	-0.244	-0.323	-0.122	-0.097	-0.026	0.067	0.115	0.133	0.060	0.028
Moles liberated B2	0.328	0.169	0.343	1.490	1.768	0.575	0.263	0.385	1.372	1.178	1.462	0.881	1.449	4.312	3.195	0.832	0.616	0.985	2.150	0.497
Moles consumed B2	0.000	0.000	0.000	-0.404	-1.582	0.000	0.000	0.000	-0.269	-1.007	-1.702	-0.970	-1.500	-4.399	-3.201	-0.684	-0.499	-0.714	-1.954	-0.466
Flux in layer 2	2.751	2.342	2.974	4.019	2.145	-0.504	-0.717	-0.569	1.135	-0.672	-0.484	-0.411	-0.173	-0.184	-0.032	0.216	0.232	0.405	0.256	0.059
Moles liberated B3	0.000	0.000	0.000	0.206	1.279	0.000	0.000	0.000	0.137	0.814	0.388	0.172	0.589	1.563	2.031	0.156	0.088	0.280	0.649	0.102
Moles consumed B3	-0.155	-0.072	-0.330	0.000	-1.196	-0.174	-0.062	-0.224	0.000	-0.795	-0.335	-0.134	-0.556	-1.573	-2.030	-0.011	-0.004	-0.025	-0.480	-0.099
Flux in layer 3	2.596	2.270	2.644	4.225	2.228	-0.678	-0.779	-0.794	1.271	-0.652	-0.430	-0.373	-0.141	-0.193	-0.032	0.360	0.316	0.660	0.425	0.062
Moles liberated B4	0.000	0.000	0.000	0.000	0.000	0.000	0.000	0.000	0.000	0.000	0.000	0.000	0.000	0.097	0.000	0.000	0.000	0.000	0.030	0.000
Moles consumed B4	-4.868	-5.702	-8.862	-0.050	-0.750	-5.462	-4.954	-6.024	-0.033	-0.480	-10.487	-10.692	-14.928	-0.084	-1.258	-0.360	-0.316	-0.660	-0.002	-0.062
Molar input quartz + met 2 at B4	-2.273	-3.432	-6.218	-	1.478	-6.140	-5.733	-6.818	-	-1.133	-10.917	-11.065	-15.069	-	-1.290	0.000	0.000	0.000	-	0.000
Flux in layer 4 (SK9B)				4.175					1.238					-0.180					0.453	
Moles liberated B5				0.000					0.000					0.000					0.000	
Moles consumed B5				-11.147					-7.368					-18.660					-0.453	
Molar input quartz + met 2 (SK9B only) at B5				-6.972					-6.130					-18.840					0.000	

Table 5.11 continued: Component fluxes through layers and molar amounts of components liberated and consumed at layer boundaries.

	Ca					Na					K				
	SK8C	**SK12A**	**SK9A**	**SK9B**	**SK9C**	**SK8C**	**SK12A**	**SK9A**	**SK9B**	**SK9C**	**SK8C**	**SK12A**	**SK9A**	**SK9B**	**SK9C**
Molar input garnet + met 1	0.155	0.168	0.168	0.407	0.095	0.342	0.188	0.232	0.694	0.154	0.008	0.003	0.004	0.383	0.003
Moles consumed B1	-0.034	-0.006	-0.005	-0.004	-0.004	0.000	0.000	0.000	0.000	0.000	0.000	0.000	0.000	0.000	0.000
Flux in layer 1	0.121	0.162	0.162	0.403	0.092	0.342	0.188	0.232	0.694	0.154	0.008	0.003	0.004	0.383	0.003
Moles liberated B2	0.006	0.000	0.001	0.004	0.003	0.000	0.000	0.000	0.000	0.000	0.000	0.000	0.000	0.000	0.000
Moles consumed B2	-0.134	-0.152	-0.197	-0.532	-0.077	-0.444	-0.228	-0.381	-0.875	-0.130	-0.010	-0.003	-0.007	-0.003	-0.002
Flux in layer 2	-0.007	0.010	-0.035	-0.125	0.018	-0.101	-0.040	-0.150	-0.181	0.023	-0.002	0.001	-0.003	0.379	0.000
Moles liberated B3	0.031	0.027	0.077	0.176	-0.009	0.101	0.040	0.150	0.286	-0.023	0.002	0.001	0.003	0.001	0.000
Moles consumed B3	-0.001	0.000	-0.002	0.001	-0.005	0.000	0.000	0.000	-0.111	0.000	0.000	0.000	0.000	-0.405	0.000
Flux in layer 3	0.023	0.036	0.041	0.051	0.003	0.000	0.000	0.000	-0.007	0.000	0.000	0.000	0.000	-0.025	0.000
Moles liberated B4	0.000	0.000	0.000	0.000	0.000	0.000	0.000	0.000	0.007	0.000	0.000	0.000	0.000	0.025	0.000
Moles consumed B4	-0.023	-0.036	-0.041	0.000	-0.0003	0.000	0.000	0.000	0.000	0.000	0.000	0.000	0.000	0.000	0.000
Molar input quartz + met 2	0.000	0.000	0.000		0.000	0.000	0.000	0.000		0.000	0.000	0.000	0.000		0.000
Flux in layer 4 (SK9B)				0.051					0.000					0.000	
Moles liberated B5				0.000					0.000					0.000	
Moles consumed B5				-0.051					0.000					0.000	
Molar input quartz + met 2 (SK9B only) at B5				0.000					0.000					0.000	

SK9B (Figure 5.32) is followed by a slight decrease in negative flux over the final blocky orthopyroxene layer toward garnet. The increase in negative Si flux over layer 2 is due to the more siliceous nature of the feldspathic layer, increasing the amount of SiO_2 consumed at boundary 2 in the production of plagioclase, i.e., $n_{Mg}^{pl}.v_{pl}^{2}$ increases. The molar amount of SiO_2 liberated at boundary 2 with the decomposition of cordierite and orthopyroxene is less than that required to form plagioclase-bearing layer 2 (Table 5.11; Figures 5.31-5.33), thus inducing an increase in the molar amount of SiO_2 diffusing from quartz toward boundary 2 to accommodate the deficiency. Negative Si fluxes in the blocky orthopyroxene layer are slightly suppressed owing to the comparatively small reaction coefficient $v_{opx_b}^{3}$, thereby reducing the magnitude of $n_i^{opx_b} \cdot v_{opx_b}^{3}$, such that the molar amount of SiO_2 consumed at the preceding boundary in producing blocky orthopyroxene is less than that liberated by the decomposition of the feldspathic layer to the left, hence, less SiO_2 is required to diffuse from reactant quartz.

Lowest-magnitude negative Si fluxes are observed in SK9C, where the molar amount of SiO_2 consumed to produce layer 1 symplectite is markedly less than in all other coronas (Figure 5.31) and approaches that liberated from the garnet reactant at boundary 1. Low Si fluxes are consistent with the high mode of cordierite in SK9C corona and an overall Si-deficient bulk composition. Accordingly, lower Si fluxes are required from quartz toward garnet to stabilize the silica-deficient product assemblage. Conversely, the higher modes of orthopyroxene in the layer 1 symplectites of SK12A (Figure 5.30a) and SK8C (Figures 5.30a, 5.33) require greater amounts of molar SiO_2 be consumed at boundary 1 for formation of the more siliceous symplectites, thereby inducing higher-magnitude negative Si fluxes in all layers from quartz for stability.

Variation of Al flux throughout the coronas is shown in Figure 5.30b. Al fluxes are positive in all coronas and increase steadily in magnitude from garnet to reactant quartz. Highest-magnitude Al fluxes are modelled in SK9A (Table 5.11, Figure 5.34) and lowest-magnitude Al fluxes are observed in SK9C (Table 5.11, Figure 5.35). In all layers, the amount of Al liberated at each boundary exceeds the amount

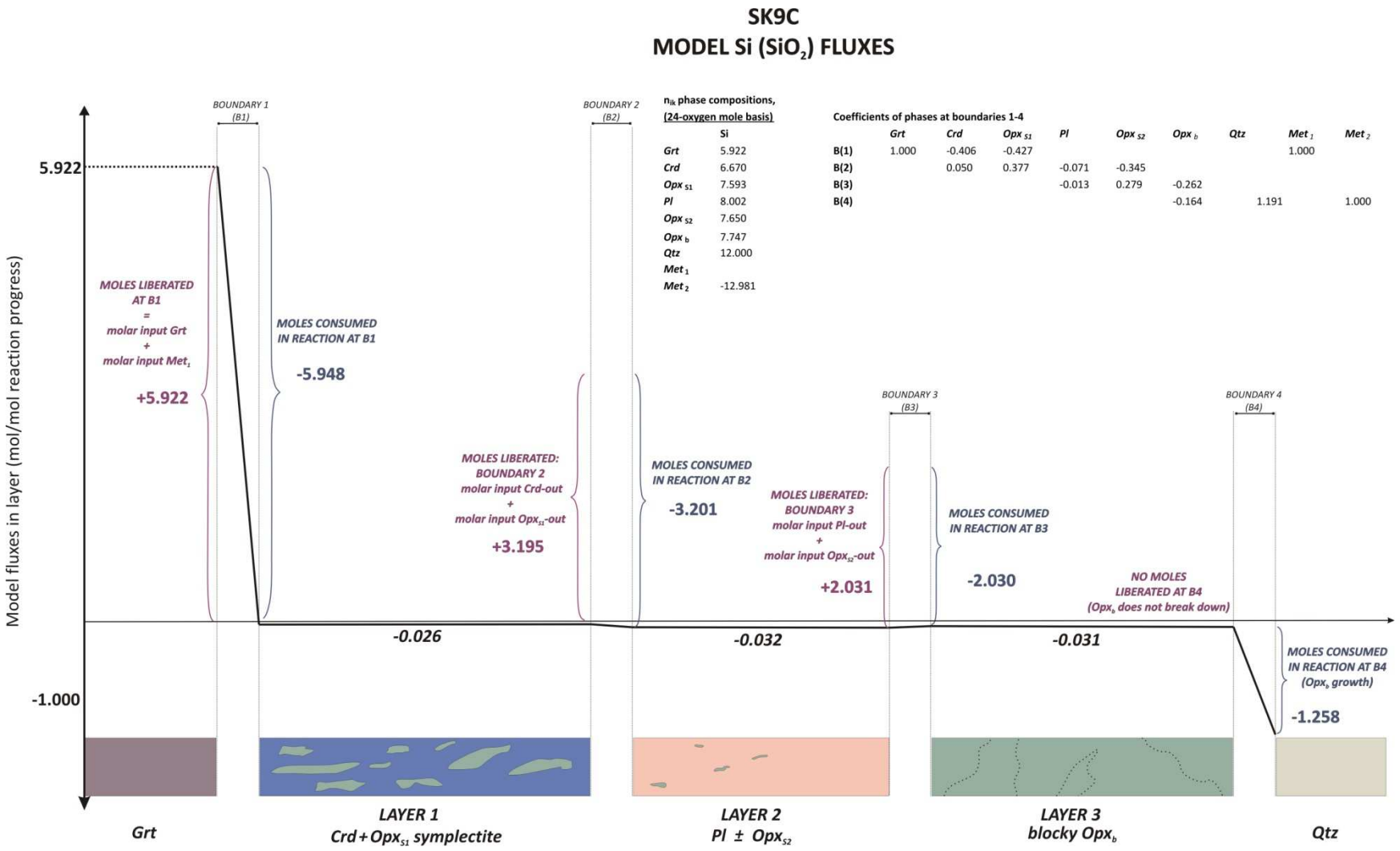

Figure 5.31: Development of negative fluxes for SiO_2 over corona layers in SK9C.

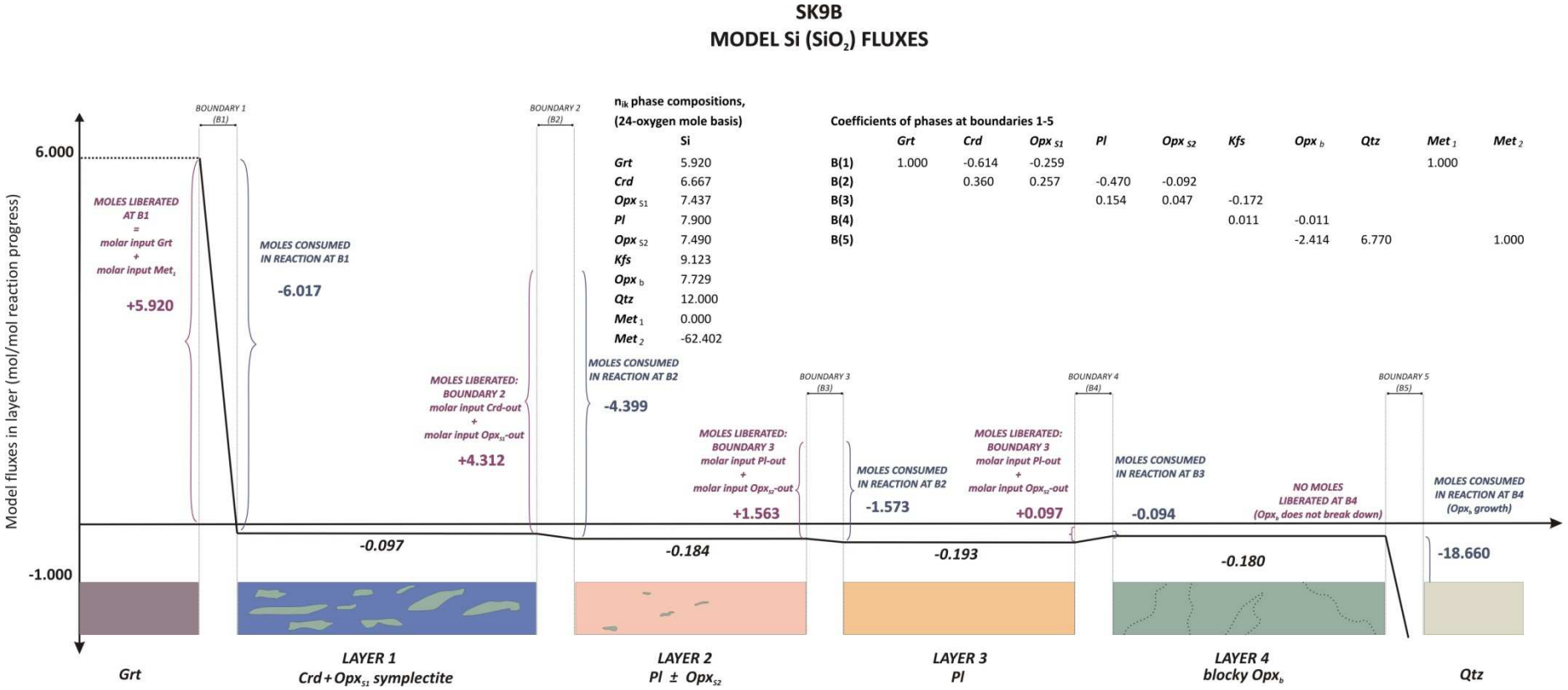

Figure 5.32: Development of negative fluxes for SiO_2 over corona layers in SK9B.

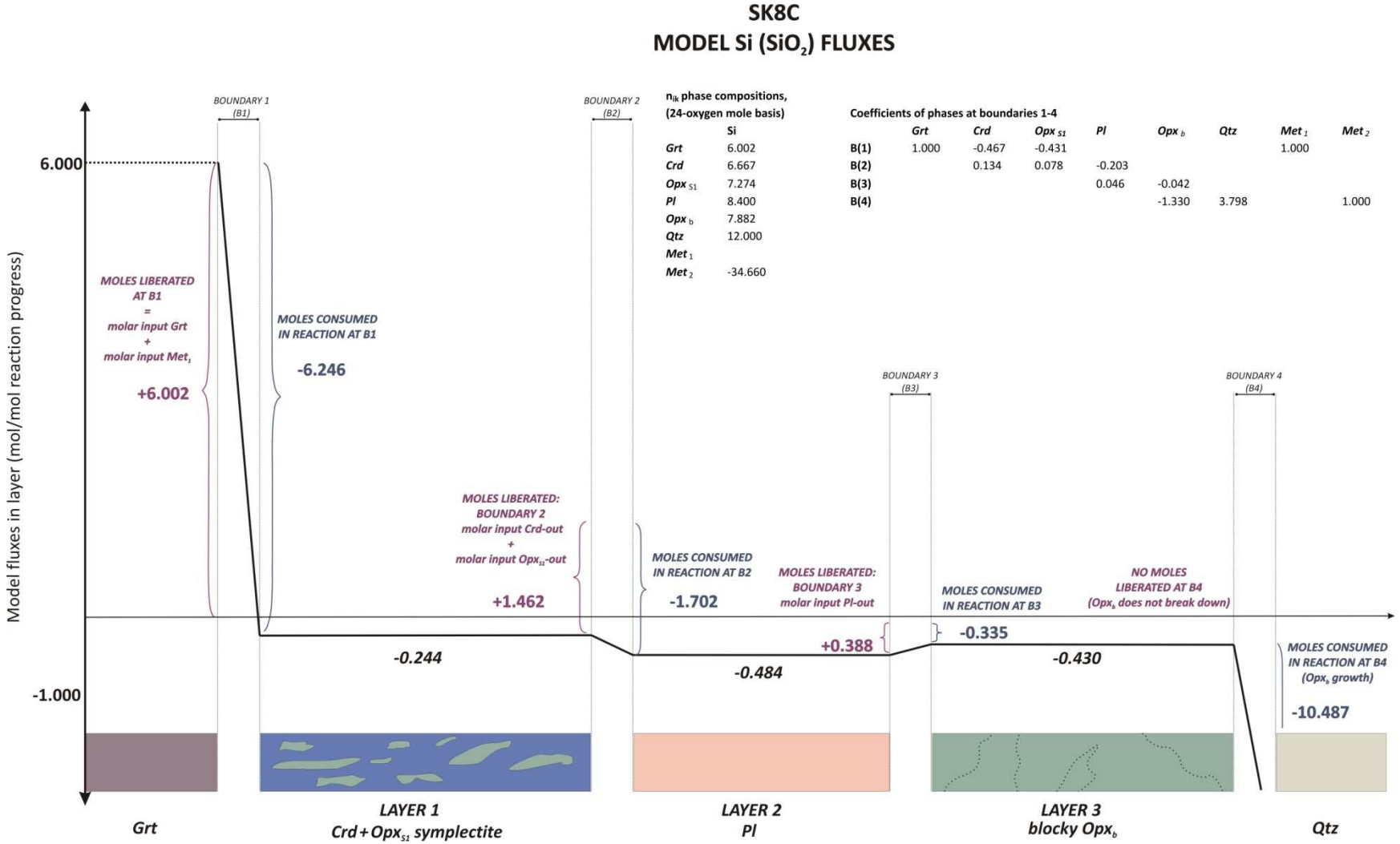

Figure 5.33: Development of negative fluxes for SiO_2 over corona layers in SK8C.

required in production of phases of the requisite composition and proportions in the following layer. The steady increase in Al fluxes across layers reflects progressively decreasing magnitudes of the term $n_{Al}^{q}.\bar{v}^{q}$, i.e., progressively smaller molar amounts of $AlO_{3/2}$ are consumed at reaction boundaries towards quartz, e.g., SK9A in Figure 5.34 and SK9C in Figure 5.35. In plagioclase-bearing layer 2, this is owing to a small reaction coefficient at boundary 2 despite the higher n_{Al}^{q} required to form plagioclase in layer 2. In blocky orthopyroxene layers (layer 3 for SK8C, SK12A, SK9A and SK9C and layer 4 for SK9B), the reduction in $n_{Al}^{opx_b}.v_{opx_b}^{3}$ is owing to a small negative reaction coefficient for Opx_b (-0.04 in SK8C) and lower Al contents in blocky orthopyroxene compared to preceding layers (Table 5.11, Figures 5.34, 5.35). Al flux is highest in all layers of SK9A (Figure 5.34) where the amount of Al lost to the system at the garnet boundary in Met_1 (-0.81 mol) is lowest compared to all other coronas and the molar amounts of $AlO_{3/2}$ liberated by reaction at succeeding boundaries exceeds that for other coronas. Conversely, Al flux is lowest in SK9C (Figure 5.35) in layer 1, where the amount of $AlO_{3/2}$ lost to the surrounding rock is largest (-1.41 mol), thus minimizing input molar $AlO_{3/2}$ into boundary 1 (+2.434 mol). Almost all of the $AlO_{3/2}$ available for reaction is consumed at boundary 1 (-2.405 mol), thereby minimizing excess Al diffusing though the layer to sinks down the chemical potential gradient in the corona. Flux magnitudes in SK9C remain at low values in succeeding layers in SK9C owing to similar magnitudes of liberated and consumed molar $AlO_{3/2}$ at each boundary.

Ferric iron flux variation throughout the coronas is shown in Figure 5.30c. Fe^{2+} fluxes are positive in all layers in all coronas and are the highest in magnitude compared to other components, reflecting the relatively large difference in the molar amount liberated from an almandine-rich garnet reactant and the amount required to stabilise the corona product compositions and proportions. Positive Fe^{2+} fluxes suggest transport from boundary 1 adjacent to garnet towards quartz. The positive flux relationships for Fe^{2+} in SK12A are demonstrated in Figure 5.36 and for SK9B in Figure 5.37. A positive inflection is commonly observed for Fe^{2+} in plagioclase-bearing layer 2 in all coronas and also over K-feldspar layer 3 in SK9B. In SK12A, Fe^{2+} fluxes increase at boundary 2 from +2.17 to +2.34 mol per unit reaction

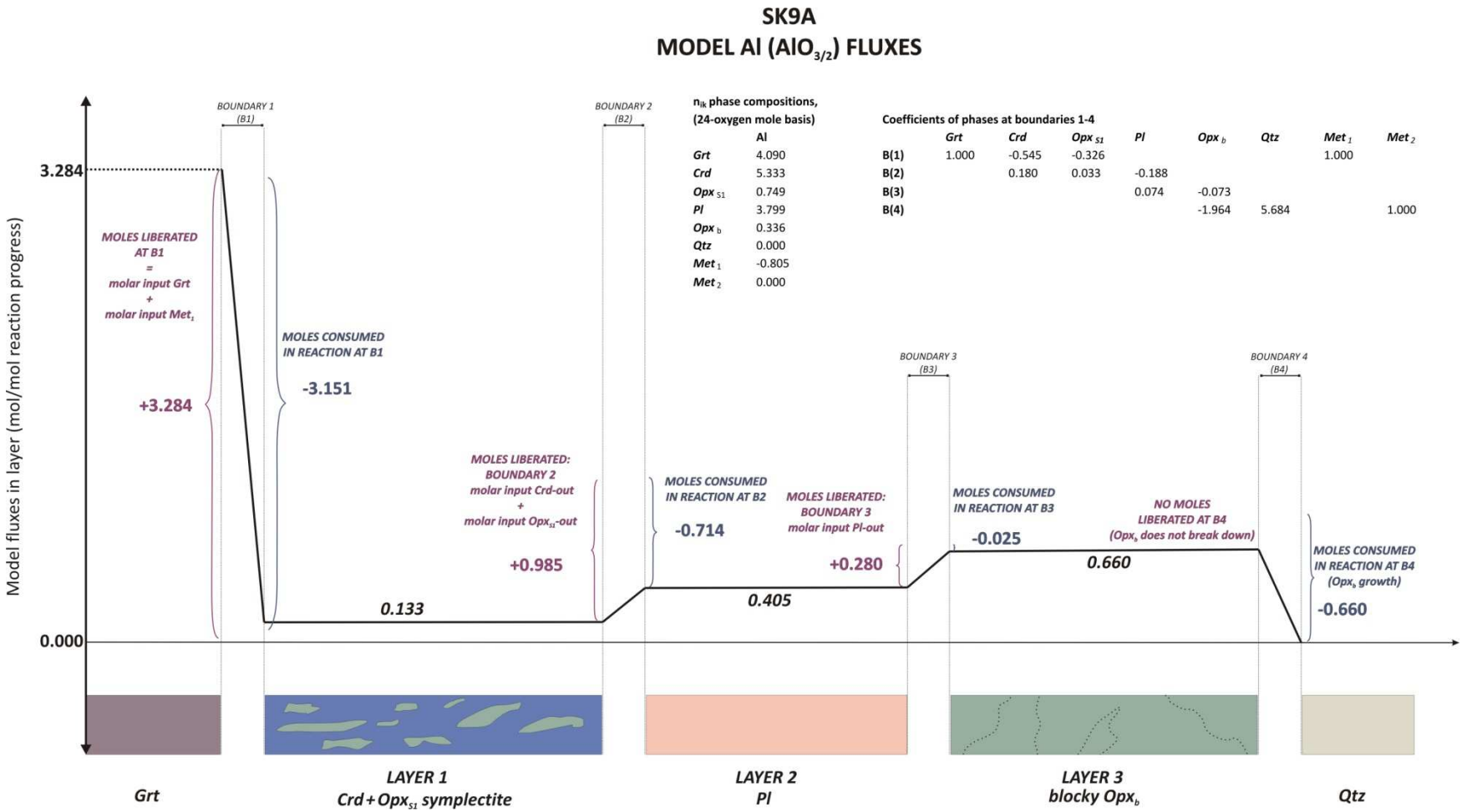

Figure 5.34: Development of positive fluxes for $AlO_{3/2}$ over corona layers in SK9A.

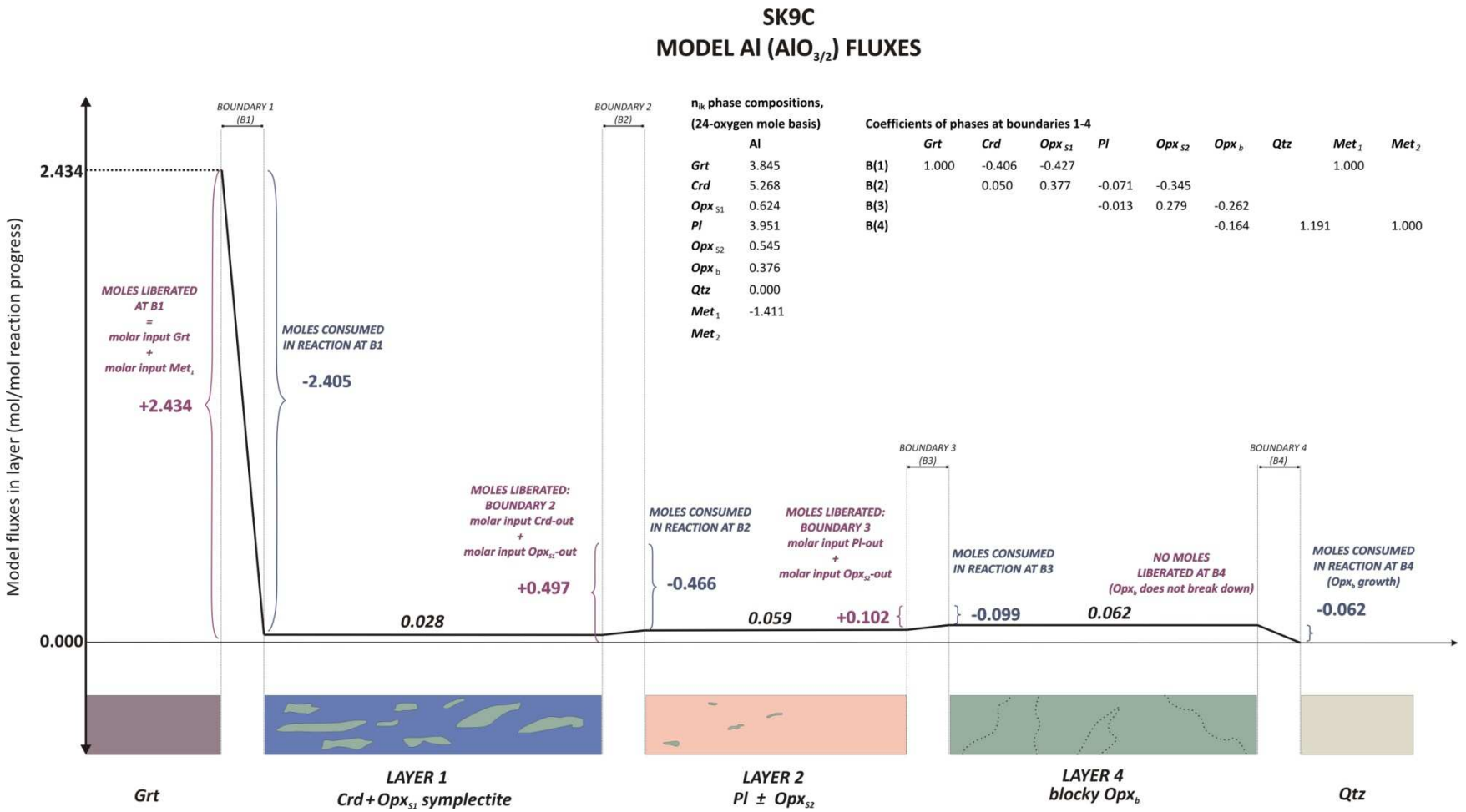

Figure 5.35: Development of positive fluxes for $AlO_{3/2}$ over corona layers in SK9C.

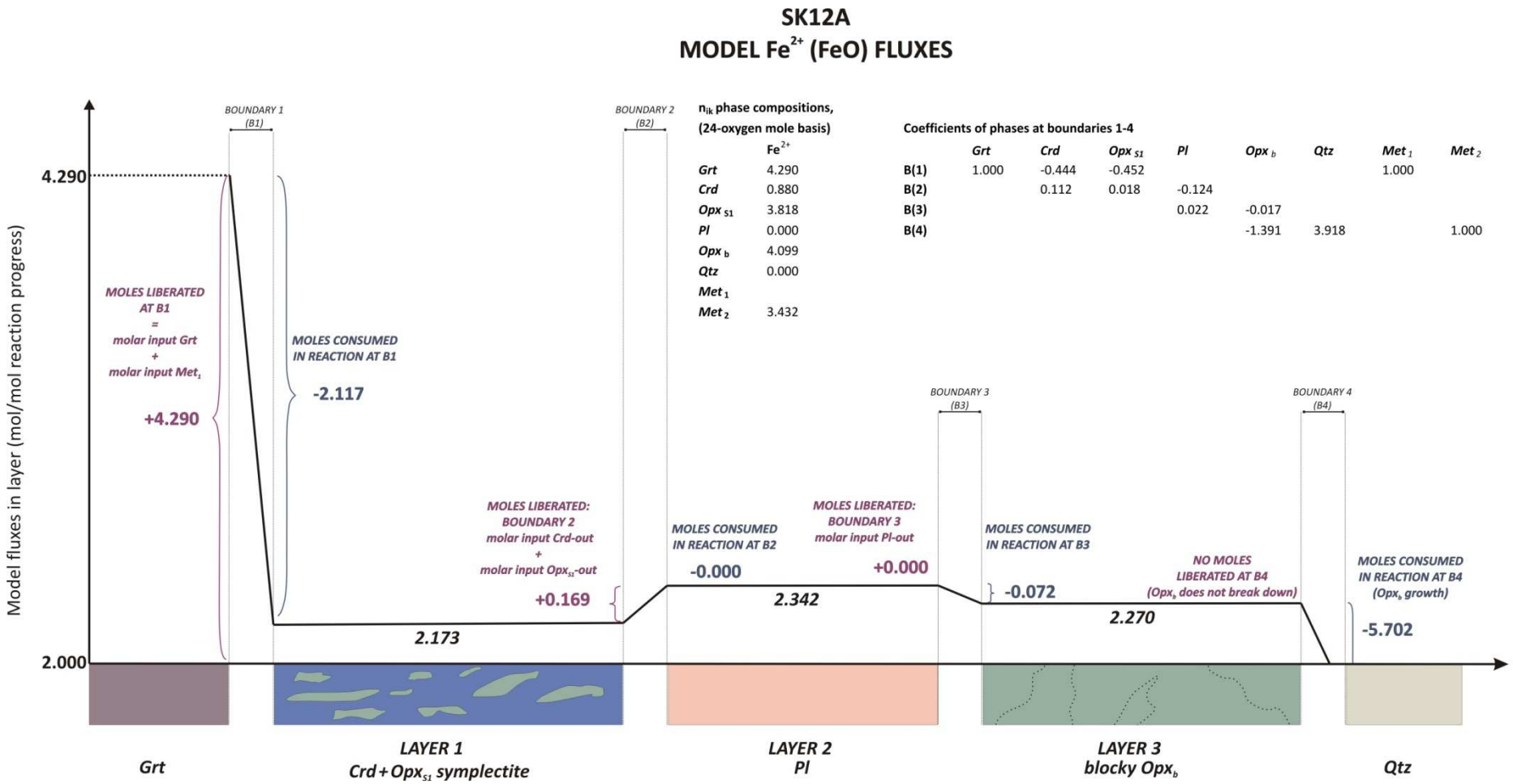

Figure 5.36: Development of positive fluxes for FeO over corona layers in SK12A.

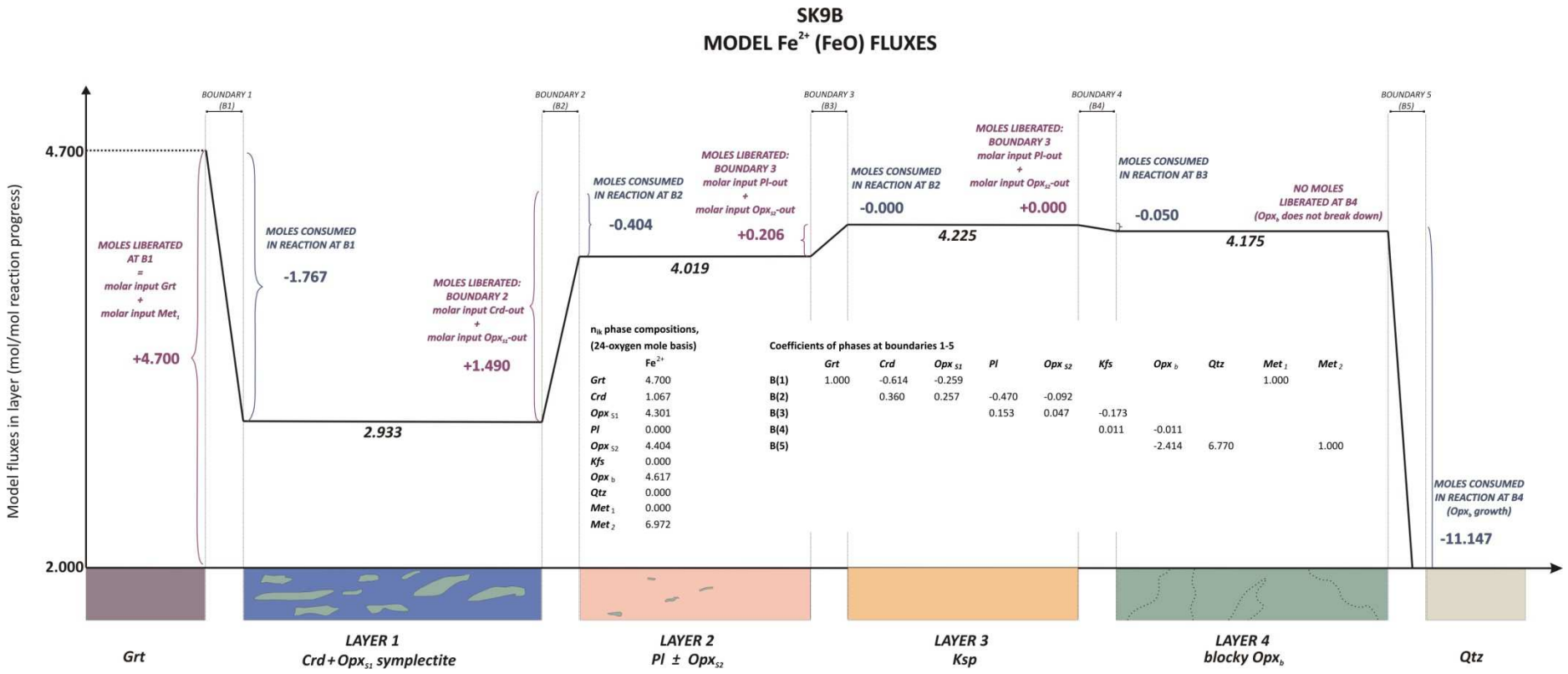

Figure 5.37: Development of positive fluxes for FeO over corona layers in SK9B.

progress (Figure 5.36) and from +2.93 to +4.02 mol per unit reaction progress in SK9B (Figure 5.37). This is owing to the fact that FeO consumed in producing the plagioclase-dominated layer 2 ($n_{Fe}^{2}.\bar{v}^{2} \rightarrow 0$) and K-feldspar layer 3 in SK9B ($n_{Fe}^{3}.\bar{v}^{3} \rightarrow 0$) is negligible compared to the molar FeO liberated at boundary 2 from the decomposition of cordierite and orthopyroxene. The positive inflection is particularly large for SK9B because of the large amounts of cordierite and orthopyroxene consumed at boundary 2 (v_{crd}^{1} = 0.360 and $v_{opx_{s1}}^{1}$= 0.257 compared to v_{crd}^{1}= 0.112 and $v_{opx_{s1}}^{1}$= 0.018 in SK12A). The excess FeO yielded at boundary 2 diffuses through the feldspathic layers toward the FeO sink adjacent to blocky Opx_b. Fe^{2+} flux is suppressed slightly in layer 3 blocky orthopyroxene in SK8C, SK12A, SK9A and SK9C and layer 4 blocky orthopyroxene in SK9B (Figure 5.30c, Table 5.11) since the molar amounts liberated at boundary 3 (boundary 4 for SK9B) for reaction are negligible. Moreover, despite higher concentrations of FeO in blocky orthopyroxene compared to the feldspathic preceding layers, the reaction coefficient for Opx_b at boundary 3 (boundary 4 for SK9B) is typically very small in magnitude, since most Opx_b grows at the boundary with quartz ($n_i^{pl}.v_{pl}^{3} + n_i^{opx_{s2}}.v_{opx_{s2}}^{3} > n_i^{opx_b}.v_{opx_b}^{3} \rightarrow 0$).

The difference in magnitudes of the Fe^{2+} flux between coronas is a function of the composition of reactant and product phases, the effective bulk composition of the corona domain, product proportions, overall reaction coefficients and local reaction coefficients at each layer boundary. Lowest Fe^{2+} fluxes are present in SK9C layer 1 (+1.96 mol), reflecting the large molar amounts of FeO consumed at boundary 1 (-2.37 mol) to yield Fe-rich symplectite phases (Table 5.11). After reaction at boundary 1, less FeO remains in excess to diffuse through the symplectite toward quartz. In contrast to SK9C, the more magnesian symplectite phases in SK8C comprise lower molar amounts of FeO and, thus, less FeO (-1.63 mol) is consumed at boundary 1, with the comparatively greater excess FeO available from garnet breakdown to diffuse through the layer down the chemical potential gradient towards quartz (Figure 5.30c, Table 5.11). Among the coronas studied, SK9B exhibits the highest Fe^{2+} fluxes in all layers, owing to a relatively Fe-rich reactant garnet compounded by low proportions of cordierite and orthopyroxene in the

corona as a whole; consequently, less FeO is consumed in reaction, yielding high molar amounts of excess FeO and, therefore, higher-magnitude positive fluxes (Table 5.11, Figure 5.37).

Fluxes in Mg are generally negative and next highest in magnitude after Fe^{2+} in all coronas (Figure 5.30d, Table 5.11). The negative flux relationships for Mg in SK12A are demonstrated in Figure 5.38 and positive flux relationships for SK9B in Figure 5.39. Negative fluxes for Mg arise in SK8C, SK12A, SK9A and SK9C (Figure 5.30d, Table 5.11) because the reactant garnet composition is deficient in MgO as it evolves to more Fe-rich final steady-state compositions with prolonged reaction duration. Consequently, there is a deficiency in the molar input of MgO from garnet breakdown and metasomatic influx at boundary 1 required to yield product phases of the appropriate composition in observed proportions. This deficiency is accommodated through influx of Mg into MgO-deficient portions of the corona at the quartz boundary and diffusion towards garnet in the opposite direction to FeO, i.e., from left to right (e.g., SK12A, Figure 5.38). In contrast to the other coronas, diffusional stability for SK9B requires metasomatic input of MgO at garnet boundary 1 that exceeds that required to stabilize layer 1 symplectite phases, resulting in a positive flux across the corona (Figure 5.39). The Mg flux in layer 1 symplectite is most negative for SK8C and SK12A (Figure 5.30d), indicative of the more magnesian phase compositions comprising the symplectites in these coronas. Larger molar amounts of MgO are required to stabilise symplectite phases of the appropriate compositions at boundary 1 (+2.62 mol for SK8C and 2.35 mol for SK12A, Table 5.11), thus inducing higher-magnitude Mg fluxes from quartz towards the MgO sink at boundary 1 for generation of symplectite phases. In contrast, symplectite phases are more ferruginous in SK9 coronas; thus, the molar amount of MgO consumed at boundary 1 in production of the symplectite is less than that for SK8C and SK12A (+1.84 mol for SK9A, +1.78 mol for SK9B and +1.89 mol for SK9C). Therefore, despite less molar MgO input at boundary 1 from more Fe-rich garnet reactants (Table 5.11), the negative flux induced in layer 1 in SK9 is less than in SK8C and SK12A (Figure 5.30d).

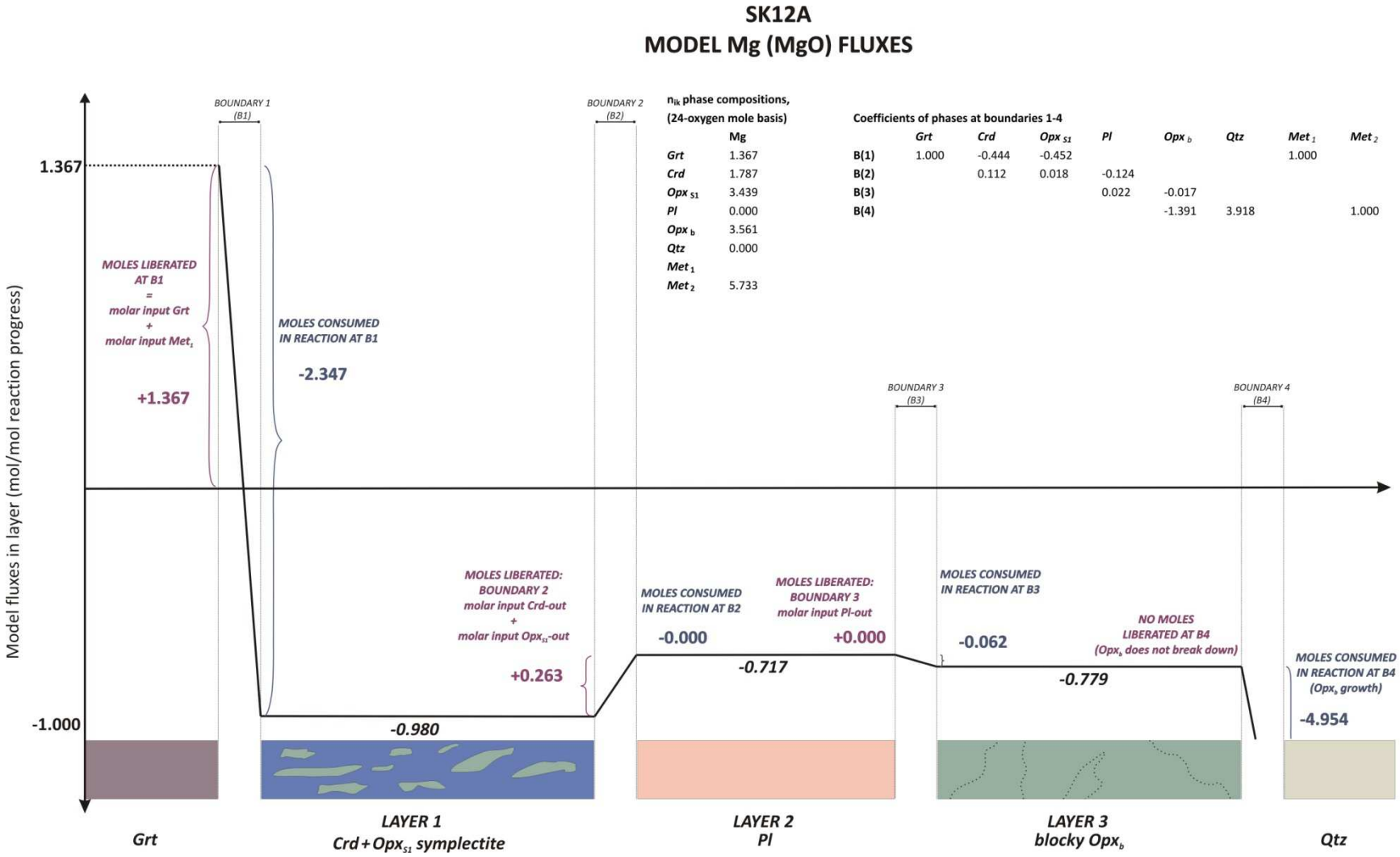

nik phase compositions, (24-oxygen mole basis)

	Mg
Grt	1.367
Crd	1.787
Opx s1	3.439
Pl	0.000
Opx b	3.561
Qtz	0.000
Met 1	
Met 2	5.733

Coefficients of phases at boundaries 1-4

	Grt	Crd	Opx s1	Pl	Opx b	Qtz	Met 1	Met 2
B(1)	1.000	-0.444	-0.452				1.000	
B(2)		0.112	0.018	-0.124				
B(3)				0.022	-0.017			
B(4)					-1.391	3.918		1.000

Figure 5.38: Development of negative fluxes for MgO over corona layers in SK12A.

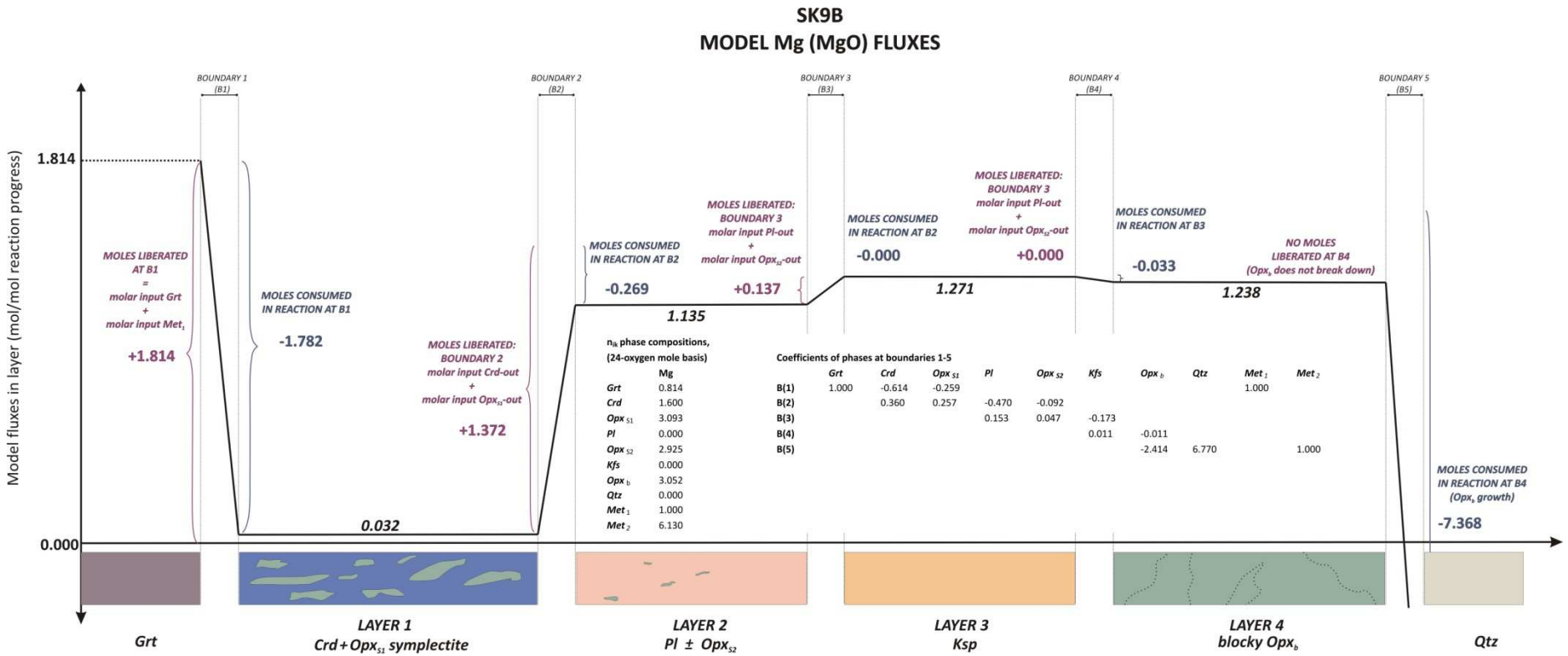

Figure 5.39: Development of negative fluxes for MgO over corona layers in SK9B.

The reduction in negative Mg flux in plagioclase-dominated layer 2 in all coronas (Figure 5.30d) and K-feldspar layer 3 in SK9B (Figures 5.30d and 5.39) reflects the absence of MgO in plagioclase, i.e., the molar amount of MgO consumed in reaction at boundary 2 approaches zero ($n_{Mg}^{pl}.v_{pl}^{2} \rightarrow 0$). The liberation of MgO from the breakdown of cordierite and orthopyroxene at boundary 2 further mitigates the negative Mg flux required from quartz at boundary 4 through layer 2. In SK9B, the amount of MgO liberated by cordierite and orthopyroxene breakdown is large enough (+1.37 mol) with only 0.27 moles consumed in the production of layer 2 orthopyroxene to yield the highest-magnitude positive flux (+1.14 mol) across layer 2 (Figure 5.39). Similarly, the negative flux in layer 1 is reduced in SK8C layer 2 (-0.50 mol) compared to SK12A (-0.72 mol) and SK9A (-0.57 mol) owing to the large molar amounts of MgO liberated at boundary 2 in SK8C with the breakdown of comparatively magnesian symplectite phases compared to SK12A and SK9A (Figure 5.30d, Table 5.11). In SK9C, large molar amounts of MgO are liberated at boundary 2 (+1.18 mol), however a large molar input is required to produce high modes of orthopyroxene (Opx_{S2}) in layer 2 (-1.00 mol), thereby preventing any reduction in negative MgO flux across layer 2 (Figure 5.30d, Table 5.11). The Mg flux in blocky orthopyroxene for layer 3 in SK8C, SK12A, SK9A and SK9C increases in magnitude slightly to accommodate the higher molar amounts of MgO consumed in reaction at boundary 3 to yield blocky orthopyroxene (Figure 5.30d, Figure 5.38). The small reaction coefficient at boundary 3 for Opx_b (~0.01, Tables 5.5-5.9) suppresses a large negative increase in magnitude since only a small amount of MgO is consumed despite relatively high concentrations of MgO in blocky Opx_b ($n_{Mg}^{opx_b}.v_{opx_b}^{3}$ = -0.062 in SK12A). Similarly, the positive flux of MgO in layer 4 blocky orthopyroxene in SK9B is suppressed to slightly less positive values by the same conditions (Figure 5.39.)

Variation in Ca flux for all coronas is shown in Figure 5.30e. Contrasting Ca flux relationships are demonstrated for SK9B and SK12A in Figure 5.40 and Figure 5.41. Large positive fluxes in layer 1 are due to metasomatic input at boundary 1 and molar input from reactant garnet decomposition. Little or no CaO is consumed in producing layer 1 symplectite phases and so flux remains essentially unchanged in

layer 1 from molar input at boundary 1 (Figure 5.30e). Fluxes in all coronas exhibit a reduction over layer 2 owing to consumption of CaO to form plagioclase (Figure 5.30e), enough to induce a negative flux in all coronas except SK12A (Figure 5.40). Liberation of CaO at boundary 3 with the breakdown of plagioclase and negligible consumption of CaO to form K-feldspar in SK9B (Figure 5.41) and blocky Opx_b in other coronas (e.g., SK12A in Figure 5.40) re-establishes positive flux of CaO in all coronas. Flux is initially highest in SK9B layer 1 relative to other coronas (Figure 5.30e), followed by the largest negative inflection in flux over layer 2, reflecting highest molar input at boundary 1 (+0.407 mol), followed by the largest molar CaO consumption at boundary 2 (-0.532 mol) in forming plagioclase in greater overall proportions than in any of the other coronas. The variation in Ca flux magnitude in other coronas over layer 2 reflects varying metasomatic input at boundary 1, compounded by different reaction coefficients for plagioclase of different compositions at boundary 2 (e.g., SK12A, Figure 5.40). The highest positive Ca flux occurs in SK12A (0.010 mol) and principally reflects a high metasomatic input at boundary 1 (0.168 mol) compared to metasomatic fluxes of 0.155 mol in SK8C and 0.168 mol in SK9A. This is further compounded by a small reaction coefficient for plagioclase at boundary 2 (-0.12 for SK12A) compared to reaction coefficients of -0.20 and -0.19 for SK8C and SK9A, respectively. In other words, the molar amount of CaO consumed in layer 2 in SK12A is less than that for SK8C and SK9A, with a greater initial input of CaO available for reaction, thereby yielding larger amounts of excess or unreacted CaO to diffuse through the layer down the chemical potential gradient toward boundary 3.

Fluxes for Na exhibit a V-shaped trend across all coronas (Table 5.11, Figure 5.30f). Contrasting flux relationships for Na in SK12A and SK9B are demonstrated in Figures 5.42 and 5.43, respectively. Large-magnitude positive fluxes are observed over layer 1 since no $NaO_{1/2}$ is consumed in the production of symplectite phases (Figure 5.30f). Na flux magnitudes in layer 1 reflect varying metasomatic input of $NaO_{1/2}$ at boundary 1 into the corona (Table 5.11). Na fluxes in layer 1 are highest in magnitude in SK9B (0.694 mol) owing to the large molar amounts of this component required to stabilize the high overall proportion of plagioclase and K-feldspar in this corona (Figure 5.43). Large flux inflections occur at boundary 2 with

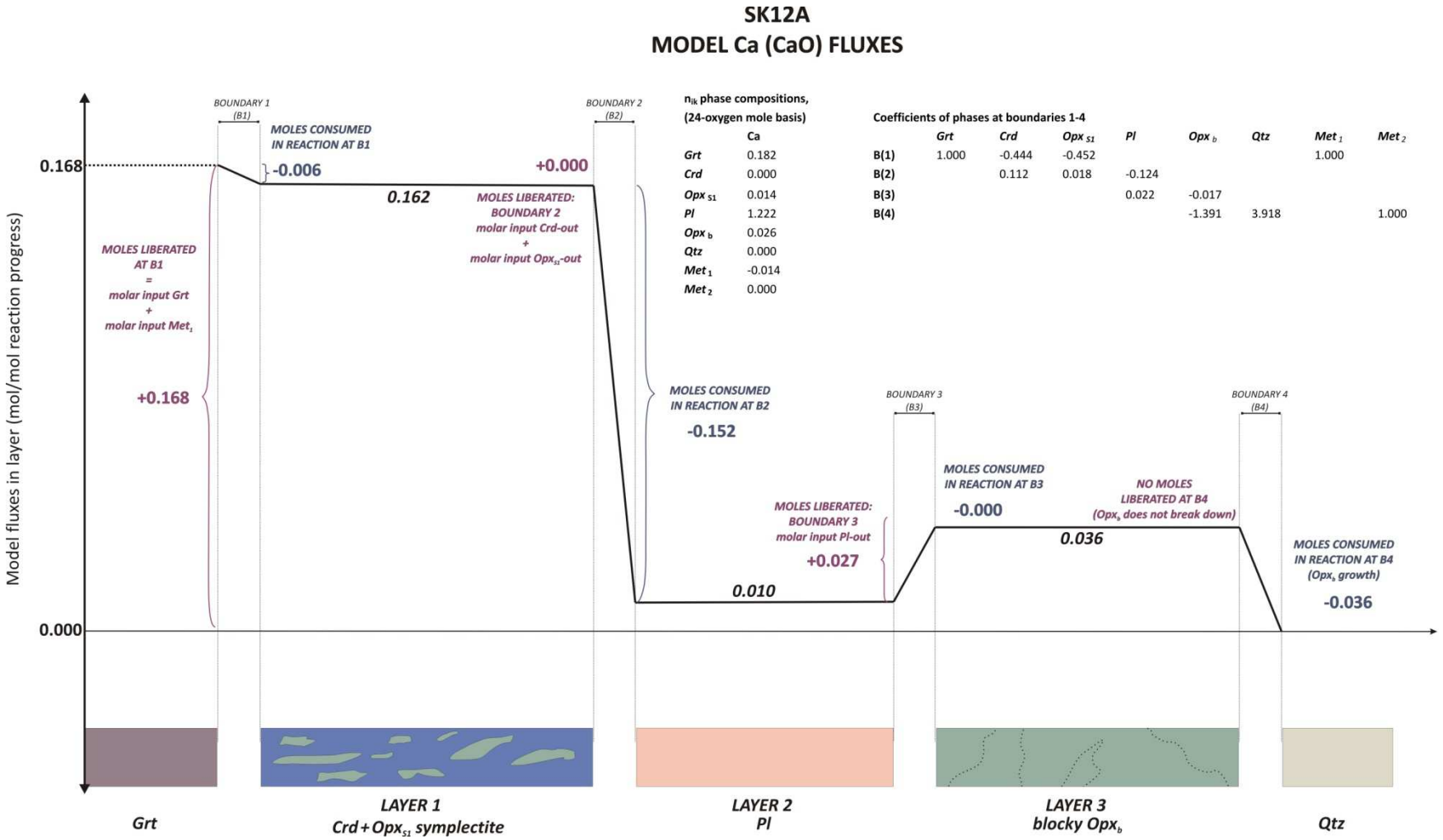

Figure 5.40: Development of fluxes for CaO over corona layers in SK12A.

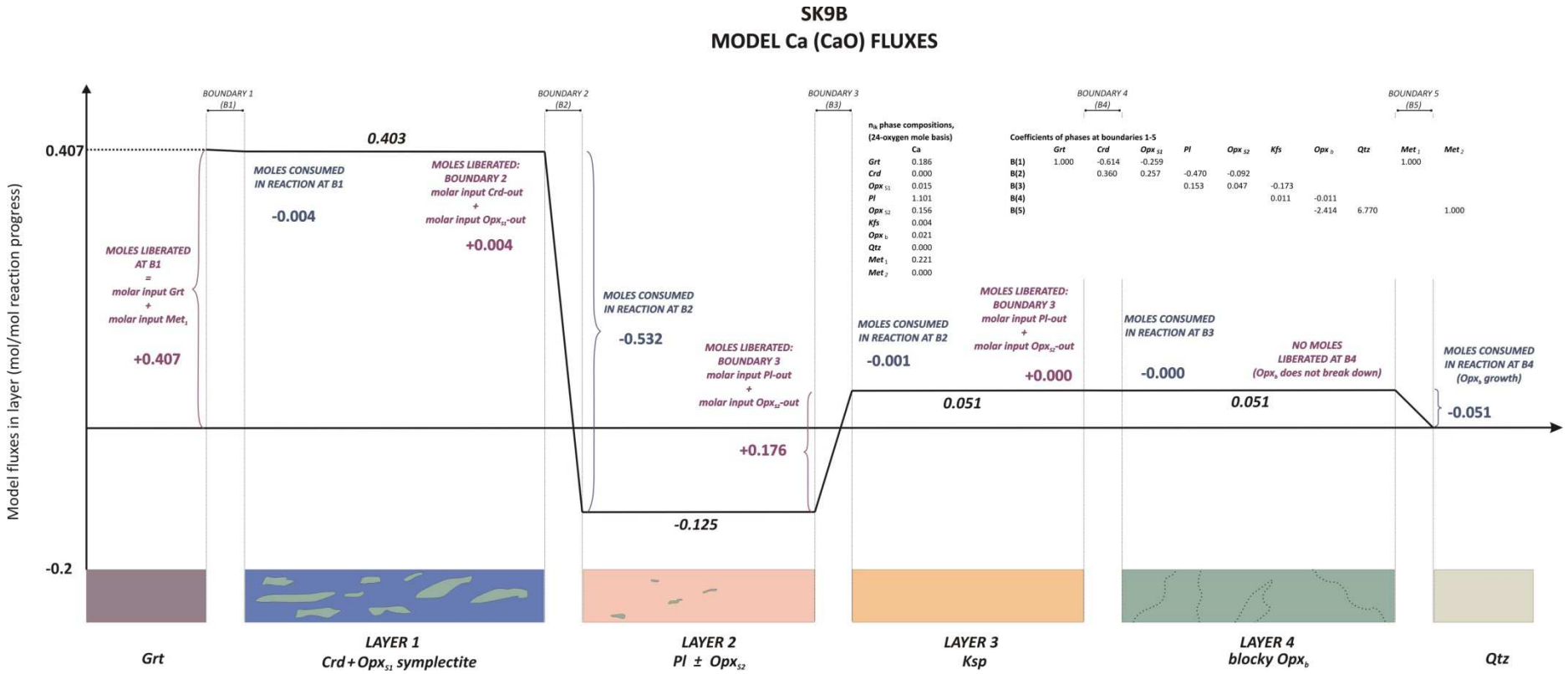

Figure 5.41: Development of fluxes for CaO over corona layers in SK9B.

the production of plagioclase-bearing layer 2 (Figure 5.30f). Flux magnitudes in layer 2 reflect the relative difference in $NaO_{1/2}$ metasomatic input at boundary 1 and the requisite amounts of $NaO_{1/2}$ consumed in producing plagioclase of the correct composition in the observed mode. The amount of $NaO_{1/2}$ consumed to produce plagioclase of the observed proportion and composition is greater than the Na flux in layer 1, i.e., molar $NaO_{1/2}$ available for reaction at boundary 2, thereby inducing negative Na fluxes in layer 2 of all coronas (except SK9C) in the opposite direction (i.e., towards garnet). The largest negative inflection occurs in SK9B at boundary 2 (-0.181 mol), and is due to the large amounts of $NaO_{1/2}$ consumed to produce high modes of plagioclase (Figure 5.43). Large negative fluxes in layer 2 in SK8C (-0.101 mol) and SK9A (-0.150 mol) reflect enrichment in X_{Ab} (0.75 and 0.65 in SK8C and SK9A, respectively) and higher overall modes of layer 2 plagioclase compared to SK9C and SK12A (Table, 5.11, Figure 5.30f). The molar $NaO_{1/2}$ liberated with the decomposition of plagioclase at boundary 3, with lesser $NaO_{1/2}$ consumed in the production of K-feldspar layer 3 in SK9B (Figure 5.43) and negligible $NaO_{1/2}$ in blocky Opx_b in SK12A (Figure 5.42), SK9A and SK9C, suppresses negative Na fluxes substantially in these layers.

The magnitude of K flux is only significant in SK9B (Table 5.11, Figure 5.30g, Figure 5.44) where the K-feldspar layer 3 is present. $KO_{1/2}$ input into the corona occurs through metasomatic input at boundary 1 (+0.383 mol). Flux remains essentially unchanged through layer 1 (+0.383 mol) and layer 2 (+0.379 mol), as negligible $KO_{1/2}$ is consumed in producing phases comprising layers 1 and 2. Molar $KO_{1/2}$ consumed in the production of layer 3 K-feldspar exceeds fluxes in layer 1 and 2 and induces nett diffusion of $KO_{1/2}$ (negative flux) in the opposite direction from quartz towards garnet in layer 3 (-0.025 mol). With negligible molar $KO_{1/2}$ consumed to produce blocky Opx_b at boundary 4, decomposition of K-feldspar reduces negative K flux to zero over layer 4 (Figure 5.44).

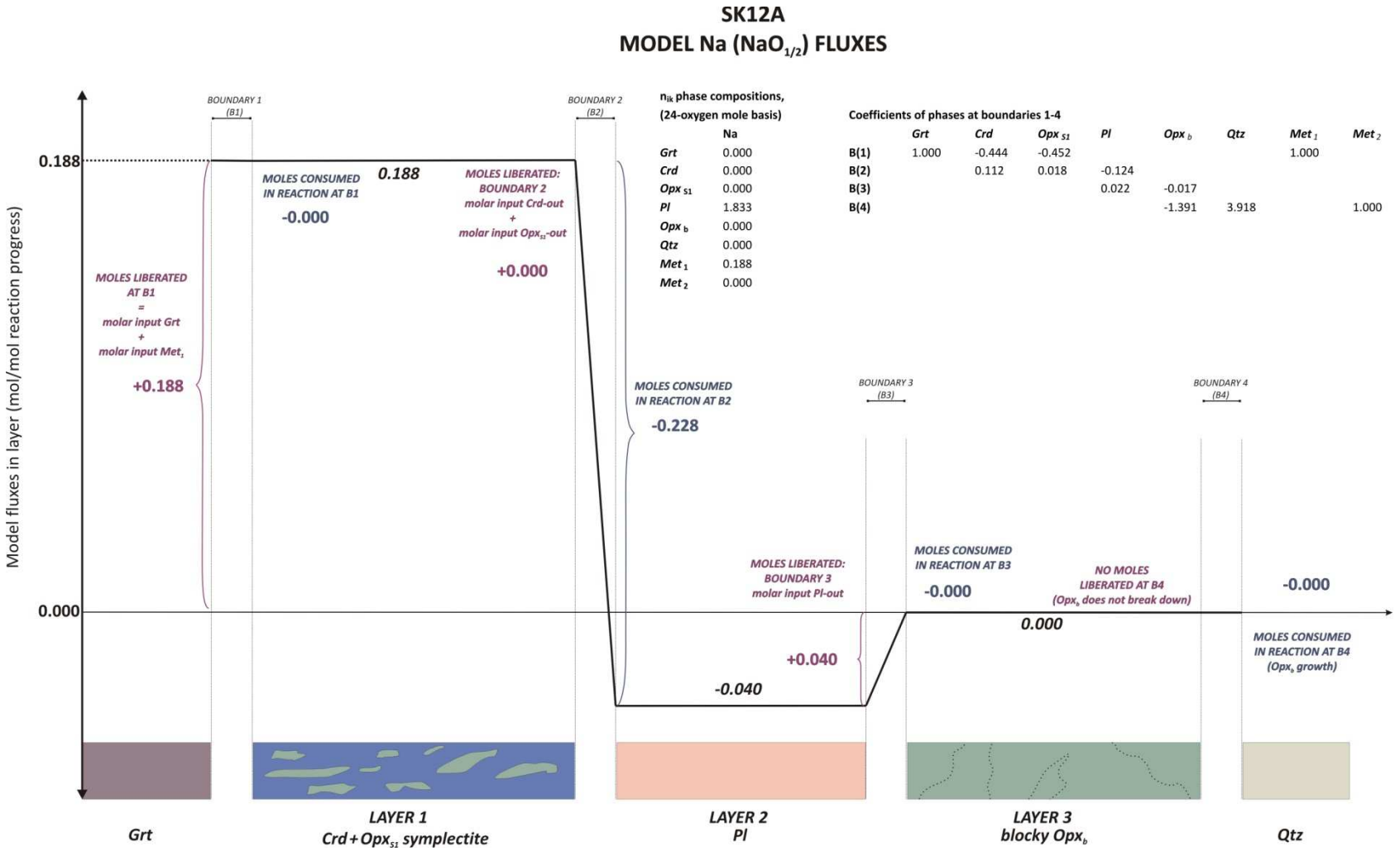

Figure 5.42: Development of fluxes for $NaO_{1/2}$ over corona layers in SK12A.

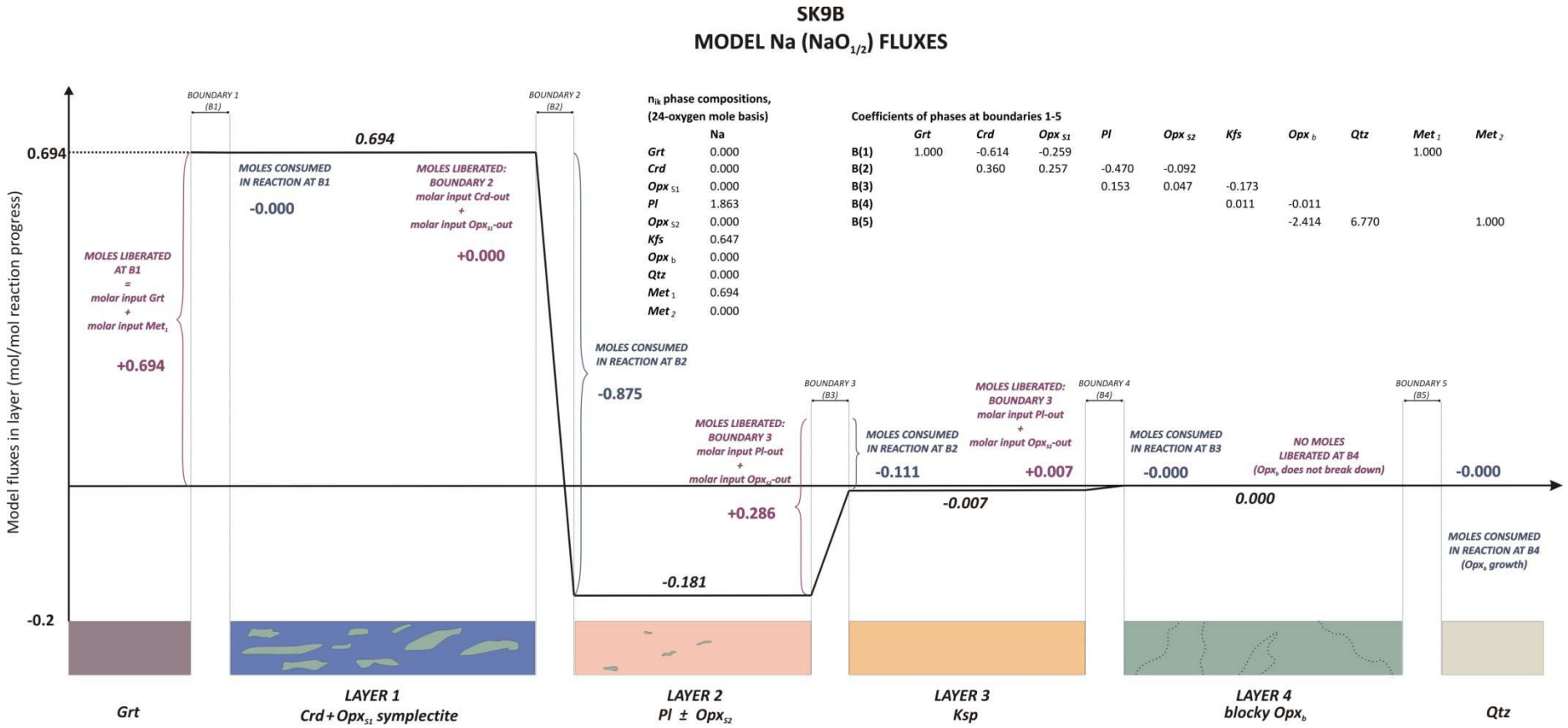

n_{ik} phase compositions, (24-oxygen mole basis)

	Na
Grt	0.000
Crd	0.000
Opx $_{s1}$	0.000
Pl	1.863
Opx $_{s2}$	0.000
Kfs	0.647
Opx $_b$	0.000
Qtz	0.000
Met $_1$	0.694
Met $_2$	0.000

Coefficients of phases at boundaries 1-5

	Grt	Crd	Opx $_{s1}$	Pl	Opx $_{s2}$	Kfs	Opx $_b$	Qtz	Met $_1$	Met $_2$
B(1)	1.000	-0.614	-0.259						1.000	
B(2)		0.360	0.257	-0.470	-0.092					
B(3)				0.153	0.047	-0.173				
B(4)						0.011	-0.011			
B(5)							-2.414	6.770		1.000

Figure 5.43: Development of fluxes for $NaO_{1/2}$ over corona layers in SK9B.

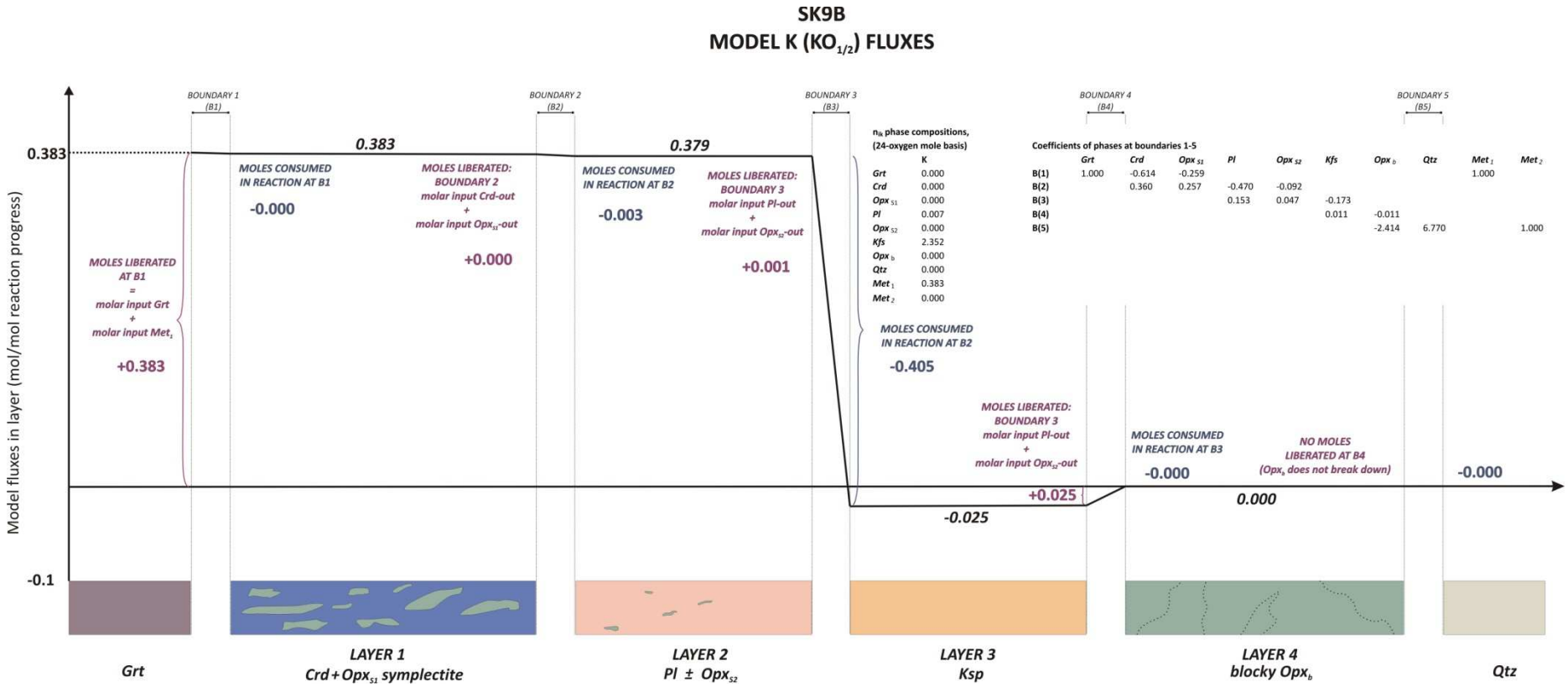

Figure 5.44: Development of fluxes for $KO_{1/2}$ over corona layers in SK9B.

5.3.5 Chemical potential gradients

The study of corona textures is predicated on the concept of local equilibrium (Thompson, 1959, 1970; Korzhinskii, 1959). Local equilibrium is attained in any corona system when the chemical potential differences between phases at any point in a corona are equalized, i.e., chemical potential gradients approach zero for all components in all phases (White et al., 2008, Chapter 3, Chapter 6). Early studies on the evolution of corona textures as a consequence of evolving chemical potential gradients began with the seminal work by Thompson (1959, 1970) and Korzhinskii (1959). Fisher (1973, 1977) and Joesten (1977) formalised the mathematical treatment of chemical potentials in coronas through the development and application of non-equilibrium thermodynamics to corona modelling. Accordingly, it is possible to reconstruct the prevailing chemical potential gradients between local equilibria across a corona and assess the extent of equilibration attained (Appendix A).

The chemical potential gradient for a component in each layer is given by the diffusion equation, with phenomenological diffusion coefficients relative to Si used in the absence of absolute diffusion coefficients:

$$\left(\frac{d\mu_i}{dx}\right)^{q*} = -\frac{L_{SiSi}}{L_{ii}} J_i^{q*} \qquad eqn\ 5.3$$

Chemical potential gradients reflect the coupled relationship between component flux and rate of diffusion and manifest as a concentration gradient for the component, *i*. Chemical potential relationships across a growing corona layer are most easily demonstrated in the binary system between components 1 and 2 in Figure 5.45. Variable intergranular diffusivities (particularly between Al, Fe and Mg) partition the system into two distinct, transient, compositional domains, A and B, which are in local equilibrium with unique chemical potentials. The gradient in chemical potentials between A and B drives diffusion in the corona from A to B for component 1 so as to equalize chemical potentials and attain equilibrium. The larger the chemical potential gradient, the more material is needed to diffuse down the chemical potential gradient more rapidly in order for equilibration to occur.

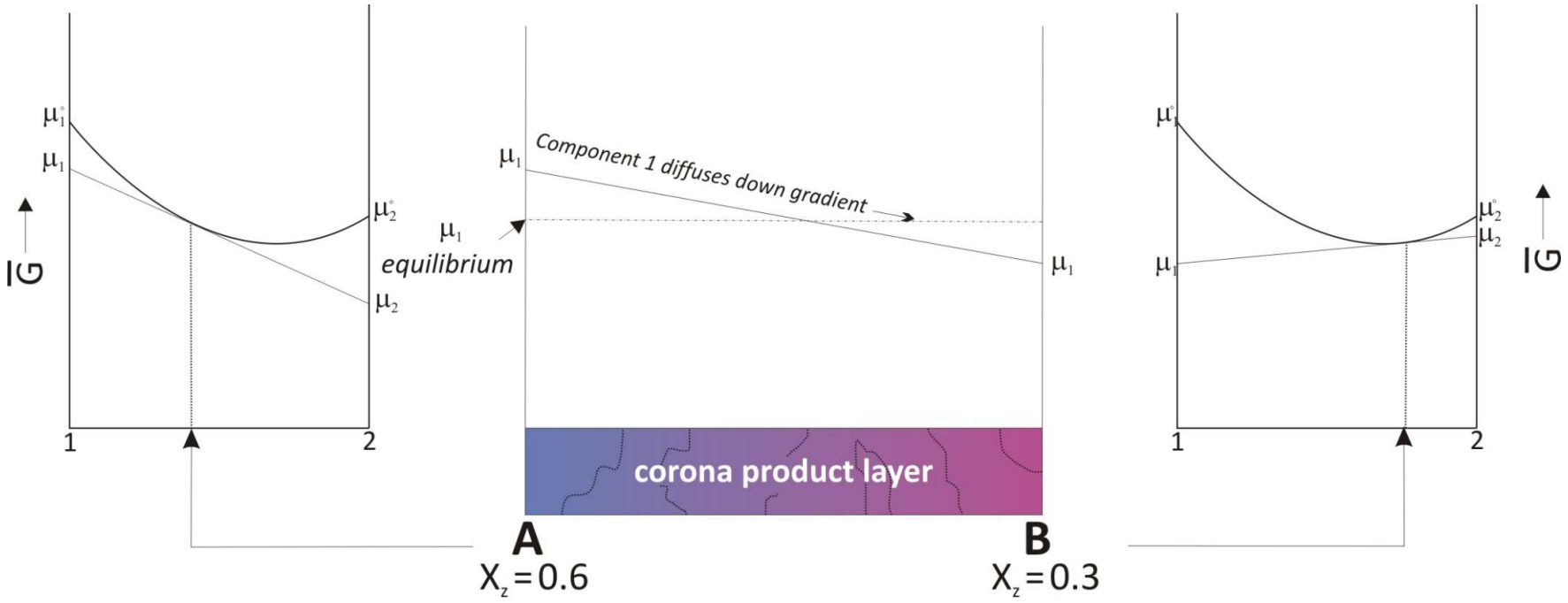

Figure 5.45: Schematic plot demonstrating the nature of chemical potential gradients during growth of a corona layer. The mole fraction of mineral endmember z ranges from X = 0.6 to X = 0.3 across the corona from A to B, reflecting a difference in chemical potentials in both component 1 and 2. For clarity the chemical potential relationships for only component 1 are demonstrated. The gradient in chemical potentials from A to B drives diffusion of component 1 down the chemical potential gradient to B to equalize potentials. Chemical potentials at A and B shift to reflect changing local bulk composition as diffusion depletes component 1 at A and enriches component 1 at B. Diffusion ceases when the chemical potentials at A and B reach the equilibrium value.

Components with the greatest chemical potential differences are those where $\frac{L_{SiSi}}{L_{ii}}$ is largest, i.e., the component diffuses slowly relative to Si, and where the concentration gradient and, thus, component flux (J_i^{q*}), is highest across a corona. Model chemical potential gradients for each component in each corona from the Steynskraal granulites are presented in Figures 5.46 and 5.47. Highest-magnitude chemical potential gradients are observed for Al in all layers in all coronas, consistent with intermediate to high component fluxes and the fact that Al diffuses most slowly relative to Si ($L_{SiSi}/L_{AlAl} \geq 1$ and highest in magnitude) compared to other components. The steady increase in magnitude of Al chemical potential gradients from layer 1 to layer 3 (Figures 5.46a-e and 5.47b) reflects the increasing magnitude of Al flux across these layers while L_{SiSi}/L_{AlAl} remains constant. Fe^{2+} chemical potential gradients are next highest in magnitude (Figures 5.46a-e and 5.47c). This is attributed to the large fluxes of FeO in all layers from all coronas, up to two orders of magnitude larger than the lowest flux components in a corona (Na, K in Figure 5.30), despite the very small L-ratios for Fe^{2+} compared to other components in all coronas (as low as 0.024 in SK9C) (see Figure 5.26, Table 5.5-5.9). Si chemical potential gradients are next highest in magnitude (Figures 5.46a-e and 5.47a). They are unchanged in magnitude from Si fluxes since $L_{SiSi}/L_{SiSi} = 1$. Mg chemical potential gradients are marginally smaller in magnitude than Si in general, owing to the very small L-ratio (only Fe diffuses more rapidly) coupled with intermediate magnitude fluxes (Figures 5.46a-e and 5.47d). Chemical potential gradients for Ca, Na and K are comparatively much smaller than for Si, Al, Fe and Mg (Figures 5.46a-e and 5.47e-g), reflecting their lower flux magnitudes through all layers and L-ratios that are all ≤1 (Figure 5.30e-g).

In general, chemical potential gradients are highest in magnitude in SK8C for SiO_2, $AlO_{3/2}$, FeO and MgO components in all layers compared to all other coronas (Figure 5.46a). The only exception is the SiO_2 chemical potential gradient in layer 1 and MgO gradient in layer 2, where SK12A exhibits larger-magnitude chemical potential gradients (Figure 5.46b). This is consistent with the larger induced Si fluxes in SK12A layers needed to accommodate the high modes of orthopyroxene in the symplectite (see flux modelling Section 5.3.4).

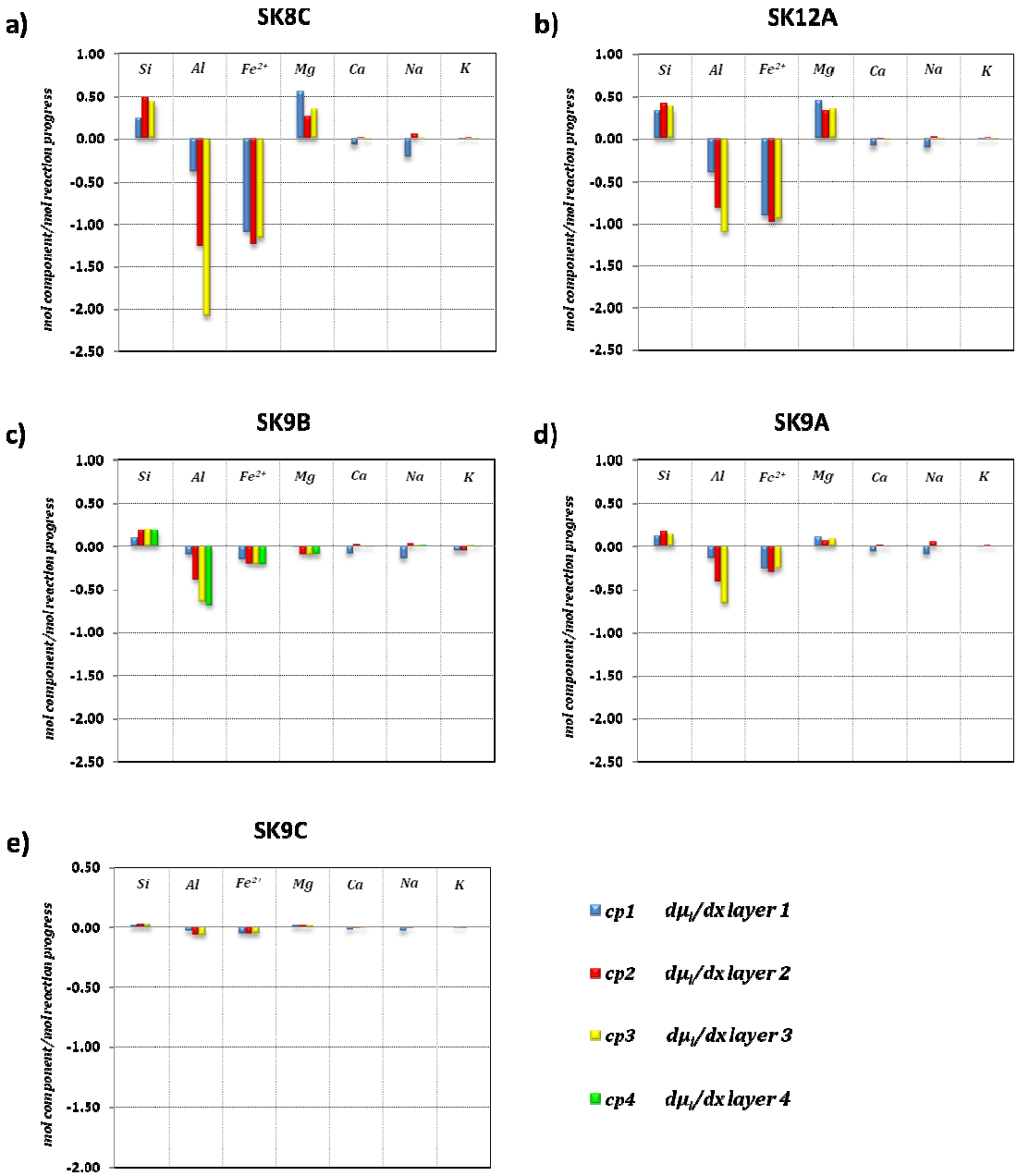

Figure 5.46: Model chemical potential gradients for components in coronas SK8C, SK12A, SK9A, SK9B and SK9C. Calculation methodology is shown in Appendix A.

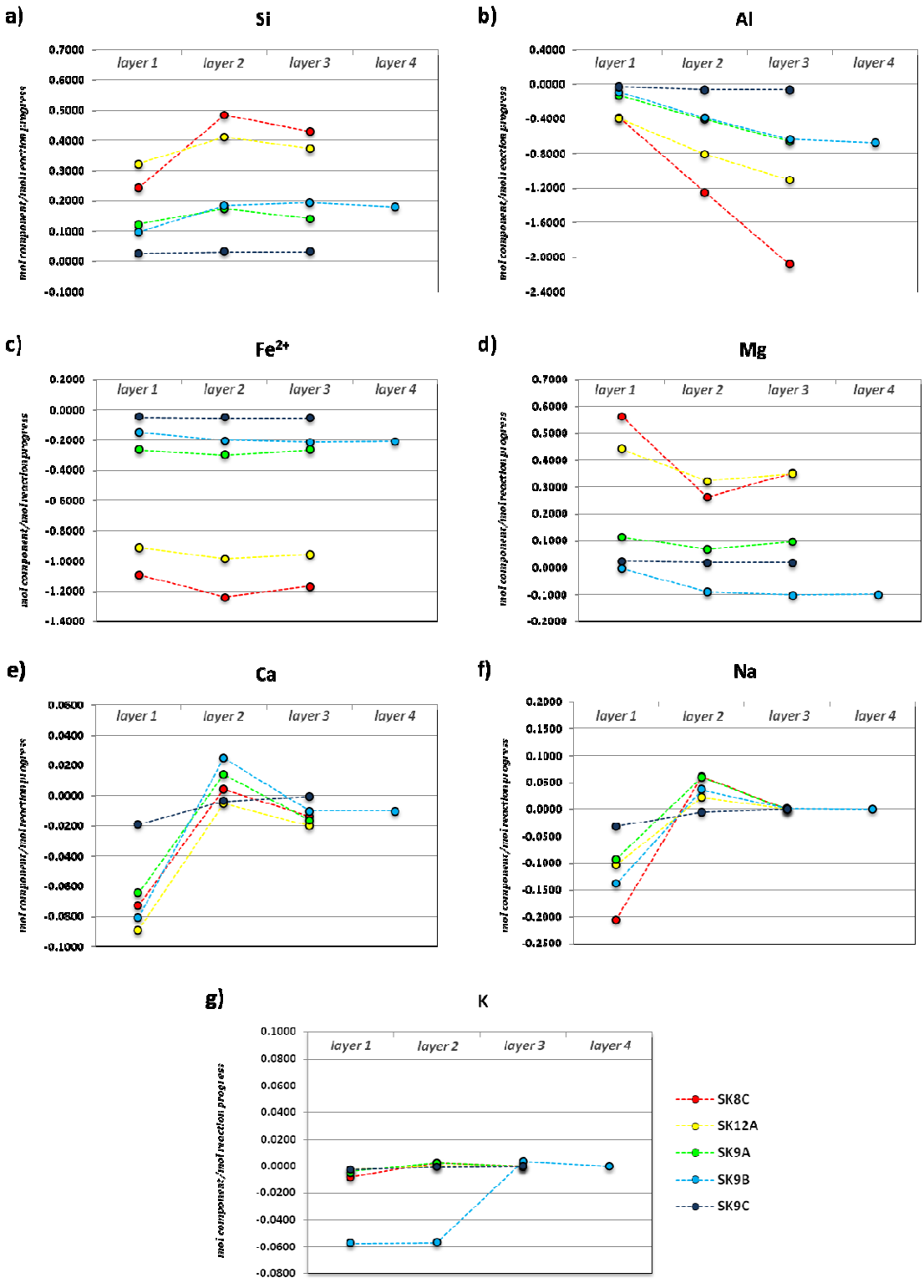

Figure 5.47: Model chemical potential gradients for components in coronas SK8C, SK12A, SK9A, SK9B and SK9C.

Following SK8C, the SK12A model chemical potential gradients are next highest in magnitude for the four major components SiO_2, $AlO_{3/2}$, FeO and MgO. Chemical potential gradients for SK9B and SK9A are slightly lower in magnitude but tend to overlap to an extent in chemical potential space (Figure 5.46c, d). Chemical potential gradients in SK9C appear to have been reduced most effectively with rapid diffusion (Figure 5.46e), consistent with high modelled L-ratios (see Section 5.3.2) and low component fluxes through all layers for this corona (see Section 5.3.4).

Figure 5.48 demonstrates the relationships between positive component flux, molar content of component *i* and negative chemical potential gradients. Negative chemical potential gradients are coupled with positive fluxes in layers and component diffusion from garnet toward quartz (e.g., $AlO_{3/2}$, FeO). Negative chemical potential gradients increasing in magnitude indicate progressively larger fluxes of component *i* diffusing comparatively more slowly ($L_{SiSi}/L_{ii} > 1$) towards quartz, e.g., $AlO_{3/2}$ in all layers (case (a) in Figure 5.48). Negative chemical potential gradients decreasing in magnitude (e.g., FeO chemical potential gradients in layer 2 and layer 3) are associated with progressively smaller fluxes or molar amounts of component *i* diffusing comparatively rapidly ($L_{SiSi}/L_{ii} << 1$) through layers towards quartz to equalise chemical potentials, e.g., FeO in feldspathic layer 2 and blocky Opx layers (case (b) in Figure 5.48).

Positive chemical potential gradients are generated with diffusion from quartz toward garnet (Figure 5.49). Positive, decreasing, chemical potential gradients are associated with diminishing negative fluxes in layers and rapid diffusion, e.g., Mg in layer 1 and 2 in all coronas (case (a), Figure 5.49). Conversely, positive increasing chemical potential gradients are consistent with relatively slow component diffusion and increasing negative flux magnitudes, e.g., SiO_2 in layer 1 and 2 in all coronas (case (b), Figure 5.49).

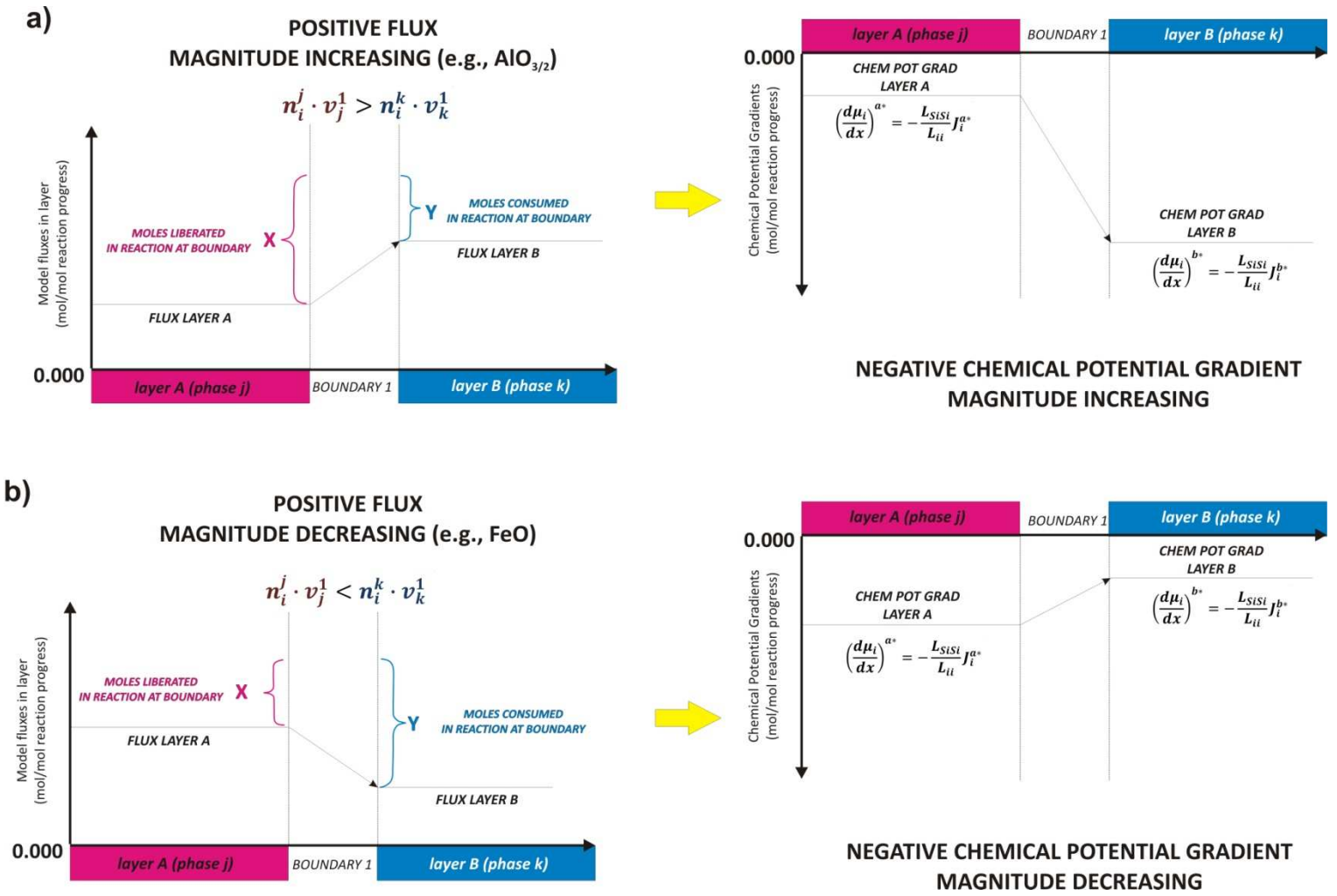

Figure 5.48: The relationship between positive component flux, molar content of component i and negative chemical potential gradients. Details are discussed in the text.

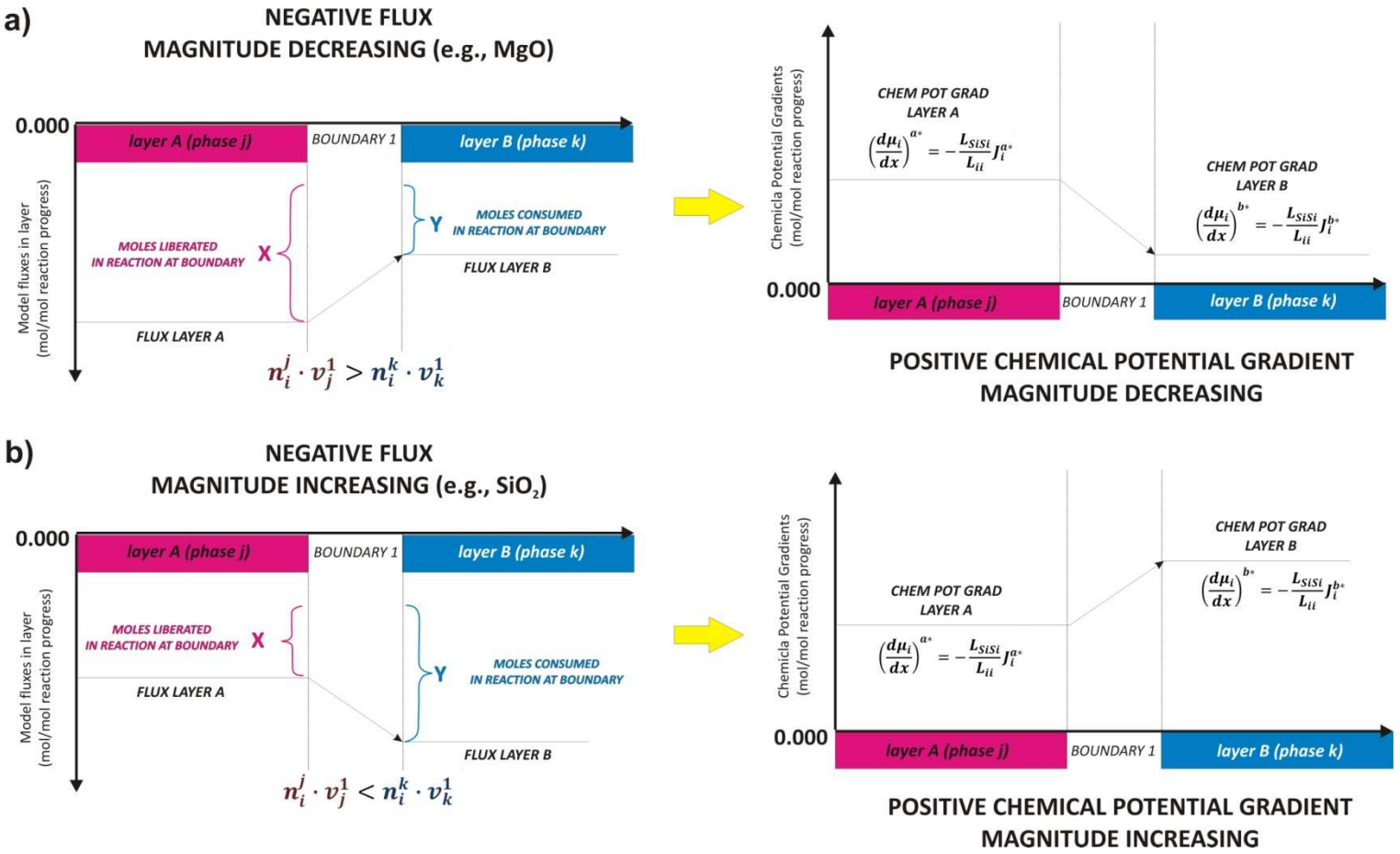

Figure 5.49: The relationship between negative component flux, molar content of component i and positive chemical potential gradients. Details are discussed in the text.

5.3.6 Chemical potential relationships and corona structure

Qualitative chemical potential (μ-μ) plots may be used to augment model chemical potential relationships to assist in characterizing the distribution of layers in the coronas and compositional zonation within corona phases (Joesten, 1977, White et al., 2008). The simplest chemical system to account for corona development is NCFAS ($NaO_{1/2}$-CaO-FeO-$AlO_{3/2}$-SiO_2). Figure 5.50 (inset c) is a qualitative $\mu_{FeO} - \mu_{SiO_2}$diagram in which $\mu_{AlO_{3/2}}$, $\mu_{NaO_{1/2}}$ and μ_{CaO} are passive variables and vary across the diagram according to Gibbs-Duhem relationships (White et al., 2004; White et al., 2008). The method employed in generating the diagram is based on the approach derived by Korzhinskii (1959) and employed by White et al. (2004) and White et al. (2008). The angular relationships between reaction lines on the μ-μ plot were obtained from an orthogonal compatibility diagram for $FeO/AlO_{3/2}$ and $SiO_2/AlO_{3/2}$ immediately prior to reaction (inset a, Figure 5.50) and post-reaction (inset b, Figure 5.50) as in White et al. (2008). Lines in the μ-μ plot are orthogonal to tie lines in the compatibility diagrams (Korzhinskii, 1959). Single-phase fields in the compatibility diagrams (Figure 5.50a, b) occur as fields in the μ-μ plot, tie-lines as reaction lines and tie triangles as intersection points (White et al., 2008, Figure 5.50c). Only the topology of the μ-μ plots can be generated by this method, i.e., the relative positions of the two μ-μ plots in Figure 5.50c cannot be established in *P–T* space. However, White et al. (2008) demonstrated that the possible relative positions of the two μ-μ plots can be inferred since only a very limited relative topological array of μ-μ plots accommodates the textural relationships observed in coronas.

In the Steynskraal granulite coronas, the pre-impact, high-pressure and low-temperature chemical potential relationships are shown in grey in Figure 5.50a and the post-impact low-pressure, high-temperature chemical potential relationships are shown in black in Figure 5.50b. Stable equilibrium chemical potentials for the post-impact assemblage cordierite+plagioclase+orthopyroxene are represented by the black circle. The relative position of pre-impact and post-impact topologies is that required to generate the requisite corona mineralogy in the observed spatial sequence from Crd→Pl→Opx under prevailing chemical potential gradients. Variable intergranular diffusivities for major components and different length scales

of diffusion partition the incipient corona into two compositions and metastable equilibria, i.e., metastable garnet-quartz on the pre-impact portion of μ-μ space at the garnet contact (black triangle) and metastable orthopyroxene-quartz in the post-impact μ-μ space (black square) at the quartz contact, each in local equilibrium with unique chemical potentials, between which chemical potential gradients exist (grey field). The metastable garnet contact domain lies at higher μ_{FeO} and lower μ_{SiO2} compared to the stable chemical potentials in the equilibrium cordierite, plagioclase and orthopyroxene. Conversely, the metastable quartz contact domain lies at higher μ_{SiO2} and lower μ_{FeO}. The chemical potential gradient between these two metastable equilibria during incipient corona growth is represented by the dotted line in Figure 5.50c. Between these two extreme equilibria lies a continuous spectrum of non-overlapping compositional domains with intermediate chemical potentials along the chemical potential gradient. In order to equalize potentials as equilibrium is approached, SiO_2 must diffuse down the chemical potential gradient from quartz toward garnet and FeO must diffuse from garnet toward quartz. In quantitative μ-μ plots, the one-phase field can be contoured for mineral compositions (e.g., White et al., 2008). The chemical potential gradient prevailing during the final steady-state corona may be determined by matching the observed zonation in corona phases with mineral isopleths in quantitative μ-μ plots.

In reality, the chemical potential gradients are not linear as in Figure 5.50c owing to differences in the relative diffusion rates, and the partitioning of the corona bulk composition cannot be reflected as a linear continuum between the two endmember garnet-quartz and orthopyroxene-quartz compositions. Rapid FeO diffusion relative to SiO_2 leads to preferential FeO depletion in bulk compositions adjacent to garnet and FeO enrichment toward quartz. Chemical potential gradients are, thus, likely to be asymptotic (Figure 5.51), giving rise to a more complex spatial array of corona products in *P*-*T* space.

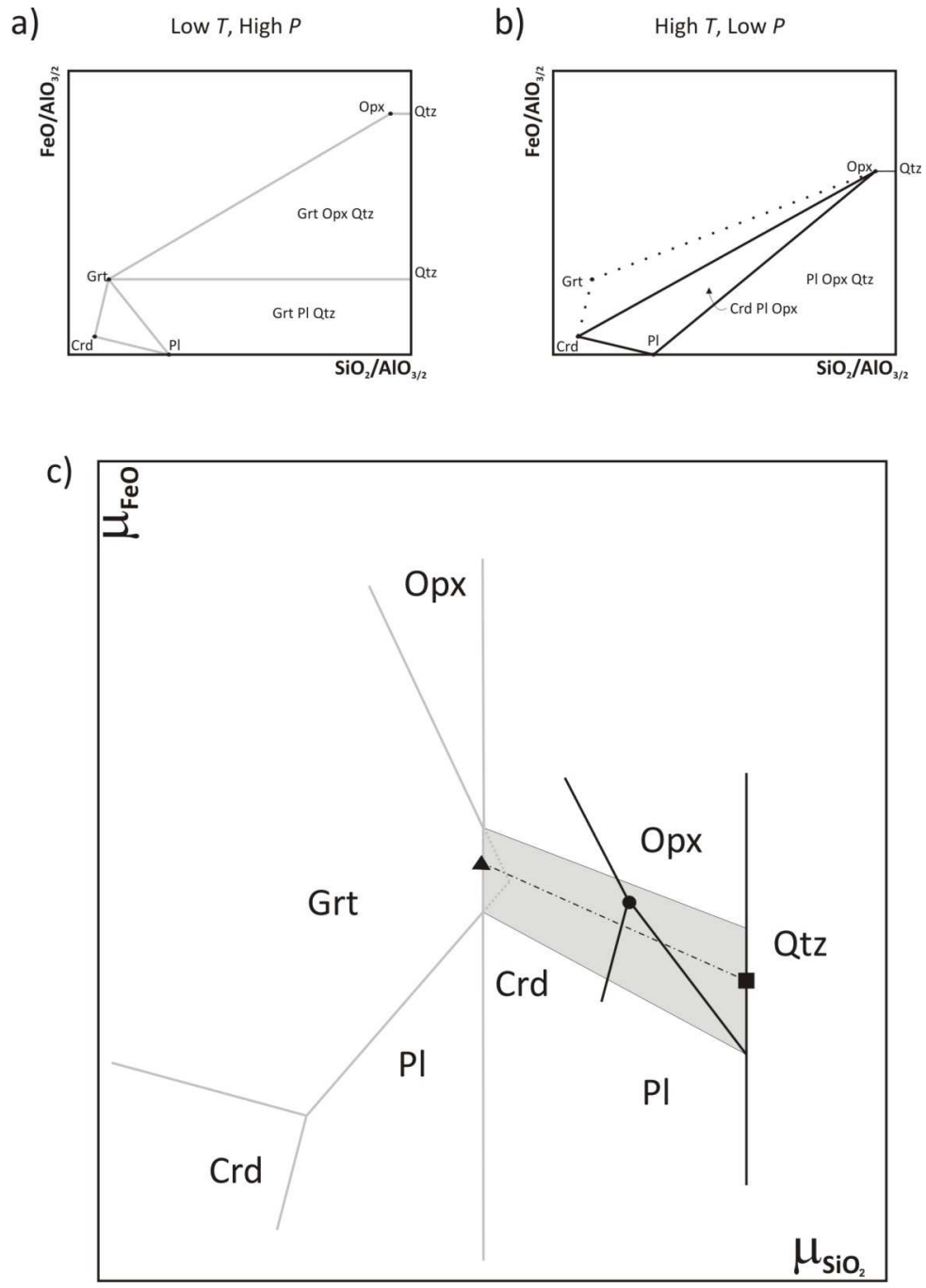

Figure 5.50: Orthogonal compatibility diagrams for: (a) pre-impact chemical potential relationships (in grey) and (b) post-impact chemical potential relationships (in black). Metastable equilibria are represented by dotted lines. Orthogonal compatibility diagrams are used to generate (c) a qualitative $\mu_{FeO} - \mu_{SiO_2}$ section in NCFAS. The metastable garnet-quartz equilibrium, in the pre-impact portion of μ-μ space at the garnet contact (black triangle) and metastable orthopyroxene-quartz in post-impact μ-μ space (black square) at the quartz contact, are characterized by unique chemical potentials and separated by a chemical potential gradient (grey field). The spatial array of corona product phases reflecting the prevailing chemical potential gradients is Crd→Pl→Opx from metastable garnet to quartz.

At the start of corona formation (Figure 5.51a, t = 1), partitioning of the corona band owing to variable interganular diffusivities yields two incipient metastable equilibria at the garnet contact A and quartz contact B and a continuum of non-overlapping bulk compositions with attendant chemical potentials along an asymptotic path from A to D, where points B and C represent points on the continuum. Equilibrium chemical potentials for the corona assemblage as a whole are those at point 'Equilibrium' in Figure 5.51. The sequence of corona layers dictated by the incipient chemical potential gradient grades from Crd (A,B) → Pl (C) → Opx (D), with mineral compositional zonation determined by isopleths in μ-μ space.

With prolonged reaction, the path in mu-mu space along which the chemical potentials of the corona compositional continuum evolves will depend on the rate at which different local chemical potentials can be equalised (White et al., 2008). This is a function of the relative fluxes for FeO and SiO_2, i.e., the amount of material diffusing through the corona to equalize chemical potential gradients across the corona (e.g., White et al., 2008) and relative rates of diffusion for FeO and SiO_2. With incipient reaction, the change in FeO chemical potentials lags behind that of Si owing to high FeO fluxes required for equalisation of chemical potentials despite a relative diffusion coefficient an order of magnitude higher than Si. The resultant chemical potentials at A, B, C and D track to new positions (indicated by yellow symbols), adjusting to values of μ_{SiO2} and μ_{FeO} approaching those at equilibrium ('Equilibrium' in Figure 5.51). The resultant transient chemical potential gradient is represented by the dotted line in Figure 5.51b. The chemical potentials of A shift to the reaction line between the cordierite and orthopyroxene one-phase fields, such that orthopyroxene is stable with cordierite at A and the symplectite starts to form. Chemical potentials at B, however, are still within the one-phase field in which cordierite alone is stable. Monomineralic plagioclase and orthopyroxene will form at C and D at the appropriate compositions dictated by isopleths intersected by the transient chemical potential gradient. The corona layer sequence is Crd→Opx→Crd→Pl→Opx.

With further reaction (t = 3, Figure 5.51c), SiO_2 diffusion, albeit less rapid than FeO, deflects the chemical potentials further toward their equilibrium values and new

transient chemical potentials defined by green symbols for A, B, C and D. Chemical potentials at A evolve along the 2-phase reaction line in mu-mu space from the yellow triangle to green triangle. Gradually, more points along the continuum between A and B track towards the two-phase reaction line between cordierite and orthopyroxene, such that the occurrence of Crd-Opx symplectite grades into the previously monomineralic Crd layer. The suppressed rate of chemical potential change for FeO owing to large requisite fluxes relative to SiO_2 manifests as a gradually more convex (compressed in μ_{SiO2} direction) transient chemical potential gradient.

The final steady-state configuration of corona layers is demonstrated in Figure 5.51d. The chemical potentials approach equilibrium values (blue symbols), but arrested reaction prevents complete equalization of potentials. More points along the compositional continuum, including those at B, now lie on the cordierite-orthopyroxene two-phase field boundary and the symplectite is near its maximum thickness. Chemical potentials for plagioclase (C) and blocky orthopyroxene (D) are frozen at values within the monomineralic phase fields. The final transient chemical potential gradient reflects the model chemical potential gradients (Figure 5.47), i.e., a relatively flatter, lower-magnitude chemical potential gradient for SiO_2 compared to FeO. An important conclusion is that the phases in coronas may very closely approach equilibrium if diffusion has permitted equalization of chemical potentials (as in SK9C) whilst still maintaining their spatial segregation. As chemical potentials are equalized with mass diffusion, the bulk compositions for A, B, C and D will expand and approach the same bulk value, within an encompassing equilibration volume.

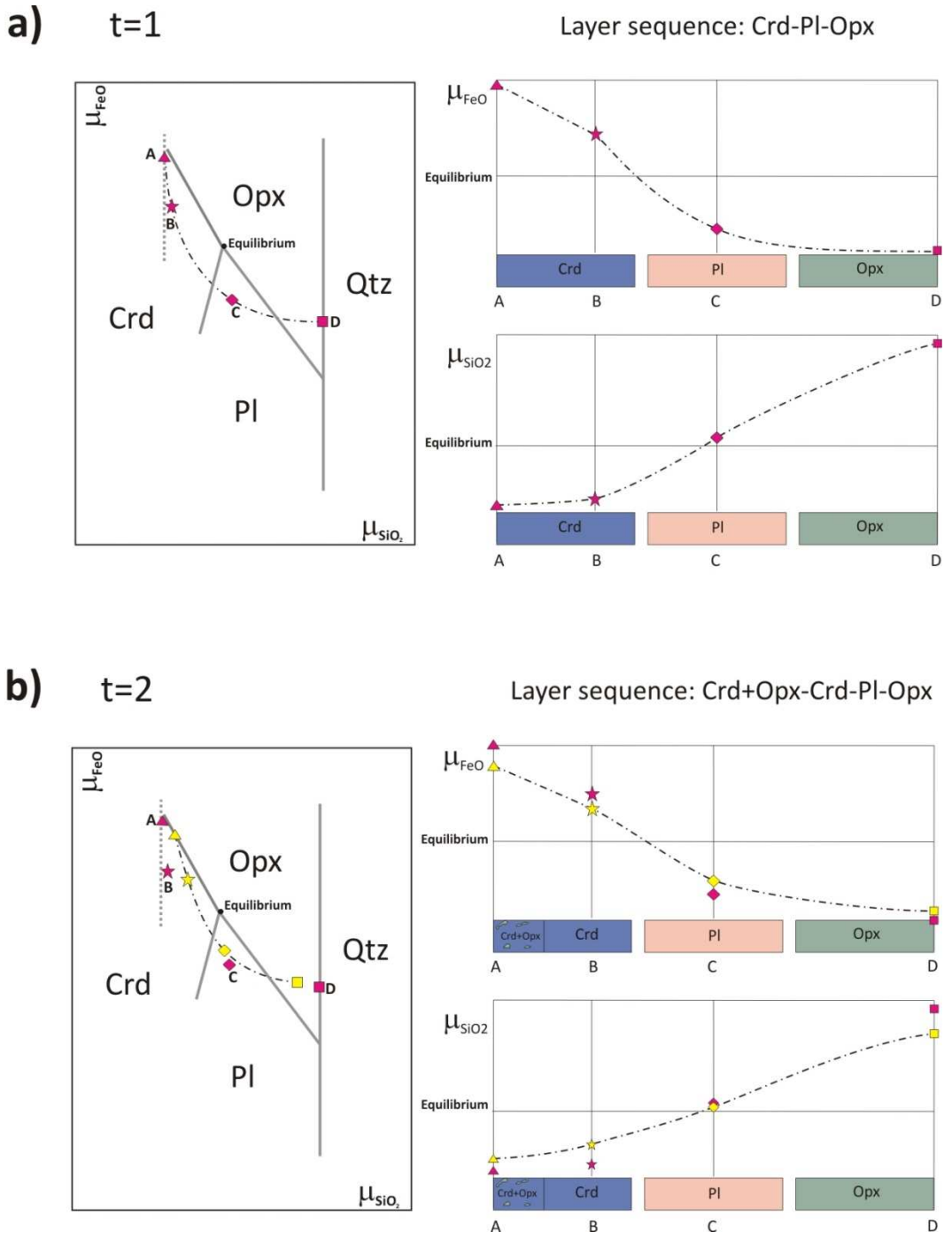

Figure 5.51: Evolving chemical potential gradients and corona structure with prolonged reaction and variable diffusion rates. (a) Establishment of incipient chemical potentials with partitioning of the corona bulk composition into local domains/equilibria. (b) With continued reaction, chemical potentials evolve to new values approaching the equilibrium chemical potentials for the corona as a whole (Equilibrium). Orthopyroxene is stable with cordierite at A with new chemical potentials (yellow triangle). SiO_2 chemical potentials shift marginally more rapidly than Fe chemical potentials.

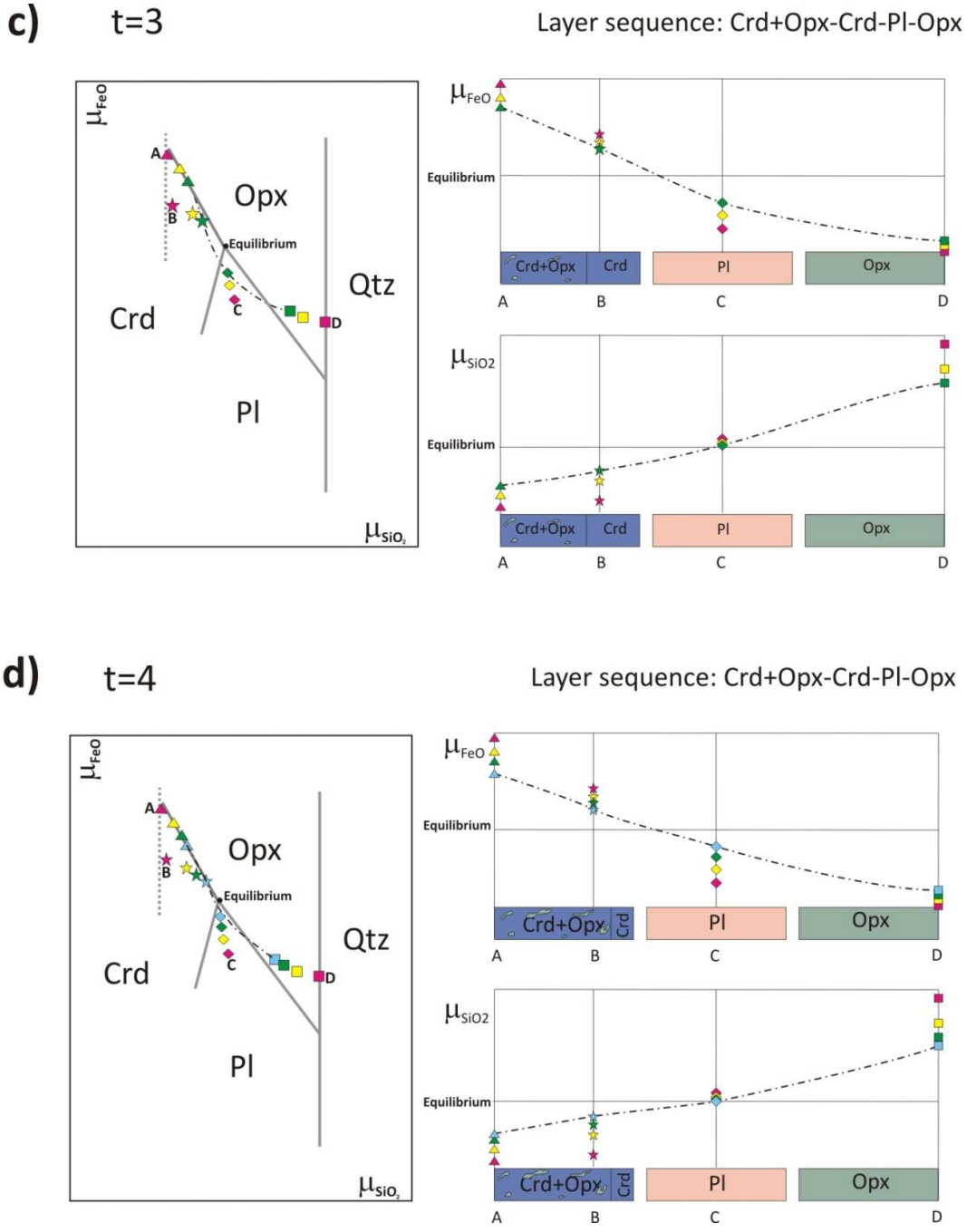

Figure 5.51 continued: Evolving chemical potential gradients and corona structure with prolonged reaction and variable diffusion rates. (c) and (d) Progressive evolution of component chemical potentials and spatial array of corona products with prolonged reaction as equilibration is gradually approached. Details in text.

5.3.7 Gibbs free energy gradients of corona phases

Diffusion modelling of coronas permits the calculation of the Gibbs free energy of the corona phases in layers (Joesten, 1977; Fisher, 1977; Ashworth and Sheplev, 1997; Appendix A). At equilibrium, at constant *P* and *T*, for each phase in the system, the Gibbs-Duhem equation relates the molar Gibbs free energy G_m, of mineral *m*, to the chemical potentials μ_i in the mineral *m*,

$$G_m = \sum_{i=1}^{S} n_{im}\mu_i \qquad eqn\ 5.4$$

Over a corona layer *q*, at equilibrium, the gradient in Gibbs free energy of a phase is given by the equation (Joesten, 1977):

$$\frac{dG_m}{dx} = \sum_{i=1}^{S} n_{im}\frac{d\mu_i}{dx} \qquad eqn\ 5.5$$

where n_{im} is the number of moles of component *i* in 1 mole of mineral *m* and $\frac{d\mu_i}{dx}$ is the model chemical potential gradient for component *i* in layer *q*.

Gibbs free energy gradients for phases in layers in all coronas are presented in Figure 5.52. If a mineral is stable in local equilibrium in layer *q*, the Gibbs free energy gradient for that phase in layer *q* is zero, e.g., in all coronas the Gibbs free energy gradients for orthopyroxene and cordierite in layer 1 symplectite are both zero. Highest-magnitude gradients in Gibbs free energy of phases in layers are due to inherently large chemical potential gradients for components in those phases in the layer. The larger the gradient in Gibbs free energy for a phase in a layer, the further that layer and the corona as a whole is away from equilibrium. In general, the Gibbs free energy gradients for all phases in layers in corona SK8C greatly exceed those of other coronas, indicative of the largest deviation from overall equilibrium in the corona. Lowest Gibbs free energy gradients for phases in layers are observed in SK9C, indicative of enhanced equalization of chemical potentials and, hence, greater equilibration in this corona.

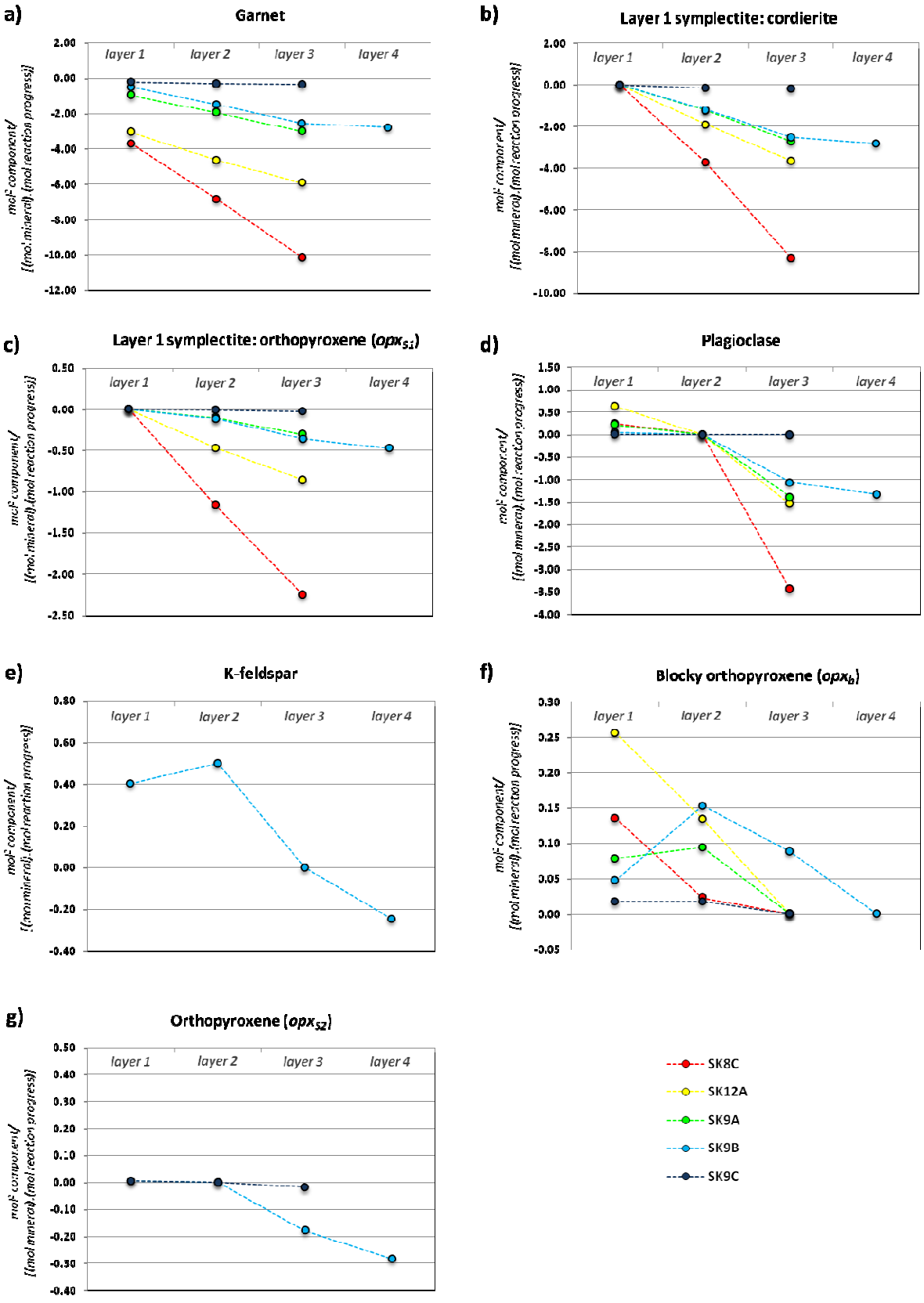

Figure 5.52: Model Gibbs free energy gradients for all corona phases in layers in coronas SK8C, SK12A, SK9A, SK9B and SK9C.

SK12A, SK9B and SK9A exhibit intermediate Gibbs free energy gradients, with similar gradients in SK9A and SK9B. SK12A gradients approach those of SK8C but are generally lower in magnitude.

The Gibbs free energy gradients for blocky orthopyroxene (Opx_b) show anomalous trends in layer 2 in all coronas except SK9C. SK8C has a lower gradient than SK12A, SK9A and SK9B, despite consistently higher chemical potential gradients for all components over this layer compared to other coronas. This is because the composition of Opx_b in SK8C is such that the nett contribution of each component's chemical potential gradient (negative and positive) to the total Gibbs free energy gradient for the phase in layer 2 approaches zero.

5.3.8 Stability Criterion

Before a diffusion model is accepted as a viable interpretation of a layer sequence, a basic thermodynamic criterion, as defined by Ashworth and Sheplev (1997), must be satisfied. The full derivation of the stability criterion after Ashworth and Sheplev (1997) is included in Appendix A, and only the major equations are summarised below.

The stability criterion is based on the principle that, in a layer where mineral *k* is absent, the intergranular diffusion medium should not be supersaturated with respect to *k* (Ashworth and Sheplev, 1997). The Gibbs free energy of a mineral is determined from the equation:

$$G_k = \sum_{i=1}^{S} n_{ik}\mu_i \qquad eqn\ 5.4$$

Ashworth and Sheplev (1997) formulated an analogous quantity defining the saturation state of the intergranular medium (IGM) with respect to mineral *k* as:

$$G_k^{IGM} = \sum_{i=1}^{S} n_{ik}\mu_i \qquad eqn\ 5.6$$

The intergranular medium may be a fluid, but this term is also valid for a disordered grain boundary medium in fluid-absent conditions (Ashworth and Sheplev, 1997) or a melt-laden grain boundary medium.

At local equilibrium, the chemical potential of each component in the mineral *k* must be equal to the chemical potential of the respective component in the intergranular medium (Ashworth and Sheplev, 1997). The equality of chemical potentials constrains $G_k = G_k^{IGM}$. If $G_k < G_k^{IGM}$, the interganular medium is super-saturated with respect to *k* and, wherever *k* is absent, $G_k > G_k^{IGM}$(Ashworth and Sheplev, 1997). The variation in G_k^{IGM}across a layer in a corona is dependent on layer thickness and chemical potential gradients. Ashworth and Sheplev (1997) derived an equation allowing the calculation of differences of G_k^{IGM}across layers in a corona (see Appendix A):

$$[(G_k^{IGM})^q - (G_k^{IGM})^1]^* = \sum_{i=1}^{S} n_{ik} \sum_{r=1}^{q-1} h^{r*} \left(\frac{d\mu_i}{dx}\right)^{r*} \qquad eqn\ 5.7$$

As a basic constraint in the model,

$$\sum_{i=1}^{S} n_{ik} \frac{d\mu_i}{dx} = 0 \qquad eqn\ 5.8$$

Consequently, $[(G_k^{IGM})^q - (G_k^{IGM})^1]^*$ has a constant value in all layers where k is present, i.e., $[G_k - (G_k^{IGM})^1]^*$ (Ashworth and Sheplev, 1997). The stability criterion is satisfied if $[(G_k^{IGM})^q - (G_k^{IGM})^1]^*$ at all boundaries is less than the constant value (Ashworth and Sheplev, 1997). Subtracting the constant value $[G_k - (G_k^{IGM})^1]^*$ from $[(G_k^{IGM})^q - (G_k^{IGM})^1]^*$ yields $[(G_k^{IGM})^q - G_k]^*$. A layer sequence is stable if $[(G_k^{IGM})^q - G_k]^* \leq 0$.

The quantity $[(G_k^{IGM})^q - G_k]^*$ for phases across layers in the coronas investigated is plotted in Figure 5.53a-g. In all coronas, the stability criterion is satisfied for all phases, i.e., $[(G_k^{IGM})^q - G_k]^* \leq 0$. The magnitude of $[(G_k^{IGM})^q - G_k]^*$ is smallest in SK9C in all layers for all phases. Apart from blocky orthopyroxene (Opx_b), SK8C

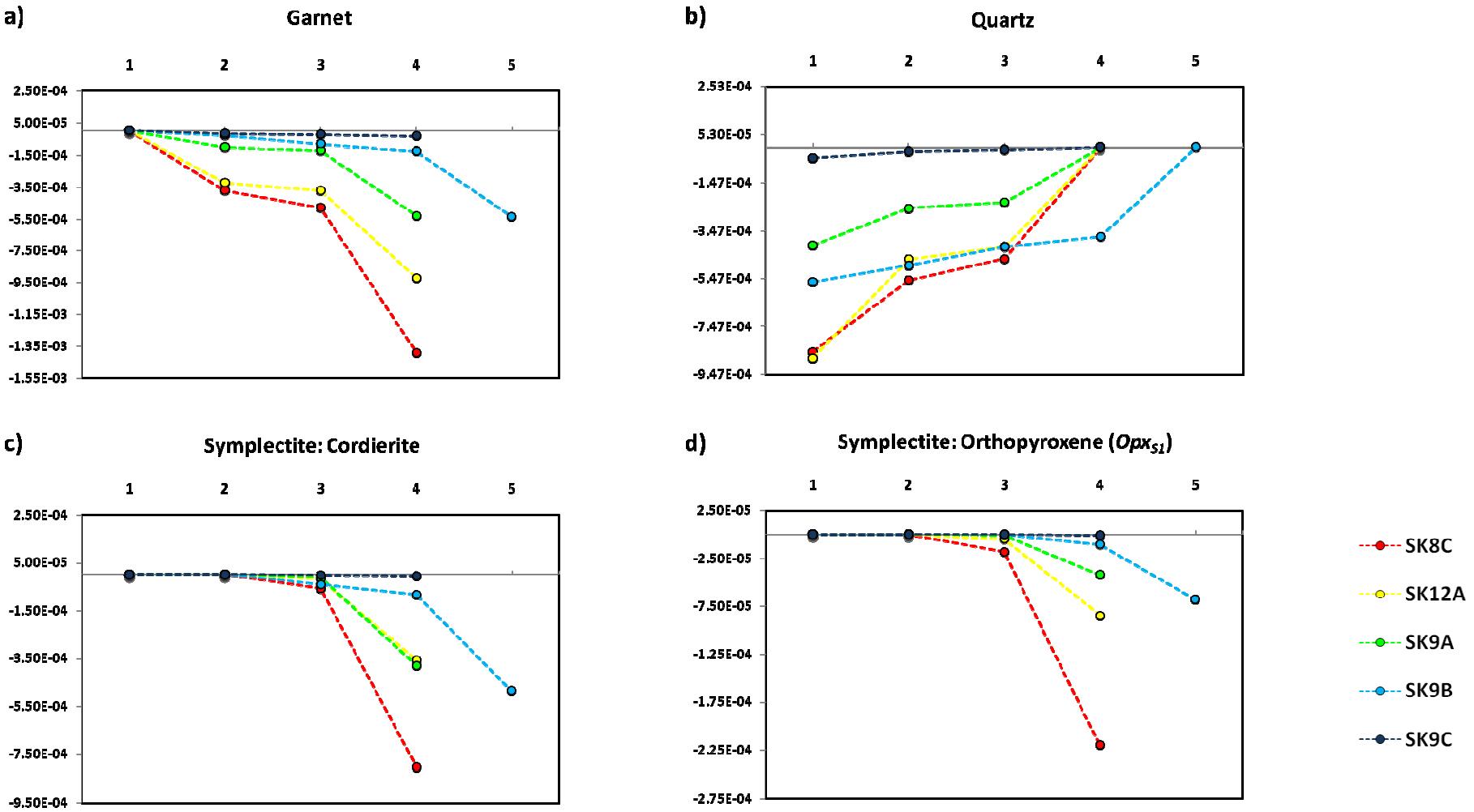

Figure 5.53: Model free energy differences of phases at boundary q from those at boundary where phase is present (must be ≤0 for stability).

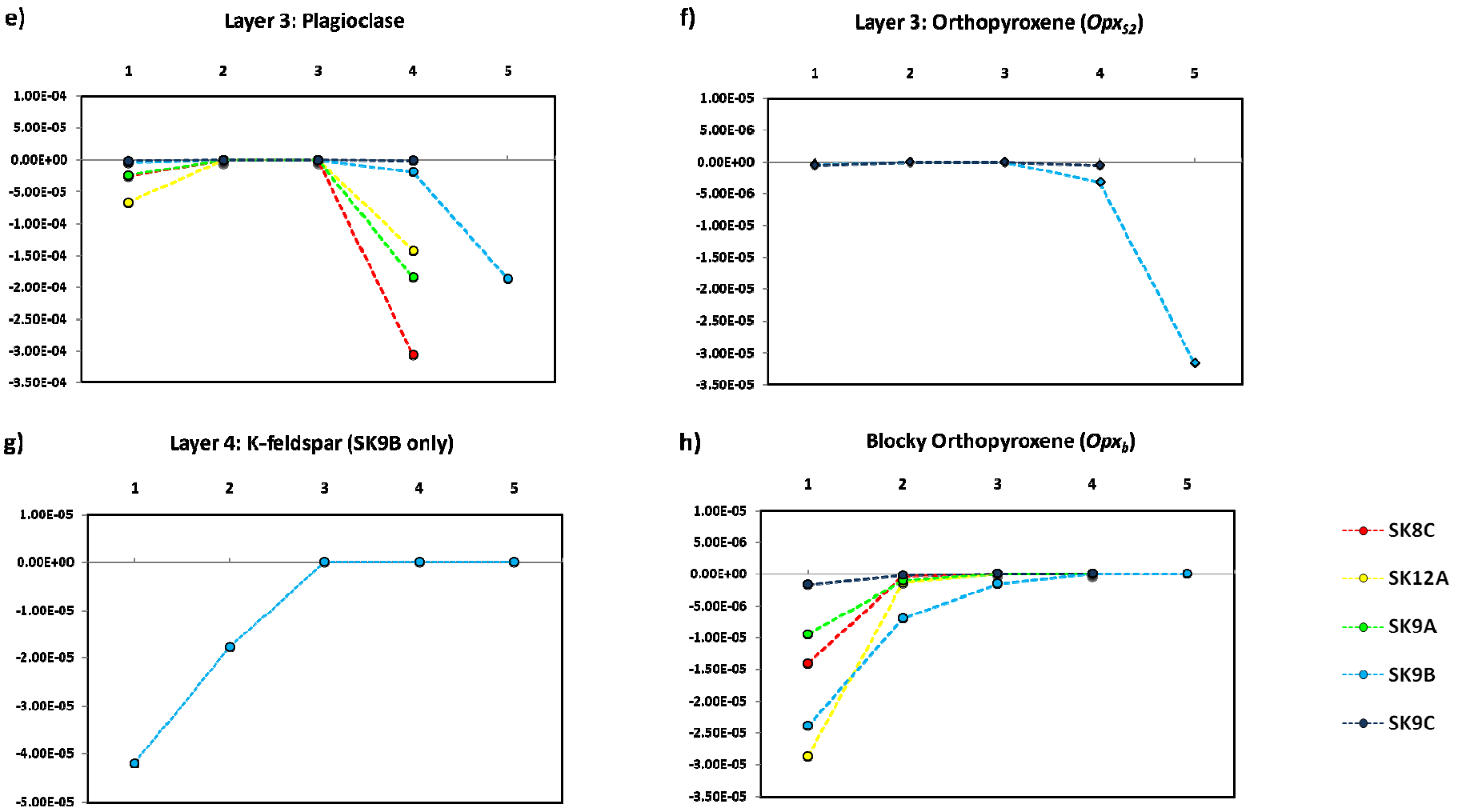

Figure 5.53 continued: Model free energy differences of phases at boundary q from those at boundary where phase is present (must be ≤0 for stability).

exhibits the largest difference in $[(G_k^{IGM})^q - G_k]^*$ for garnet, quartz, cordierite, symplectite orthopyroxene and plagioclase, consistent with higher-magnitude free energy gradients for these phases in this corona. Intermediate values of $[(G_k^{IGM})^q - G_k]^*$ for phases in other coronas reflect the fluctuating free energy gradients as a function of phase composition and respective chemical potential gradients.

5.3.9 Non-equilibrium thermobarometry

The existence of chemical potential gradients across the coronas examined in this study (Section 5.3.5) prevents the application of conventional thermobarometry that is predicated on the assumption that all minerals are in equilibrium with zero affinity for reaction (cf. Perchuk et al., 2002). An innovative extension to conventional thermobarometry to accommodate minerals separated by chemical potential gradients has been derived by Ashworth et al. (2001). Instead of constraining the region in *P*-*T* space where endmember reaction affinities defining a local equilibrium are zero, this technique isolates regions in *P*-*T* space where ratios in end-member reaction affinities obtained from corona modelling correspond with respective end-member reaction affinity ratios obtained independently from the internally consistent thermodynamic database of Holland and Powell (1998, November 2003 upgrade). A major assumption in non-equilibrium thermobarometry is that of approximate constancy of prevailing *P* and *T* during corona formation. Ashworth and Sheplev (1997) argued that this is a reasonable assumption for most coronas. The detailed derivation of the non-equilibrium thermobarometric technique is included in Appendix A (Ashworth et al., 2001) and is summarized below.

Endmember reaction affinity is evaluated at two boundary locations: boundary 1 (case A) and boundary 5 (case B) (Ashworth et al., 2001). The average composition of a phase comprising endmember *j* in local metastable equilibria at location A or B is known and this provides a reference location for the chemical potential ($\mu_j{}^*$). The difference in $\mu_j{}^*$ between the reference location and any point in the corona (typically, A or B) will give rise to a chemical potential gradient and reaction affinity. The reference locations are defined at layer boundaries for convenience in

calculation such that the chemical potential difference for $\mu_j{}^*$ is the sum of differences across layers (Ashworth et al., 2001). If the reference boundary is q_j and the boundary at which affinity is evaluated is q, then differences in chemical potentials across the corona are yielded by the following expressions, where h^{r*} are the model layer (r) thicknesses (after Ashworth et al., 2001):

$$\left(\mu_j^{qj} - \mu_j^{q}\right)^* = -\sum_{r=q_j}^{q-1} h^{r*}\left(\frac{d\mu_j}{dx}\right)^{r*} \quad if\ q_j < q \qquad eqn\ 5.9a$$

$$\left(\mu_j^{qj} - \mu_j^{q}\right)^* = \sum_{r=q}^{q_j-1} h^{r*}\left(\frac{d\mu_j}{dx}\right)^{r*} \quad if\ q_j > q \qquad eqn\ 5.9b$$

Differences in $\mu_j{}^*$ for each end-member across each corona layer are given in Tables 5.12-5.16.

The model reaction affinity for each end-member reaction k, where v_{jk} is the stoichiometric coefficient of each end-member j, is given by (Ashworth et al., 2001):

$$(-\Delta G)_k^* = \sum_j v_{jk}\left(\mu_j^{qj} - \mu_j^{q}\right)^* \qquad eqn\ 5.10$$

In all coronas, boundary 1 is the reference location for garnet, cordierite and symplectite orthopyroxene (Opx_{S1}). Boundary 4 in SK8C, SK12A, SK9A and SK9C is the reference location for quartz and blocky orthopyroxene (Opx_b). Boundary 5 is the reference location for quartz and blocky orthopyroxene in SK9B. The reference boundary for plagioclase is either boundary 2 or boundary 3, depending on which boundary is nearest to the boundary at which affinity is evaluated.

In case A, reaction affinity is evaluated at boundary 1, i.e., the garnet contact (Figure 5.54). Phases absent from boundary 1 and contributing to reaction affinity are quartz and plagioclase. The end-member absent is anorthite and the reference location is the nearest boundary at which it is present, i.e., boundary 2.

EVALUATION OF REACTION AFFINITY AT BOUNDARY 1
(CASE A, *q*=1)

$$(-\Delta G)_k^* = \sum_{j=an} v_{j,k}\left(\mu_j^{qj} - \mu_j^{q}\right)^* + \sum_{j=qtz} v_{j,k}\left(\mu_j^{qj} - \mu_j^{q}\right)$$

$$(-\Delta G)_k^* = v_{an,k}\left(\mu_{an}^{2} - \mu_{an}^{1}\right)^* + v_{qtz,k}\left(\mu_{qtz}^{4} - \mu_{qtz}^{1}\right)^*$$

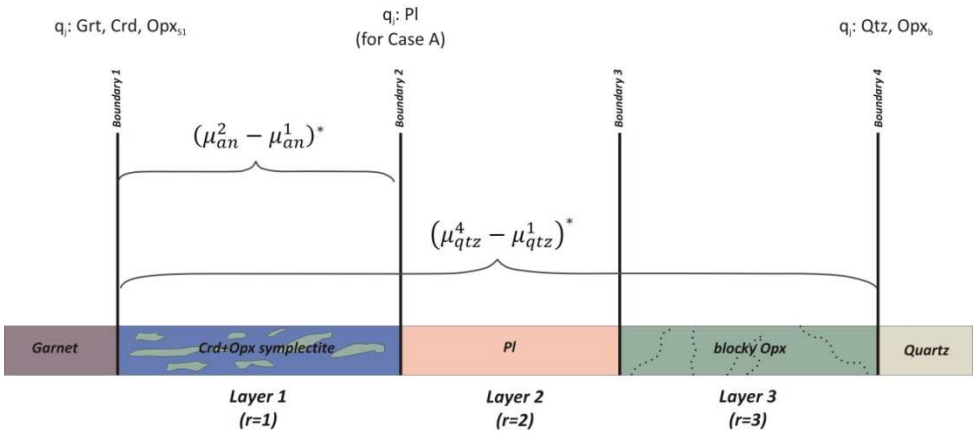

EVALUATION OF REACTION AFFINITY AT BOUNDARY 4
(CASE B, *q*=4)

$$(-\Delta G)_k^* = \sum_{\substack{j=crd,fcrd,\\ mncrd}} v_{j,k}\left(\mu_j^{qj} - \mu_j^{q}\right)^* + \sum_{\substack{j=prp,\,alm,\\ grs,\,sps}} v_{j,k}\left(\mu_j^{qj} - \mu_j^{q}\right)^* + \sum_{j=an} v_{j,k}\left(\mu_j^{qj} - \mu_j^{q}\right)$$

$$(-\Delta G)_k^* = \sum_{\substack{j=crd,fcrd,\\ mncrd}} v_{j,k}\left(\mu_j^{1} - \mu_j^{4}\right)^* + \sum_{\substack{j=prp,\,alm,\\ grs,\,sps}} v_{j,k}\left(\mu_j^{1} - \mu_j^{4}\right)^* + \sum_{j=an} v_{j,k}\left(\mu_j^{1} - \mu_j^{3}\right)^*$$

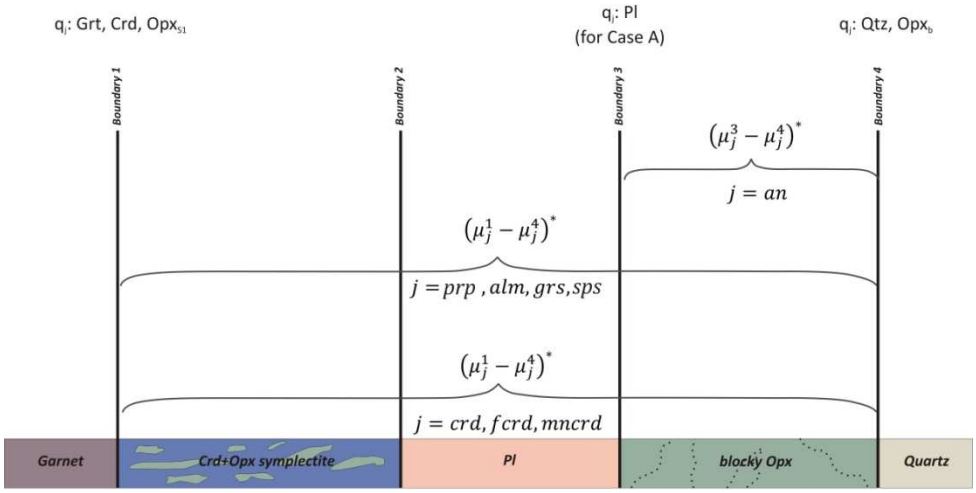

Figure 5.54: Evaluation of reaction affinity at reference boundary A (q_j>q) and B (q_j<q). Details are explained in the text.

Since $q_j > q$, calculation of $(-\Delta G)_k^*$ for endmember reaction k at boundary 1 or location A reduces to:

$$(-\Delta G)_k^* = \sum_{j=an} v_{j,k}\left(\mu_j^{qj} - \mu_j^{q}\right)^* + \sum_{j=qtz} v_{j,k}\left(\mu_j^{qj} - \mu_j^{q}\right)^*$$

$$(-\Delta G)_k^* = v_{an,k}(\mu_{an}^2 - \mu_{an}^1)^* + v_{qtz,k}\left(\mu_{qtz}^4 - \mu_{qtz}^1\right)^*$$

$$(-\Delta G)_k^* = v_{an,k}\sum_{r=1}^{2-1} h^{r*}\left(\frac{d\mu_{an}}{dx}\right)^{r*} + v_{qtz,k}\sum_{r=1}^{4-1} h^{r*}\left(\frac{d\mu_{qtz}}{dx}\right)^{r*}$$

In case B (Figure 5.54), reaction affinity is evaluated at the quartz contact, i.e., boundary 4 for SK8C, SK12A, SK9A, SK9C, and boundary 5 for SK9B. Phases absent from this boundary and contributing to reaction affinity include cordierite, garnet and plagioclase. The reference location for cordierite and garnet is boundary 1 and the reference location for plagioclase is boundary 3. In this instance, $q_j < q$, such that end-member reaction affinity at boundary 4 or location B reduces to:

$$(-\Delta G)_k^* = \sum_{\substack{j=crd,fcrd,\\ mncrd}} v_{j,k}\left(\mu_j^{qj} - \mu_j^{q}\right)^* + \sum_{\substack{j=prp,alm,\\ grs,sps}} v_{j,k}\left(\mu_j^{qj} - \mu_j^{q}\right)^* + \sum_{j=an} v_{j,k}\left(\mu_j^{qj} - \mu_j^{q}\right)^*$$

$$(-\Delta G)_k^* = \sum_{\substack{j=crd,fcrd,\\ mncrd}} v_{j,k}\left(\mu_j^{1} - \mu_j^{4}\right)^* + \sum_{\substack{j=prp,alm,\\ grs,sps}} v_{j,k}\left(\mu_j^{1} - \mu_j^{4}\right)^* + \sum_{j=an} v_{j,k}\left(\mu_j^{3} - \mu_j^{4}\right)^*$$

$$(-\Delta G)_k^* = \sum_{\substack{j=crd,fcrd,\\ mncrd}} -v_{j,k}\sum_{r=qj}^{q-1} h^{r*}\left(\frac{d\mu_j}{dx}\right)^{r*} + \sum_{\substack{j=prp,alm,\\ grs,sps}} -v_{j,k}\sum_{r=qj}^{q-1} h^{r*}\left(\frac{d\mu_j}{dx}\right)^{r*} + \sum_{j=an} -v_{j,k}\sum_{r=qj}^{q-1} h^{r*}\left(\frac{d\mu_j}{dx}\right)^{r*}$$

$$(-\Delta G)_k^* = \sum_{\substack{j=crd,fcrd,\\ mncrd}} -v_{j,k}\sum_{r=1}^{3} h^{r*}\left(\frac{d\mu_j}{dx}\right)^{r*} + \sum_{\substack{j=prp,alm,\\ grs,sps}} -v_{j,k}\sum_{r=1}^{3} h^{r*}\left(\frac{d\mu_j}{dx}\right)^{r*} + \sum_{j=an} -v_{j,k}\sum_{r=3}^{3} h^{r*}\left(\frac{d\mu_j}{dx}\right)^{r*}$$

Table 5.12: SK8C : Chemical potential relationships for components and end-members across corona layers

Model chemical potential gradients for components in layers 1 to 3 (mol mineral/mol reaction progress)

	hr (10^{-4} m^3/mol)*	*Si*	*Al*	*Fe^{3+}*	*Fe^{2+}*	*Mn*	*Mg*	*Ca*	*Na*	*K*
Layer 1	1.009373	0.24463	-0.3875	0.010333	-1.0904	-0.038528	0.56135	-0.072851	-0.2052	-0.008
Layer 2	0.156274	0.48405	-1.2491	0.055867	-1.238	-0.040249	0.26225	0.0040883	0.061038	0.0023334
Layer 3	0.896378	0.43037	-2.087	0.045605	-1.1681	-0.038976	0.35285	-0.013864	0.0003096	-0.0000236

Model chemical potential differences for components across layers (m^3/mol): $h^{r*}(d\mu_i/dx)^{r*}$

	Si	*Al*	*Fe^{3+}*	*Fe^{2+}*	*Mn*	*Mg*	*Ca*	*Na*	*K*
Layer 1	0.000025	-0.000039	0.000001	-0.000110	-0.000004	0.000057	-0.000007	-0.000021	-0.000001
Layer 2	0.000008	-0.000020	0.000001	-0.000019	-0.000001	0.000004	0.000000	0.000001	0.000000
Layer 3	0.000039	-0.000187	0.000004	-0.000105	-0.000003	0.000032	-0.000001	0.000000	0.000000

Model chemical potential differences for endmembers across layers (m^3/mol): $h^{r*}(d\mu_i/dx)^{r*}$

	alm	*prp*	*grs*	*sps*	*crd*	*fcrd*	*mncrd*	*en*	*fs*	*mgts*	*an*	*qtz*
Layer 1	-0.000334	0.000166	-0.000019	-0.000016	0.000080	-0.000253	-0.000041	0.000163	-0.000171	0.000003	-0.000036	-0.000334
Layer 2	-0.000074	-0.000004	-0.000016	-0.000018	-0.000032	-0.000079	-0.000042	0.000023	-0.000024	-0.000027	-0.000024	-0.000074
Layer 3	-0.000573	-0.000164	-0.000261	-0.000269	-0.000492	-0.000765	-0.000562	0.000140	-0.000132	-0.000304	-0.000298	-0.000573

Model chemical potential differences for components from boundary 1 at boundary q (m^3/mol)

	Si	*Al*	*Fe^{3+}*	*Fe^{2+}*	*Mn*	*Mg*	*Ca*	*Na*	*K*
Boundary 2	0.000025	-0.000039	0.000001	-0.000110	-0.000004	0.000057	-0.000007	-0.000021	-0.000001
Boundary 3	0.000032	-0.000059	0.000002	-0.000129	-0.000005	0.000061	-0.000007	-0.000020	-0.000001
Boundary 4	0.000071	-0.000246	0.000006	-0.000234	-0.000008	0.000092	-0.000009	-0.000020	-0.000001

Model chemical potential differences for endmembers from boundary 1 at boundary q (m^3/mol)

		alm	*prp*	*grs*	*sps*	*crd*	*fcrd*	*mncrd*	*en*	*fs*	*mgts*	*an*	*qtz*
Boundary 2	$\sum_{r=1}^{1} h^{r*}(d\mu_j/dx)^{r*}$	-0.000334	0.000166	-0.000019	-0.000016	0.000080	-0.000253	-0.000041	0.000163	-0.000171	0.000003	-0.000334	0.000166
Boundary 3	$\sum_{r=1}^{2} h^{r*}(d\mu_j/dx)^{r*}$	-0.000409	0.000162	-0.000035	-0.000034	0.000048	-0.000332	-0.000082	0.000186	-0.000194	-0.000024	-0.000409	0.000162
Boundary 4	$\sum_{r=1}^{3} h^{r*}(d\mu_j/dx)^{r*}$	-0.000981	-0.000002	-0.000296	-0.000303	-0.000444	-0.001097	-0.000645	0.000326	-0.000327	-0.000328	-0.000981	-0.000002

Table 5.13: SK12A : Chemical potential relationships for components and end-members across corona layers

Model chemical potential gradients for components in layers 1 to 3 (mol mineral/mol reaction progress)

	hr^* ($10^{-4}m^3$/mol)	Si	Al	Fe^{3+}	Fe^{2+}	Mn	Mg	Ca	Na	K
Layer 1	1.063224	0.322560	-0.400460	0.102460	-0.912850	0.000000	0.441200	-0.088919	-0.103400	-0.003000
Layer 2	0.103440	0.410680	-0.811690	0.117130	-0.983900	0.000000	0.322600	-0.005474	0.021981	0.000482
Layer 3	0.924680	0.372770	-1.107500	0.120680	-0.953840	0.000000	0.350590	-0.020056	-0.000266	-0.000136

Model chemical potential differences for components across layers (m^3/mol): $h^{r*}(d\mu_i/dx)^{r*}$

	Si	Al	Fe^{3+}	Fe^{2+}	Mn	Mg	Ca	Na	K
Layer 1	0.000034	-0.000043	0.000011	-0.000097	0.000000	0.000047	-0.000009	-0.000011	0.000000
Layer 2	0.000004	-0.000008	0.000001	-0.000010	0.000000	0.000003	0.000000	0.000000	0.000000
Layer 3	0.000034	-0.000102	0.000011	-0.000088	0.000000	0.000032	-0.000002	0.000000	0.000000

Model chemical potential differences for endmembers across layers (m^3/mol): $h^{r*}(d\mu_j/dx)^{r*}$

	alm	prp	grs	crd	fcrd	mgts	en	fs	an	qtz
Layer 1	-0.000273	0.000158	-0.000001	0.000095	-0.000193	-0.000004	0.000162	-0.000126	-0.000026	0.000034
Layer 2	-0.000035	0.000006	-0.000004	-0.000006	-0.000033	-0.000009	0.000015	-0.000012	-0.000008	0.000004
Layer 3	-0.000366	-0.000004	-0.000105	-0.000172	-0.000414	-0.000138	0.000134	-0.000107	-0.000138	0.000034

Model chemical potential differences for components from boundary 1 at boundary q (m^3/mol)

	Si	Al	Fe^{3+}	Fe^{2+}	Mn	Mg	Ca	Na	K
Boundary 2	0.000034	-0.000043	0.000011	-0.000097	0.000000	0.000047	-0.000009	-0.000011	0.000000
Boundary 3	0.000039	-0.000051	0.000012	-0.000107	0.000000	0.000050	-0.000010	-0.000011	0.000000
Boundary 4	0.000073	-0.000153	0.000023	-0.000195	0.000000	0.000083	-0.000011	-0.000011	0.000000

Model chemical potential differences for endmembers from boundary 1 at boundary q (m^3/mol)

		alm	prp	grs	crd	fcrd	mgts	en	fs	an	qtz
Boundary 2	$\sum_{r=1}^{1} h^{r*}(d\mu_j/dx)^{r*}$	-0.000273	0.000158	-0.000001	0.000095	-0.000193	-0.000004	0.000162	-0.000126	-0.000026	0.000034
Boundary 3	$\sum_{r=1}^{2} h^{r*}(d\mu_j/dx)^{r*}$	-0.000308	0.000164	-0.000005	0.000089	-0.000226	-0.000013	0.000178	-0.000137	-0.000034	0.000039
Boundary 4	$\sum_{r=1}^{3} h^{r*}(d\mu_j/dx)^{r*}$	-0.000674	0.000160	-0.000110	-0.000083	-0.000639	-0.000151	0.000311	-0.000245	-0.000172	0.000073

Table 5.14: SK9A : Chemical potential relationships for components and end-members across corona layers

Model chemical potential gradients for components in layers 1 to 3 (mol mineral/mol reaction progress)

	hr^* (10^{-4} m^3/mol)	Si	Al	Fe^{3+}	Fe^{2+}	Mn	Mg	Ca	Na	K
Layer 1	1.052060	0.122490	-0.133930	0.065636	-0.263110	0.000000	0.114540	-0.064586	-0.092800	-0.004000
Layer 2	0.116439	0.174050	-0.405390	0.086185	-0.297410	0.000000	0.068342	0.014080	0.059651	0.002574
Layer 3	1.341394	0.141280	-0.660940	0.107740	-0.264390	0.000000	0.095274	-0.016276	-0.000196	-0.000007

Model chemical potential differences for components across layers (m^3/mol): $h^{r*}(d\mu_i/dx)^{r*}$

	Si	Al	Fe^{3+}	Fe^{2+}	Mn	Mg	Ca	Na	K
Layer 1	0.000013	-0.000014	0.000007	-0.000028	0.000000	0.000012	-0.000007	-0.000010	0.000000
Layer 2	0.000002	-0.000005	0.000001	-0.000003	0.000000	0.000001	0.000000	0.000001	0.000000
Layer 3	0.000019	-0.000089	0.000014	-0.000035	0.000000	0.000013	-0.000002	0.000000	0.000000

Model chemical potential differences for endmembers across layers (m^3/mol): $h^{r*}(d\mu_j/dx)^{r*}$

	alm	prp	grs	crd	fcrd	mgts	en	fs	an	qtz
Layer 1	-0.000073	0.000047	-0.000003	0.000032	-0.000047	-0.000003	0.000050	-0.000030	-0.000009	0.000013
Layer 2	-0.000014	-0.000001	-0.000003	-0.000007	-0.000016	-0.000007	0.000006	-0.000003	-0.000005	0.000002
Layer 3	-0.000227	-0.000082	-0.000125	-0.000234	-0.000331	-0.000146	0.000063	-0.000033	-0.000142	0.000019

Model chemical potential differences for components from boundary 1 at boundary q (m^3/mol)

	Si	Al	Fe^{3+}	Fe^{2+}	Mn	Mg	Ca	Na	K
Boundary 2	0.000013	-0.000014	0.000007	-0.000028	0.000000	0.000012	-0.000007	-0.000010	0.000000
Boundary 3	0.000015	-0.000019	0.000008	-0.000031	0.000000	0.000013	-0.000007	-0.000009	0.000000
Boundary 4	0.000034	-0.000107	0.000022	-0.000067	0.000000	0.000026	-0.000009	-0.000009	0.000000

Model chemical potential differences for endmembers from boundary 1 at boundary q (m^3/mol)

		alm	prp	grs	crd	fcrd	mgts	en	fs	an	qtz
Boundary 2	$\sum_{r=1}^{1} h^{r*}(d\mu_j/dx)^{r*}$	-0.000073	0.000047	-0.000003	0.000032	-0.000047	-0.000003	0.000050	-0.000030	-0.000009	0.000013
Boundary 3	$\sum_{r=1}^{2} h^{r*}(d\mu_j/dx)^{r*}$	-0.000086	0.000046	-0.000006	0.000025	-0.000063	-0.000010	0.000056	-0.000032	-0.000014	0.000015
Boundary 4	$\sum_{r=1}^{3} h^{r*}(d\mu_j/dx)^{r*}$	-0.000313	-0.000036	-0.000131	-0.000209	-0.000394	-0.000155	0.000119	-0.000065	-0.000156	0.000034

Table 5.15: SK9B : Chemical potential relationships for components and end-members across corona layers

Model chemical potential gradients for components in layers 1 to 3 (mol mineral/mol reaction progress)

	hr^* ($10^{-4}m^3$/mol)	Si	Al	Fe^{3+}	Fe^{2+}	Mn	Mg	Ca	Na	K
Layer 1	0.598881	0.096827	-0.090947	0.005350	-0.146630	0.000000	-0.002541	-0.080548	-0.138730	-0.057427
Layer 2	0.351689	0.184390	-0.384510	0.011550	-0.200940	0.000000	-0.090766	0.025002	0.036329	-0.056934
Layer 3	0.174871	0.193800	-0.637910	-0.009330	-0.211220	0.000000	-0.101690	-0.010148	0.001395	0.003732
Layer 4	1.597822	0.180630	-0.679210	-0.005737	-0.208720	0.000000	-0.099052	-0.010111	0.000021	-0.000012

Model chemical potential differences for components across layers (m^3/mol): $h^{r*}(d\mu_i/dx)^{r*}$

	Si	Al	Fe^{3+}	Fe^{2+}	Mn	Mg	Ca	Na	K
Layer 1	0.000006	-0.000005	0.000000	-0.000009	0.000000	0.000000	-0.000005	-0.000008	-0.000003
Layer 2	0.000006	-0.000014	0.000000	-0.000007	0.000000	-0.000003	0.000001	0.000001	-0.000002
Layer 3	0.000003	-0.000011	0.000000	-0.000004	0.000000	-0.000002	0.000000	0.000000	0.000000
Layer 4	0.000029	-0.000109	-0.000001	-0.000033	0.000000	-0.000016	-0.000002	0.000000	0.000000

Model chemical potential differences for endmembers across layers (m^3/mol): $h^{r*}(d\mu_j/dx)^{r*}$

	alm	prp	grs	sps	crd	fcrd	mncrd	en	fs	mgts	an	qtz
Layer 1	-0.000020	0.000006	-0.000003	0.000007	0.000007	-0.000010	0.000007	0.000011	-0.000006	-0.000005	-0.000004	0.000006
Layer 2	-0.000029	-0.000017	-0.000006	-0.000008	-0.000028	-0.000036	-0.000022	0.000007	-0.000001	-0.000024	-0.000013	0.000006
Layer 3	-0.000023	-0.000017	-0.000012	-0.000012	-0.000031	-0.000035	-0.000028	0.000003	-0.000001	-0.000021	-0.000016	0.000003
Layer 4	-0.000231	-0.000178	-0.000134	-0.000130	-0.000321	-0.000356	-0.000290	0.000026	-0.000009	-0.000204	-0.000161	0.000029

Model chemical potential differences for components from boundary 1 at boundary q (m^3/mol)

	Si	Al	Fe^{3+}	Fe^{2+}	Mn	Mg	Ca	Na	K
Boundary 2	0.000006	-0.000005	0.000000	-0.000009	0.000000	0.000000	-0.000005	-0.000008	-0.000003
Boundary 3	0.000012	-0.000019	0.000001	-0.000016	0.000000	-0.000003	-0.000004	-0.000007	-0.000005
Boundary 4	0.000016	-0.000030	0.000001	-0.000020	0.000000	-0.000005	-0.000004	-0.000007	-0.000005
Boundary 5	0.000045	-0.000139	0.000000	-0.000053	0.000000	-0.000021	-0.000006	-0.000007	-0.000005

Model chemical potential differences for endmembers from boundary 1 at boundary q (m^3/mol)

		alm	prp	grs	sps	crd	fcrd	mncrd	en	fs	mgts	an	qtz
Boundary 2	$\sum_{r=1}^{1} h^{r*}(d\mu_j/dx)^{r*}$	-0.000020	0.000006	-0.000003	0.000007	0.000007	-0.000010	0.000007	0.000011	-0.000006	-0.000005	-0.000004	0.000006
Boundary 3	$\sum_{r=1}^{2} h^{r*}(d\mu_j/dx)^{r*}$	-0.000049	-0.000011	-0.000009	-0.000001	-0.000021	-0.000046	-0.000014	0.000018	-0.000007	-0.000029	-0.000017	0.000012
Boundary 4	$\sum_{r=1}^{3} h^{r*}(d\mu_j/dx)^{r*}$	-0.000072	-0.000029	-0.000021	-0.000013	-0.000052	-0.000081	-0.000042	0.000021	-0.000008	-0.000050	-0.000033	0.000016
Boundary 5	$\sum_{r=1}^{4} h^{r*}(d\mu_j/dx)^{r*}$	-0.000302	-0.000207	-0.000155	-0.000144	-0.000374	-0.000438	-0.000332	0.000047	-0.000017	-0.000254	-0.000194	0.000045

Table 5.16: SK9C : Chemical potential relationships for components and end-members across corona layers

Model chemical potential gradients for components in layers 1 to 3 (mol mineral/mol reaction progress)

	hr^* ($10^{-4}m^3$/mol)	Si	Al	Fe^{3+}	Fe^{2+}	Mn	Mg	Ca	Na	K
Layer 1	0.862118	0.026335	-0.028410	-0.213080	-0.046999	-0.018339	0.022767	-0.018841	-0.031502	-0.002607
Layer 2	0.128363	0.032398	-0.058548	-0.221900	-0.051469	-0.021711	0.018150	-0.003624	-0.004799	-0.000397
Layer 3	0.280986	0.031726	-0.061785	-0.224820	-0.053474	-0.021869	0.017614	-0.000686	0.000000	0.000000

Model chemical potential differences for components across layers (m^3/mol): $h^{r*}(d\mu_i/dx)^{r*}$

	Si	Al	Fe^{3+}	Fe^{2+}	Mn	Mg	Ca	Na	K
Layer 1	0.000002	-0.000002	-0.000018	-0.000004	-0.000002	0.000002	-0.000002	-0.000003	0.000000
Layer 2	0.000000	-0.000001	-0.000003	-0.000001	0.000000	0.000000	0.000000	0.000000	0.000000
Layer 3	0.000001	-0.000002	-0.000006	-0.000002	-0.000001	0.000000	0.000000	0.000000	0.000000

Model chemical potential differences for endmembers across layers (m^3/mol): $h^{r*}(d\mu_j/dx)^{r*}$

	alm	prp	grs	sps	crd	fcrd	mncrd	en	fs	mgts	an	qtz
Layer 1	-0.000010	0.000008	-0.000001	-0.000003	0.000005	-0.000007	-0.000002	0.000008	-0.000004	-0.000001	-0.000002	0.000002
Layer 2	-0.000002	0.000000	0.000000	-0.000001	0.000000	-0.000002	-0.000001	0.000001	0.000000	-0.000001	-0.000001	0.000000
Layer 3	-0.000005	0.000001	-0.000001	-0.000003	-0.000001	-0.000005	-0.000004	0.000003	-0.000001	-0.000002	-0.000002	0.000001

Model chemical potential differences for components from boundary 1 at boundary q (mol mineral/mol reaction progress)

	Si	Al	Fe^{3+}	Fe^{2+}	Mn	Mg	Ca	Na	K
Boundary 2	0.000002	-0.000002	-0.000018	-0.000004	-0.000002	0.000002	-0.000002	-0.000003	0.000000
Boundary 3	0.000003	-0.000003	-0.000021	-0.000005	-0.000002	0.000002	-0.000002	-0.000003	0.000000
Boundary 4	0.000004	-0.000005	-0.000028	-0.000006	-0.000002	0.000003	-0.000002	-0.000003	0.000000

Model chemical potential differences for endmembers from boundary 1 at boundary q (m^3/mol)

		alm	prp	grs	sps	crd	fcrd	mncrd	en	fs	mgts	an	qtz
Boundary 2	$\sum_{r=1}^{1} h^{r*}(d\mu_j/dx)^{r*}$	-0.000010	0.000008	-0.000001	-0.000003	0.000005	-0.000007	-0.000002	0.000008	-0.000004	-0.000001	-0.000002	0.000002
Boundary 3	$\sum_{r=1}^{2} h^{r*}(d\mu_j/dx)^{r*}$	-0.000012	0.000008	-0.000002	-0.000004	0.000005	-0.000009	-0.000003	0.000010	-0.000004	-0.000002	-0.000003	0.000003
Boundary 4	$\sum_{r=1}^{3} h^{r*}(d\mu_j/dx)^{r*}$	-0.000018	0.000009	-0.000003	-0.000007	0.000004	-0.000014	-0.000007	0.000013	-0.000005	-0.000004	-0.000004	0.000004

Model reaction affinities and ratios between model end-member reaction affinities, i.e., Q-ratios, are reported in Table 5.17. End-member reactions differ slightly between the coronas, accommodating subtle differences in average mineral composition from each corona. Some Q-ratios are very sensitive to variation in composition of phases within and between coronas and the same end-member reaction ratios may vary widely. This is exemplified by Q-ratio 1a/4a for SK9A and SK9B, where 1a/4a = -3.680 in SK9A and -10.810 in SK9B (Table 5.17). Similarly, the same Q-ratio evaluated at site B in SK9B (1b/4b) yields -0.242. In contrast, other Q-ratios are less sensitive to compositional variation and, thus, are slightly more robust, e.g., 2a/3b and 1a/3b (see Table 5.17). Compositional sensitivity may limit the use of some Q-ratios in modelling insofar as they may be equally vulnerable to uncertainties in the data (Ashworth et al., 2001) and may prevent accurate correlation with real end-member reaction affinities (calculated from Holland and Powell, 1998; November 2003 upgrade) in *P-T* space.

Real end-member reaction affinities were determined from the internally consistent database of Holland and Powell (1998; November 2003 upgrade) at a range of pressures from 1 to 5 kbar and 500 - 1200 °C using James Connolly's Perplex application, Frendly (*www.perplex.ethz.ch)*. Ratios of real end-member reaction affinities are compared with model affinity ratios (Q-ratios). A line in *P-T* space may be defined along which equality between ratios of real and model reaction affinities is attained. These lines should intersect at a point within error, which defines the predominant *P* and *T* prevailing during corona formation. Figures 5.55 - 5.59 are *P-T* grids for Q-ratio lines of equality between model and real end-member reaction affinities for all coronas. In Figure 5.55, the *P-T* grid for SK8C, there appears to be a clustering of Q-ratio intersections at 750 °C and 2.75 kbar and a broad, smeared cluster at ~620 °C and 3.5 kbar. In SK12A (Figure 5.56), there are two poorly constrained Q-ratio clusters at ~ 780 °C and 2.5 kbar and ~ 700 °C and 3.1 kbar. SK9A and SK9B exhibit very loosely-constrained Q-ratio clusters at 620 °C and 1.6 kbar in SK9A and 550 - 580 °C and 1.0 – 1.5 kbar in SK9B (Figure 5.57; Figure 5.58). Similarly, two poorly constrained Q-ratio clusters occur at 640-660 °C and 780 °C at 2 kbar in SK9C (Figure 5.59).

The smeared nature of clusters toward lower temperatures and lower pressures (particularly in SK9 coronas) may be attributed to poorly constrained Q-ratios in *P-T* space owing to uncertainties in the SEM compositional data acquired for coronas. It has been demonstrated that some Q-ratios are extremely sensitive to compositional variation and uncertainties in the data (e.g., Table 5.17, Ashworth et al., 2001). Resulting erroneous Q-ratios mean that the intersection between model and real end-member reaction affinity ratios is either not realized or is shifted in *P-T* space relative to other Q-ratio lines of equality, giving rise to a spread of Q-ratio intersections. Ashworth et al. (2001) encountered similar difficulties when constraining non-equilibrium *P, T* estimates for coronas developed between orthopyroxene and plagioclase from the Yenisey Ridge, Siberia (Chapter 3). Non-equilibrium thermobarometric estimates could be refined significantly with detailed EMP analysis of corona phases and this is recommended for future work on the Vredefort coronas.

Table 5.17: Model independent end-member reaction affinities

SK8C			SK12A		
		$(-\Delta G)_k^*$ (m^3/mol)			$(-\Delta G)_k^*$ (m^3/mol)
Reaction (k):	***A***	***B***	**Reaction (k):**	***A***	***B***
1) 2prp + 3qtz = crd + 2en	0.000213	-0.000440	1) en + mgts = prp	0	0.00016
2) 2mgts + 3qtz = crd	0.000213	-0.000444	2) 2prp + 3qtz = crd + 2en	0.000219	-0.000404
3) 2alm + 3qtz = fcrd + 2fs	0.000213	0.000866	3) 2alm + 3qtz = fcrd + 2fs	0.000219	0.000709
4) 3an + fs = grs + fcrd	-0.000109	-0.000498	4) 2prp + grs + 3qtz = 3an + 3en	0.000297	-0.000623
5) 3an + en = grs + crd	-0.000109	0.000155	5) 3an + fs = grs + fcrd	-0.000078	-0.000337

Q-ratios:				**Q-ratios:**			
1b/2b	0.992	1a/4b	-0.427	1b/2b	-0.397	1a/4b	0
1b/3b	-0.509	1a/5b	1.372	1b/3b	0.226	1a/5b	0
1b/4b	0.884	2a/1b	-0.483	1b/4b	-0.257	2a/1b	1.367
1b/5b	-2.844	2a/2b	-0.479	1b/5b	-0.476	2a/2b	-0.543
2b/3b	-0.513	2a/3b	0.245	2b/3b	-0.57	2a/3b	0.309
2b/4b	0.891	2a/4b	-0.427	2b/4b	0.648	2a/4b	-0.351
2b/5b	-2.867	2a/5b	1.372	2b/5b	1.199	2a/5b	-0.651
3b/4b	-1.738	3a/1b	-0.483	3b/4b	-1.137	3a/1b	1.367
3b/5b	5.59	3a/2b	-0.479	3b/5b	-2.106	3a/2b	-0.543
4b/5b	-3.217	3a/3b	0.245	4b/5b	1.852	3a/3b	0.309
1a/2a	1	3a/4b	-0.427	1a/2a	0	3a/4b	-0.351
1a/3a	1	3a/5b	1.372	1a/3a	0	3a/5b	-0.651
1a/4a	-1.957	4a/1b	0.247	1a/4a	0	4a/1b	1.854
1a/5a	-1.957	4a/2b	0.245	1a/5a	0	4a/2b	-0.736
2a/3a	1	4a/3b	-0.125	2a/3a	1	4a/3b	0.419
2a/4a	-1.957	4a/4b	0.218	2a/4a	0.737	4a/4b	-0.477
2a/5a	-1.957	4a/5b	-0.701	2a/5a	-2.806	4a/5b	-0.883
3a/4a	-1.957	5a/1b	0.247	3a/4a	0.737	5a/1b	-0.487
3a/5a	-1.957	5a/2b	0.245	3a/5a	-2.806	5a/2b	0.193
4a/5a	1	5a/3b	-0.125	4a/5a	-3.806	5a/3b	-0.11
1a/1b	-0.483	5a/4b	0.218	1a/1b	0	5a/4b	0.125
1a/2b	-0.479	5a/5b	-0.701	1a/2b	0	5a/5b	0.232
1a/3b	0.245			1a/3b	0		

Table 5.17 continued: Model independent end-member reaction affinities

SK9A			SK9B		
	$(-\Delta G)_k^*$ (m^3/mol)			$(-\Delta G)_k^*$ (m^3/mol)	
Reaction (k):	***A***	***B***	**Reaction (k):**	***A***	***B***
1) 2prp + 3qtz = crd + 2en	0.000102	-0.000136	1) 2prp + 3qtz = crd + 2en	0.000134	0.000039
2) 2mgts + 3qtz = crd	0.000102	-0.000209	2) 2mgts + 3qtz = crd	0.000134	-0.000374
3) 2alm + 3qtz = fcrd + 2fs	0.000102	0.001020	3) 2alm + 3qtz = fcrd + 2fs	0.000134	0.000167
4) 3an + fs = grs + fcrd	-0.000028	-0.000100	4) 3an + fs = grs + fcrd	-0.000012	-0.000162
5) 2prp + 9an + 3fs = 3grs + 2alm + 3crd	-0.000083	-0.000300	5) 2prp + 9an + 3fs = 3grs + 2alm + 3crd	-0.000012	-0.000486

Q-ratios:				Q-ratios:			
1b/2b	0.652	1a/4b	-1.016	1b/2b	-0.105	1a/4b	-0.825
1b/3b	-0.134	1a/5b	-0.339	1b/3b	0.235	1a/5b	-0.275
1b/4b	1.364	2a/1b	-0.745	1b/4b	-0.242	2a/1b	3.403
1b/5b	0.455	2a/2b	-0.485	1b/5b	-0.081	2a/2b	-0.357
2b/3b	-0.205	2a/3b	0.100	2b/3b	-2.238	2a/3b	0.800
2b/4b	2.094	2a/4b	-1.016	2b/4b	2.308	2a/4b	-0.825
2b/5b	0.698	2a/5b	-0.339	2b/5b	0.769	2a/5b	-0.275
3b/4b	-10.206	3a/1b	-0.745	3b/4b	-1.031	3a/1b	3.403
3b/5b	-3.402	3a/2b	-0.485	3b/5b	-0.344	3a/2b	-0.357
4b/5b	0.333	3a/3b	0.100	4b/5b	0.333	3a/3b	0.800
1a/2a	1.000	3a/4b	-1.016	1a/2a	1.000	3a/4b	-0.825
1a/3a	1.000	3a/5b	-0.339	1a/3a	1.000	3a/5b	-0.275
1a/4a	-3.680	4a/1b	0.202	1a/4a	-10.810	4a/1b	-0.315
1a/5a	-1.227	4a/2b	0.132	1a/5a	-10.810	4a/2b	0.033
2a/3a	1.000	4a/3b	-0.027	2a/3a	1.000	4a/3b	-0.074
2a/4a	-3.680	4a/4b	0.276	2a/4a	-10.810	4a/4b	0.076
2a/5a	-1.227	4a/5b	0.092	2a/5a	-10.810	4a/5b	0.025
3a/4a	-3.680	5a/1b	0.607	3a/4a	-10.810	5a/1b	-0.315
3a/5a	-1.227	5a/2b	0.396	3a/5a	-10.810	5a/2b	0.033
4a/5a	0.333	5a/3b	-0.081	4a/5a	1.000	5a/3b	-0.074
1a/1b	-0.745	5a/4b	0.829	1a/1b	3.403	5a/4b	0.076
1a/2b	-0.485	5a/5b	0.276	1a/2b	-0.357	5a/5b	0.025
1a/3b	0.100			1a/3b	0.800		

Table 5.17 continued: Model independent end-member reaction affinities

SK9C

Reaction (k):	$(-\Delta G)_k^*$ (m^3/mol) *A*	*B*
1) 2prp + 3qtz = crd + 2en	0.0000107	-0.000014
2) 2mgts + 3qtz = crd	0.0000107	0.000004
3) 2alm + 3qtz = fcrd + 2fs	0.0000107	0.000021
4) 3an + fs = grs + fcrd	-0.0000059	-0.000012
5) 2sps + 6mgts + 9qtz = 2prp + 3mncrd	0.0000322	0.000011
6) 2prp + 4alm + 9qtz = 3crd + 6fs	0.0000322	0.000064

Q-ratios:

1b/2b	-4.071	2a/6a	0.333	3a/5b	1.016
1b/3b	-0.674	3a/4a	-1.805	3a/6b	0.168
1b/4b	1.227	3a/5a	0.333	4a/1b	0.415
1b/5b	-1.357	3a/6a	0.333	4a/2b	-1.688
1b/6b	-0.225	4a/5a	-0.185	4a/3b	-0.279
2b/3b	0.166	4a/6a	-0.185	4a/4b	0.509
2b/4b	-0.301	5a/6a	1.000	4a/5b	-0.563
2b/5b	0.333	1a/1b	-0.748	4a/6b	-0.093
2b/6b	0.055	1a/2b	3.047	5a/1b	-2.245
3b/4b	-1.821	1a/3b	0.504	5a/2b	9.141
3b/5b	2.014	1a/4b	-0.919	5a/3b	1.513
3b/6b	0.333	1a/5b	1.016	5a/4b	-2.756
4b/5b	-1.106	1a/6b	0.168	5a/5b	3.047
4b/6b	-0.183	2a/1b	-0.748	5a/6b	0.504
5b/6b	0.166	2a/2b	3.047	6a/1b	-2.245
1a/2a	1.000	2a/3b	0.504	6a/2b	9.141
1a/3a	1.000	2a/4b	-0.919	6a/3b	1.513
1a/4a	-1.805	2a/5b	1.016	6a/4b	-2.756
1a/5a	0.333	2a/6b	0.168	6a/5b	3.047
1a/6a	0.333	3a/1b	-0.748	6a/6b	0.504
2a/3a	1.000	3a/2b	3.047		
2a/4a	-1.805	3a/3b	0.504		
2a/5a	0.333	3a/4b	-0.919		

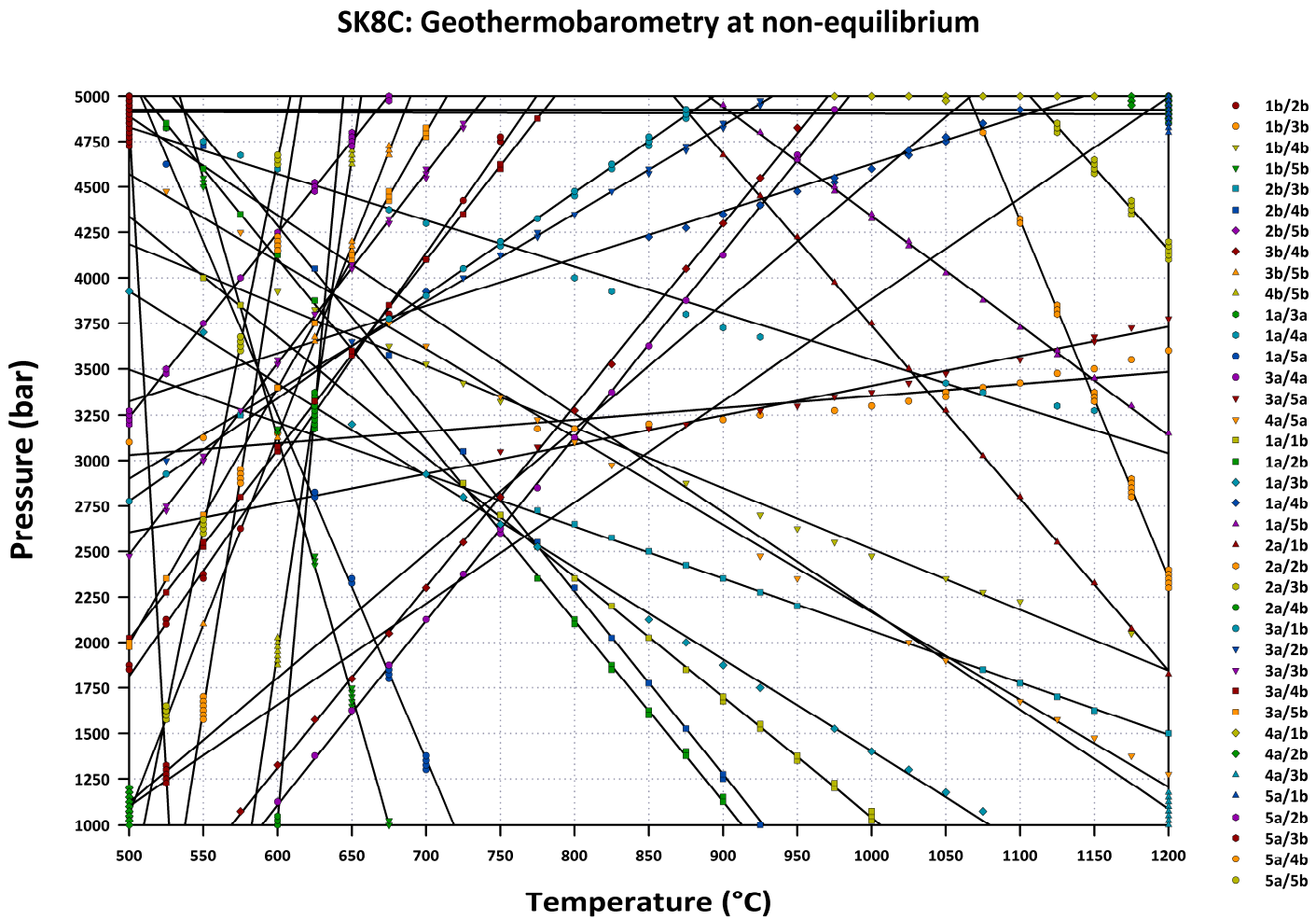

Figure 5.55: SK8C: Geothermobarometry from ratios between endmember reaction affinities using both case A and B (see text). Each line represents the P and T at which the ratio of affinities calculated from the dataset of Holland and Powell (1998, Nov 2003) equals the corresponding ratio of model reaction affinities.

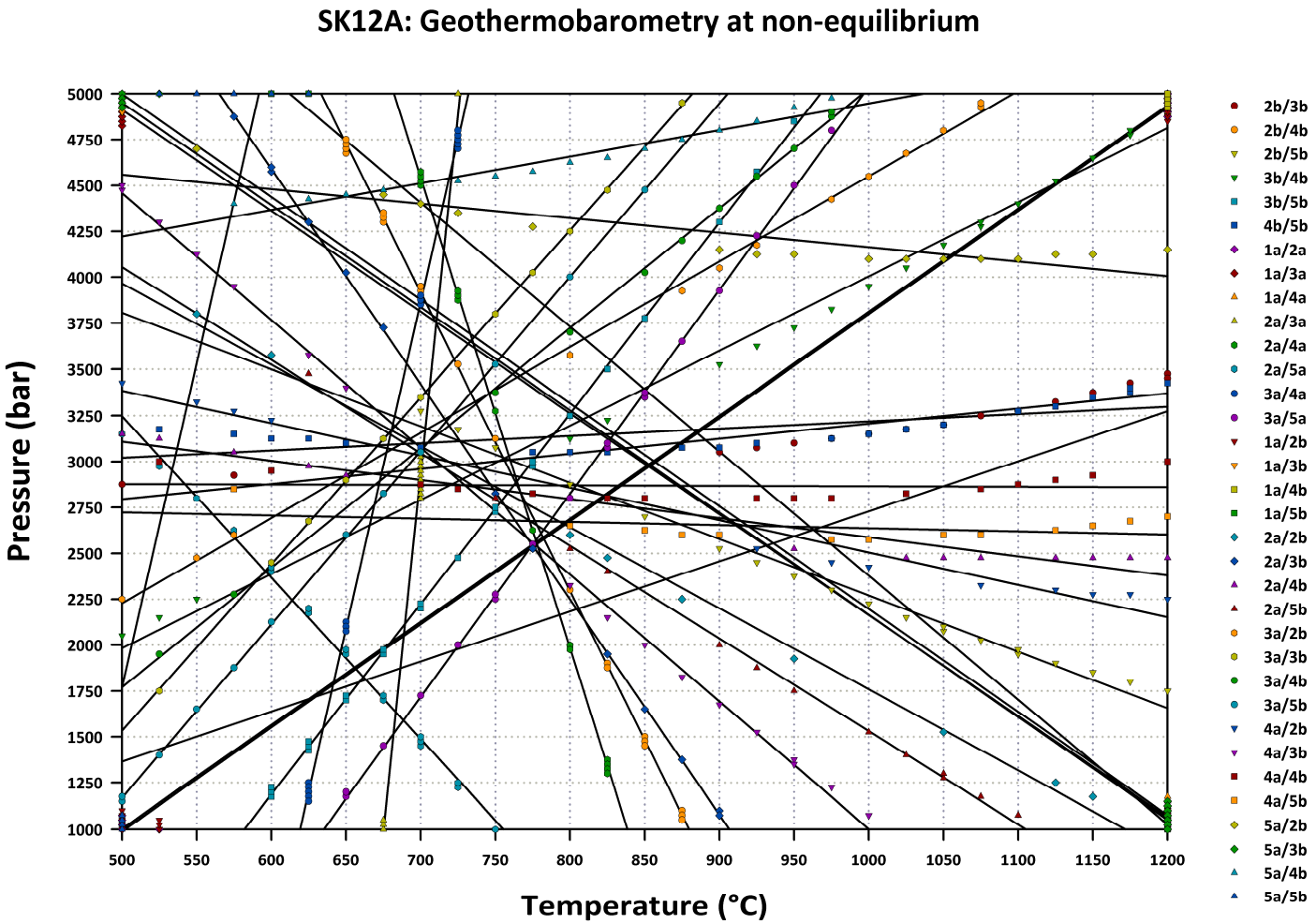

Figure 5.56: SK12A: Geothermobarometry from ratios between endmember reaction affinities using both case A and B (see text for details). Each line represents P and T at which the ratio of affinities calculated from the dataset of Holland and Powell (1998, Nov 2003) equals the corresponding ratio of model reaction affinities.

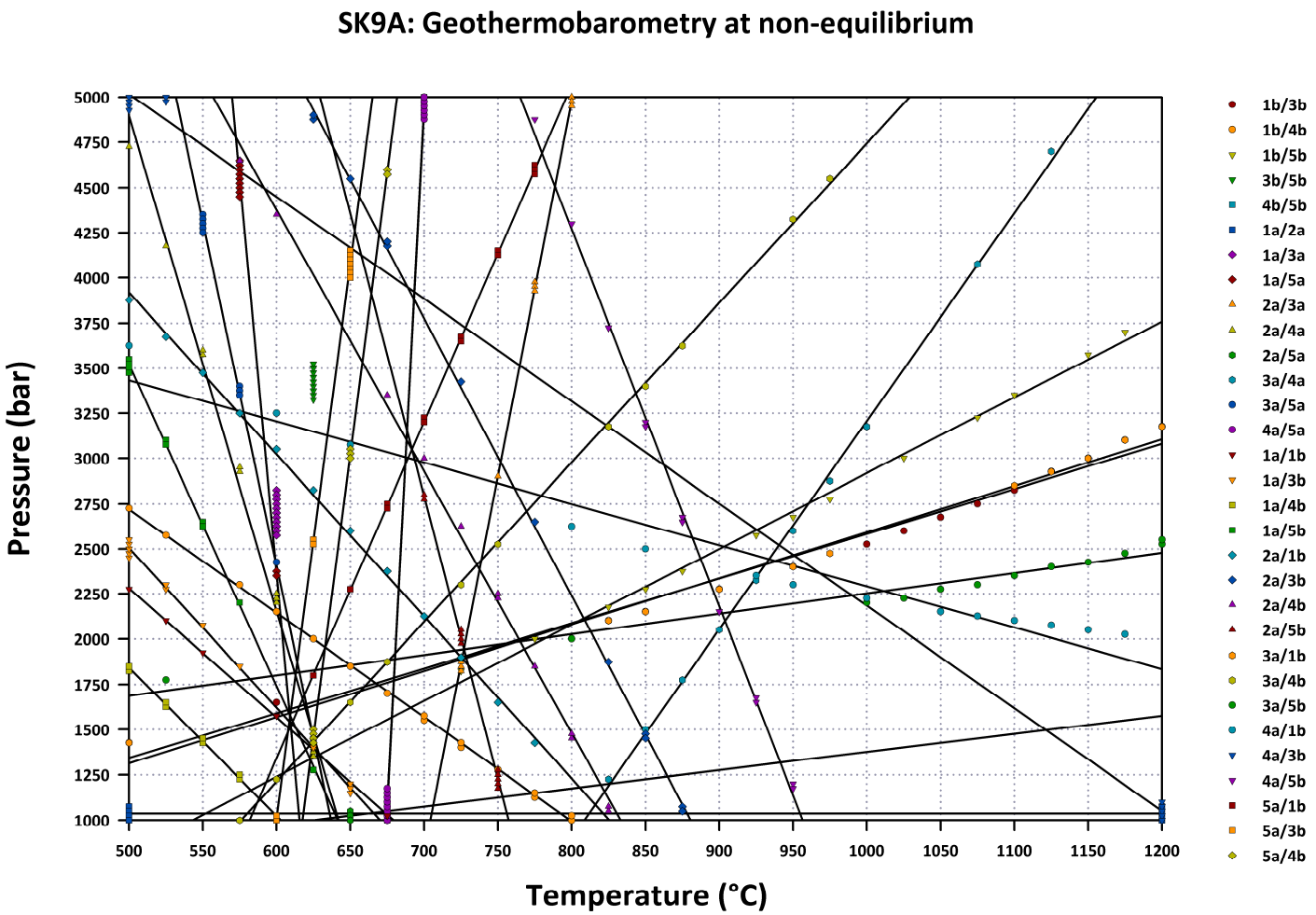

Figure 5.57: SK9A: Geothermobarometry from ratios between endmember reaction affinities using both case A and B (see text for details). Each line represents P and T at which the ratio of affinities calculated from the dataset of Holland and Powell (1998, Nov 2003) equals the corresponding ratio of model reaction affinities.

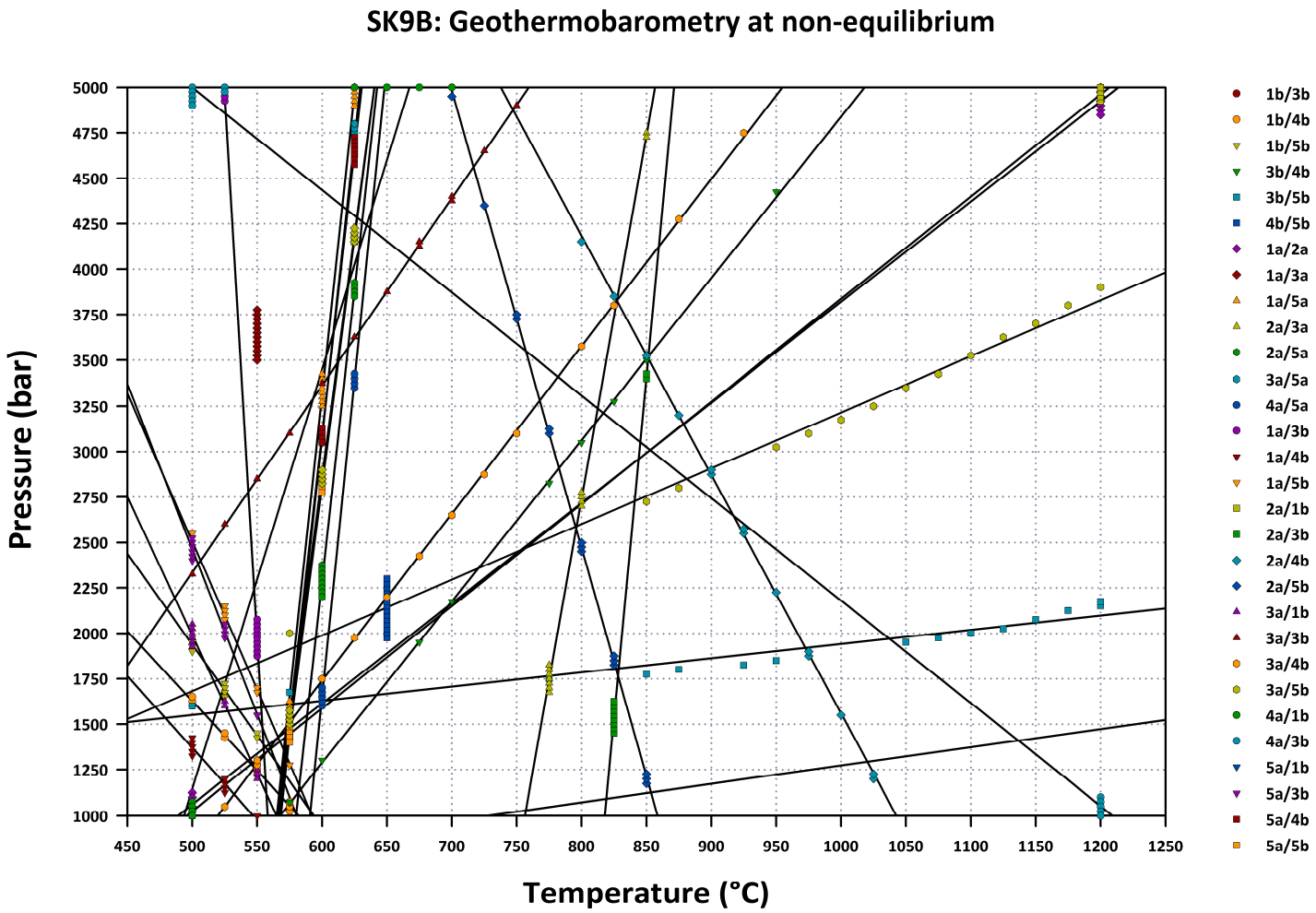

Figure 5.58: SK9B: Geothermobarometry from ratios between endmember reaction affinities using both case A and B (see text for details). Each line represents P and T at which the ratio of affinities calculated from the dataset of Holland and Powell (1998, Nov 2003) equals the corresponding ratio of model reaction affinities.

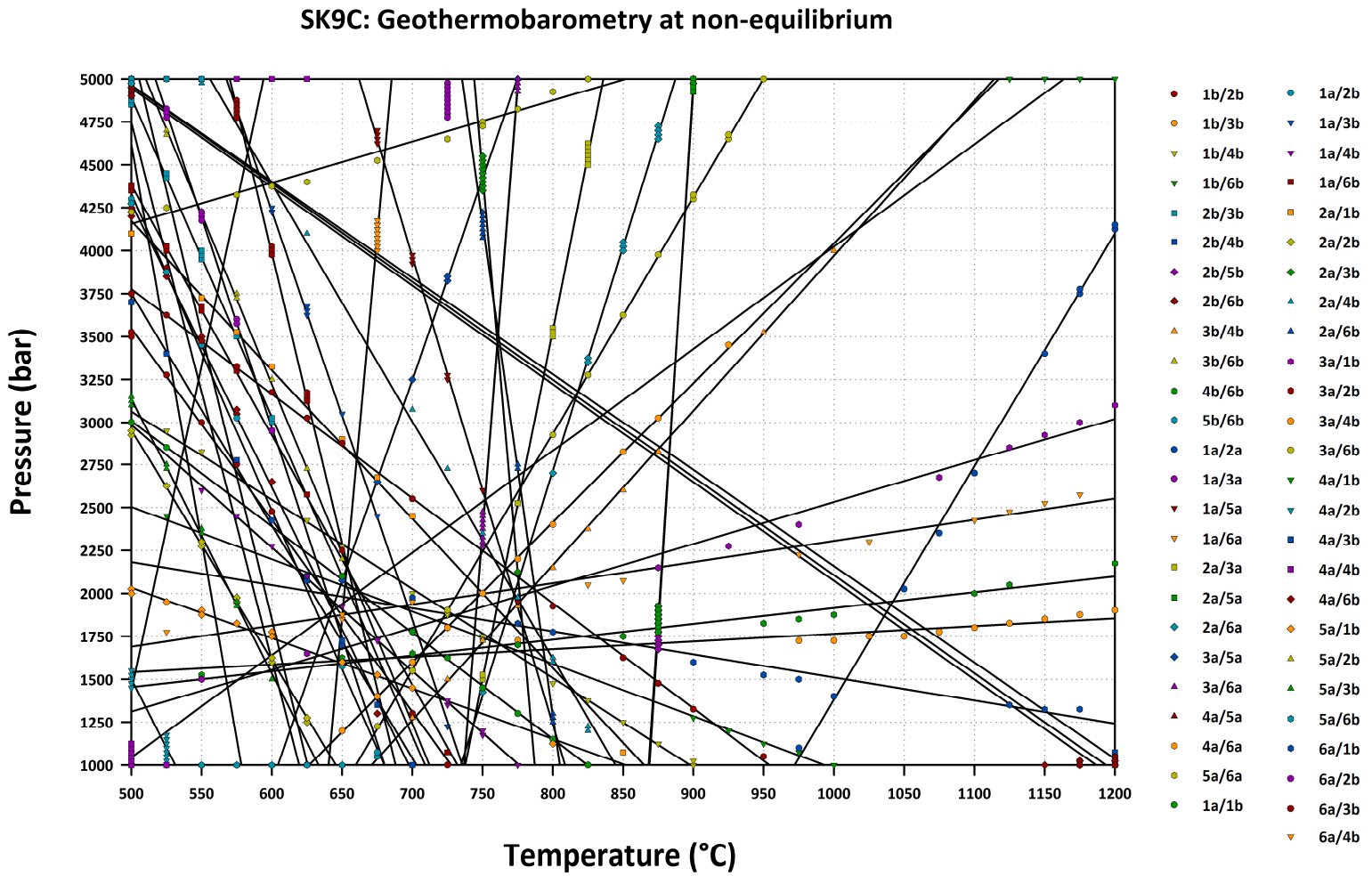

Figure 5.59: SK9C: Geothermobarometry from ratios between endmember reaction affinities using both case A and B (see text for details). Each line represents P and T at which the ratio of affinities calculated from the dataset of Holland and Powell (1998, Nov 2003) equals the corresponding ratio of model reaction affinities.

5.3.10 Reaction affinity

An expression for model reaction affinity derived by Ashworth and Sheplev (1997) is derived in Appendix A. The reaction affinity is a function of phase compositions, phase proportions (v_k), layer thicknesses and chemical potential gradients across all layers:

$$(-\Delta G) = \sum_{k=1}^{\phi} v_k \sum_{i=1}^{S} n_{ik} \sum_{r=1}^{q^k-1} h^{r*} \left(\frac{d\mu_i}{dx}\right)^{r*} \qquad eqn\ 5.11$$

Flatter chemical potential gradients reduce the $(-\Delta G)$ accordingly, such that $(-\Delta G)$ approaches zero, indicative of greater extent of equilibration. In contrast, large chemical potential gradients over thicker layers will cause the product $(-\Delta G)$ to deviate further from zero, suggesting suppressed equilibration.

The reaction affinity for each corona investigated is presented in Figure 5.60. The reaction affinity has been calculated in two other cases, for coronas from mafic granulites by Ashworth and Sheplev (1997) and Ashworth et al. (1998), and these are included in Figure 5.60 for comparison with the coronas under investigation. Ashworth and Sheplev (1997) modelled a reaction affinity for a corona bearing hornblende after plagioclase and olivine of 0.000132 m^3mol^{-1}, in an olivine gabbro (ASH1 in Figure 5.60). Ashworth et al. (1998) obtained a much higher reaction affinity for a less hydrous corona comprising garnet, pyroxene and quartz after plagioclase and pyroxene of 0.001344 m^3mol^{-1} (ASH2 in Figure 5.60).

In the Vredefort coronas, reaction affinity decreases from 0.00079 m^3mol^{-1} in SK8C and 0.00058 m^3mol^{-1} in SK12A to 0.00027 m^3mol^{-1} in SK9A. The reduction in reaction affinity accords with general trends of decreasing L-ratios (Figure 5.26), i.e., increasingly rapid diffusion relative to Si, and decreasing chemical potential gradients for components (Figure 5.46) and free energy gradients (Figure 5.52) for phases across layers in these coronas from SK8C to SK9A. Reaction affinity for SK9B (0.00031 m^3mol^{-1}) is marginally larger than SK9A despite similarity in magnitudes of L-ratios, chemical potential gradients and free energy gradients. This

may be attributed to the presence of an intervening K-feldspar layer, which increases the contribution of the term $\sum_{r=1}^{q^k-1} h^{r*} \left(\frac{d\mu_i}{dx}\right)^{r*}$ to the sum in equation 5.11 for determination of reaction affinity. SK9C is the most equilibrated corona, with reaction affinity approaching zero, an order-of-magnitude lower than either of the two coronas modelled by Ashworth and Sheplev (1997) and Ashworth et al. (1998). Suppressed reaction affinity for SK9C is consistent with the smallest L-ratios (Section 5.3.2, Figure 5.26, Table 5.5-5.9), lowest model chemical potential gradients for all components (Section 5.3.5, Figure 5.46, Table 5.5-5.9) and the lowest Gibbs free energy gradients for all phases across the corona (Section 5.3.7, Figure 5.52, Table 5.5-5.9).

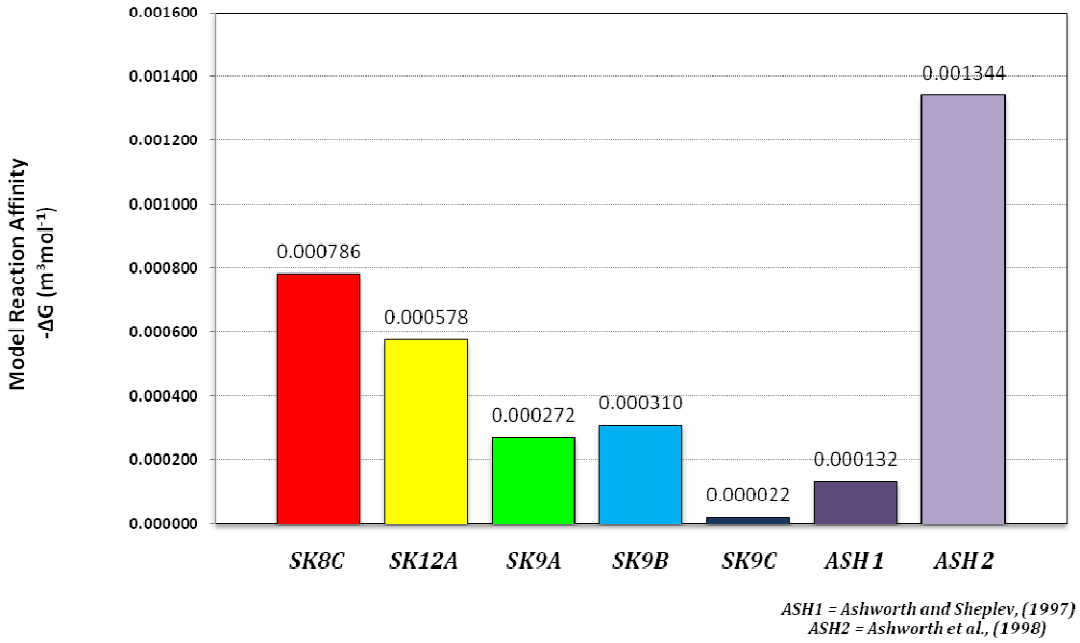

Figure 5.60: Model reaction affinity for coronas investigated. Reaction affinity progressively decreases toward the core of the Dome in coronas SK8C, SK12A and SK9A. Marginal corona, SK9C, with the most hydrous effective bulk composition, has the lowest reaction affinity. The only two other coronas modelled in the literature are from mafic granulites. ASH2 is an anhydrous corona comprising a garnet-pyroxene-quartz product assemblage after plagioclase and pyroxene. ASH1 is a hornblende-bearing corona after plagioclase and olivine.

5.4 Discussion

Open-system diffusion models have been constructed for coronas after garnet and quartz in the Steynskraal granulites in a variety of spatial, textural and compositional regimes to characterize the influence of post-shock temperature and bulk composition on the extent of corona development and equilibration. Coronas in samples SK8C, SK12A and SK9A are close analogues for a pure end-member garnet-quartz effective bulk composition since they are included in the garnet core and armoured from interaction with the enclosing matrix. Apart from a slight variation in X_{Mg} (SK8C = 0.41, SK12A = 0.39; SK9A = 0.44), bulk compositions immediately prior to onset of reaction are similar. The corona layer sequence developed in each of these coronas includes: cordierite + orthopyroxene symplectite → plagioclase → blocky orthopyroxene.

The influence of bulk composition on equilibration may be evaluated in coronas SK9A, SK9B and SK9C. Coronas SK9B and SK9C occur in the same sample as SK9A, but with different textural associations and, thus, different effective bulk compositions. SK9B is a more potassic, siliceous, EBC compared to SK9A, owing to communication with an adjacent K-feldspar inclusion in garnet. Enrichment in $KO_{1/2}$ in the SK9B EBC manifests as a K-feldspar layer between the plagioclase and blocky orthopyroxene layers. SK9C is a corona developed between a garnet margin and the matrix. It displays a markedly higher cordierite mode, thicker symplectite, trace biotite and a comparatively thinner blocky orthopyroxene layer, consistent with a slightly more hydrous EBC. Given the range of compositions for the same post-shock temperature, the compositional control on equilibration was assessed through open-system diffusion models.

Inputs in the open-system diffusion models include estimates of corona product proportions obtained from rigorous image analysis of corona products (Section 5.3.3) and average phase compositions in each layer (Section 5.2). The modes of cordierite and plagioclase decrease in the order SK8C→SK12A→SK9A, whilst the mode of orthopyroxene (symplectite and blocky combined) increases. Cordierite mode is highest, and overall orthopyroxene mode is lowest, in SK9C. Plagioclase mode is highest in SK9B compared to all other coronas, as is the mode of blocky

orthopyroxene. Lowest cordierite modes are observed in SK9B. The compositions of product phases vary across corona layers in all coronas. X_{Mg} and y(Opx) of symplectite orthopyroxene (Opx_{S1}) and cordierite X_{Mg} progressively decrease from garnet toward layer 2 plagioclase. X_{Ab} decreases in plagioclase layers toward quartz in SK9A, whereas no systematic trend in zonation is observed in other coronas. X_{Ab} decreases towards quartz in the K-feldspar layer of SK9B. X_{Mg} and y(Opx) for blocky orthopyroxene also decrease towards the contact with quartz. In SK9A and SK9C, the X_{Mg} for blocky orthopyroxene increases slightly above the minimum values for symplectite orthopyroxene, before decreasing systematically across the layer towards quartz. Compositional variation (Section 5.2.1) is minimized in SK9C. In contrast, there is greater compositional variation in SK8C and SK12A. Inasmuch as compositional variation indicates prevailing chemical potential gradients, the mole fraction standard deviation for phase analyses in a corona might be used as a proxy for equilibration. Accordingly, equilibration is most enhanced in SK9C and most suppressed in SK8C.

Since the Al/Si ratio of reactant garnet is not conserved in the symplectite (Section 5.2.2), closure of the system could not be used as a constraint in defining the overall reaction (Section 5.3.1). A constant-volume approximation is used in derivation of the overall reaction instead (Carmichael, 1987; Carlson and Johnson, 1991). The system is considered open to all components including Al and Si. Metasomatic exchange with the surrounding matrix assemblage and prolonged reaction has altered or reset the composition of the reactant garnet, such that its final steady-state composition is more Fe-rich than the initial garnet composition at reaction onset. This is reflected in progressive Fe-enrichment of garnet compositions from the northwest of the Steynskraal traverse to the southeast, regardless of bulk rock composition (Chapter 2, Section 2.5, Figure 2.17). An apparent initial bulk composition was obtained from the final steady-state garnet composition that was corrected for metasomatic exchange with the external system by adjusting the bulk composition until the original composition of peak garnet predicted from THERMOCALC (Chapter 6) was reproduced. The true initial bulk composition is related to the final steady-state composition of the corona layers by metasomatic flux vectors. With prolonged corona reaction, the EBC becomes richer in FeO, MgO

and $NaO_{1/2}$ with a slight loss of $AlO_{3/2}$ to the external system, whilst remaining Si-saturated. SK8C and SK12A evolved to more magnesian final steady-state bulk compositions, whereas SK9A, SK9B and SK9C became more Fe-rich.

Stable open-system diffusion models were produced for all coronas. Ratios of phenomenological coefficients (L_{SiSi}/L_{ii}) modelled decrease progressively in the order SK8C→SK12A→SK9A→SK9B→SK9C (Section 5.3.2). Within all coronas the diffusion coefficients increase in the order: $L_{Al}<L_{Si}<L_{Na,Ca,K}<L_{Mg}<L_{Fe}$. Component fluxes across corona bands reflect a balance between corona product proportions and compositions, reactant phase compositions and reaction coefficients for phases at layer boundaries (Section 5.3.4). Highest-magnitude modelled component fluxes are those where mass transfer though a layer to a reaction site down the chemical potential gradient is largest, consistent with a marked compositional gradient. Positive fluxes are indicative of transport from garnet and negative fluxes suggest derivation at the quartz boundary. Flux magnitudes were largest for FeO (positive), followed by MgO (negative except in SK9B), $AlO_{3/2}$ (positive), SiO_2 (negative) and, finally, CaO, $NaO_{1/2}$ and $KO_{1/2}$. Fluxes vary considerably for the last three components between coronas, depending on the mode and composition of plagioclase.

Chemical potential gradients are a function of the component flux through a layer and the phenomenological coefficients for diffusing components (Section 5.3.5). Chemical potential gradients for all components decrease progressively in the order SK8C → SK12A → SK9B → SK9A → SK9C. The order of decreasing chemical potential gradients for components is: $AlO_{3/2}$ → FeO → SiO_2 → MgO → CaO, $NaO_{1/2}$, $KO_{1/2}$. Chemical potential gradients are high for FeO as a result of large FeO flux magnitudes across all corona layers, despite consistently having the smallest L-ratio. Gibbs free energy gradients for phases in product layers are, in general, largest for coronas with the highest magnitude chemical potential gradients (Section 5.3.7). Accordingly, the order of decreasing Gibbs free energy gradients for phases is: SK8C → SK12A → SK9A, SK9B → SK9C.

A non-equilibrium thermobarometric technique (Ashworth et al., 2001) has been applied to the coronas, in which ratios of model end-member reaction affinities (Q-

ratios) across a corona are correlated with real ratios of end-member reaction affinities calculated from an internally consistent thermodynamic database (Holland and Powell, 1998, Nov 2003 upgrade) in *P-T* space (Section 5.3.9). Unfortunately, the marked sensitivity of Q-ratios to uncertainties in compositional data acquired from SEM analysis means that the intersection between model and real end-member reaction affinity ratios in *P-T* space is either not realised or is shifted in *P-T* space relative to other Q-ratio lines of equality, giving rise to a spread of Q-ratio intersections and poorly constrained *P-T* estimates. More rigorous EMP analysis of corona products is required for refinement of the non-equilibrium thermobarometry.

Overall reaction affinity has been calculated for all coronas (Section 5.3.10). Model reaction affinity diminishes in the order SK8C (0.00079 m^3mol^{-1}) → SK12A (0.00058 m^3mol^{-1}) → SK9B (0.00031 m^3mol^{-1}) → SK9A (0.00027 m^3mol^{-1}) → SK9C (0.000022 m^3mol^{-1}). Equilibration is enhanced in SK12A and SK9A compared to SK8C owing to higher post-shock temperatures and increased intergranular diffusion of major components, facilitating equalization of chemical potentials across the corona. Expansive length-scales of H_2O diffusion from hydrous matrix phases into the core of garnet at higher post-shock temperatures in SK9A compared to SK8C may also contribute to enhanced intergranular diffusion of all components by lowering the solidus for the corona reaction and increasing melt volumes in the corona domain. This possibility is investigated in Chapter 6. The FeO-enrichment of the SK9A final steady-state corona bulk composition relative to SK8C and SK12A is attributed to elevated metasomatic input of FeO into the equilibration volume, with higher intergranular diffusivities at higher post-shock temperatures so as to stabilize the more Fe-rich, more equilibrated, post-impact reaction products.

Near-coincident chemical potential gradients for Si and Al, and comparable free energy gradients for phases in layers, contribute to very similar overall reaction affinities for SK9A and SK9B, despite compositional differences. Lower reaction affinity in the marginal corona, SK9C may be ascribed to a more hydrous corona bulk composition derived from open-system chemical communication with a biotite-rich matrix. As $a H_2O$ is raised in the corona bulk composition, the solidus might be

lowered in the corona domain accordingly (Chapter 6). Assuming corona reaction cessation at the solidus, a lower-temperature solidus implies more prolonged reaction, with higher melt modes in SK9C compared to SK9A and SK9B, facilitating equilibration and lowering reaction affinity in the more hydrous bulk composition. Ashworth et al. (1998) also obtained a lower reaction affinity for a more hydrous hornblende-bearing corona developed after plagioclase and olivine (Figure 5.60, ASH1) compared to an anhydrous corona comprising garnet, pyroxene and quartz after plagioclase and pyroxene (Figure 5.60, ASH2; Ashworth et al., 1998). In addition to the closer spatial proximity to hydrous phases in the matrix, marginal coronas may have been more exposed to highly mobile and reactive biotite shock melts known from experiments to have been generated at the shock pressures experienced by these rocks (Chapter 7). The presence of these shock melts would also have greatly enhanced diffusion in marginal rim coronas relative to core coronas.

In summary, open-system diffusion modelling has established a strong temperature and compositional control on extent of equilibration in the garnet-quartz corona domain. In Chapter 6, variation in modal mineralogy between all corona domains from the core and rim of garnet is modelled in THERMOCALC with T-X pseudosections to clarify the dependence of corona development on both temperature and the proportion of H_2O-rich melt.